UNIVERSIDAD NACIONAL AUTÓNOMA DE MÉXICO
POSGRADO EN CIENCIAS FÍSICAS
INSTITUTO DE FÍSICA
FÍSICA CUÁNTICA, ATÓMICA Y MOLECULAR

Exploring a Third Spin Species in Ultracold Fermi Gases: Beyond Conventional Two-Component System

TESIS
QUE PARA OPTAR POR EL GRADO DE:
MAESTRO EN CIENCIAS (FÍSICA)

PRESENTA:
JUAN PABLO LEMUS SALDIVAR

TUTOR PRINCIPAL:
DR. FREDDY JACKSON POVEDA CUEVAS
INVESTIGADOR POR MÉXICO - INSTITUTO DE FÍSICA, UNAM

MIEMBROS DE COMITÉ TUTOR:

DR. ROBERTO DE JESUS LEÓN MONTIEL
INSTITUTO DE CIENCIAS NUCLEARES, UNAM

DR. DANIEL SAHAGÚN SÁNCHEZ
INSTITUTO DE FÍSICA, UNAM

CIUDAD UNIVERSITARIA, CIUDAD DE MÉXICO, JULIO 2025

A la comunidad disidente que resiste y revoluciona la ciencia en Latinoamérica,
pues el camino no ha sido fácil para nosotres

Agradecimientos

A mí mamá, Lidya Saldivar, por apoyarme siempre y enseñarme mucho de la vida, por procurarme siempre y velar por mi bienestar. Gracias mami por ser un ejemplo para mi. Para mi tú eres mi ejemplo a seguir. Este trabajo no existiría sin ti.

A mi papá, Juan Manuel Lemus, en quien he visto que el tiempo no es más que otro aliado. Siempre buscaste ser correcto conmigo, pero te agradezco que ahora que administras tus emociones de otra manera, me has demostrado ese cariño que tanto me ha hecho bien. También por cuidad de mi Kisi.

A mi hermano, R. David, a quien amo y adoro con todo mi corazón. A la persona que mas he extrañado los últimos dos años de mi vida y quien a decidido embarcarse en este mismo mar. Quiero que sepas que estoy muy orgullose de ti. Espero algún día estar leyendo tu tesis o tu primer artículo para dicutirlo juntes.

A mi asesor, Jackson, a quien estoy escuchando dictar clase en estos momentos y sigo recordando cómo es que me convenció para seguir en este negocio piramidal. Jackson, todo mi aprecio y cariño por la gran persona que eres y el gran Físico. Me inspiras muchísimo. Te lo he dicho cientos de veces pero quiero recordarlo una más, gracias a ti encontré en la Física una pasión y un gusto que llevaré, de ser posible, toda mi vida. Dr. Parce, me siento con mucha fortuna de haber hecho equipo contigo estos años. ¡Cámara parce!

A mis amistades de la fraternidad $|\kappa\alpha\mu\rangle$. A Jesica Espino, mi mejor amiga en estos últimos dos años, con quien sobreviví y reaprendí a vivir. Te quiero mucho Jesi Tribit. A Lalo Solis, un hermano académico con quien no solo discutí física, también discutí sobre la vida. Gracias por ser como eres, te quiero un buen Lalito. A César, hermano, recuerda siempre velar por ti y simepre seguir con el talento que tienes. Te abrazo mucho.

A David A. Díaz de Sandy, une persone con tantos proyectos tan preciosos y une excelente ser que me ha brindado su amor ya casi en la recta final de este camino pero ha abrazado mi corazón con tanto cariño. Eres inigualable, te adoro.

Al Laboratorio de Materia Ultrafría, mi segundo hogar en los últimos 4 años de mi vida. Literalmente, un sótano al que le tengo mucho cariño. A Jose Luis Lugo, un amigo y compañero con quien la pasábamos cotorreando para que la oscuridad del sótano no nos venciera (fracasamos en eso, pero no faltaron las risas); y si, ¡Sáquese la mano de'ay! A Natalia Rivera, quien se unió al equipo no hace mucho pero ha mostrado tener el caracter, la disciplina y el conocimiento que me inspiran; cree en ti, confía en ti. A ambos, porque me permitieron enseñarles lo que yo con mucho amor aprendí de hacer física experimental en Latinoamética y desde luego, con quienes nos divertimos en aquellas extenuantes horas metidos en el sótano donde alguna vez llovieron aguas turbias.

A Fernando Ballesteros, a quien decidí dedicarle un párrafo por mi extenso cariño y aprecio.

Mi compañero con quien manejé la maquina durante dos años consecutivos, mi amigo con quien aprendí de física, de rolitas que daban sed, de la vida y de todo un poco. Gracias Fer. A Paulina Carreón, la profesora más dedicada y con mejor estilo de la moda que he conocido. A ambos, por ser quienes siempre me recibieron con cordialidad y cariño en su hogar y en su familia.

A Jorge Seman, un experto en fermiones que se ha aventurado a construir un experiemnto tan inimaginable. Jorge, eres culpable de que me enamorara de la física atómica y por quien conocí a Jackson. No sé como saldar esa cuenta.

A mi comité tutor, Daniel Sahagún y Roberto León, de quienes tuve la fortuna de ser también estudiante y que reunión con reunión alimentaban este trabajo que hoy plasmo aquí.

Al GOA, ese grupo que Jackson creó ya hace unos años. Desde los primeros integrantes, los Jackson fives y a quienes lo conforman hoy en día, en cada integrate hallé mucha retroalimentación y crecimiento.

Al cuerpo de electrónicos que contribuyeron en el diseño de la antena, Carlos Gardea y Rodrigo Gutiérrez. A ambos, gracias por ayudarme a entender esto de los circuitos RF.

A mis sinodales, quienes me han ayudado a mejorar y estructurar este contenido. Dr. Arturo Camacho, Dr. Jorge Hirsch, Dr. Eduardo Gómez y Dr. José Jiménez-Mier, a cada uno de ustedes les agradezco sus comentarios y contribuciones para que este texto tuviese la calidad y contenido adecuado.

A la Doctora Rocío Jáuregui, por ser un pilar incomparable para estos proyectos y quien me ha brindado la oportunidad de continuar este proceso con el ingreso económico en los momento más oportunos. Admiro mucho su liderazgo y compromiso con la ciencia en México, Latinoamérica y el mundo.

A mis amistades que por más de 10 años ahí han estado, a ti Karen León y a ti Maya Martínez. A ambas las amo y les adoro muchísimo. Pareciera que fue ayer cuando reinventé Marianela. Las extraño también muchísimo. Espero que en este párrafo me encuentren siempre.

A mi Jimmy, José Juan Vega. Tú no sabes, pero sigues siendo mi mejor amigo (esta afirmación es atemporal, de lo contrario es porque no leíste esto); gracias por hablarme cuando estaba llorando en la prepa. A mi BERFMANA, Alma Eugenio, no sabes lo mucho que te adoro; podremos pasar periodos criogenizadas pero siempre que nos volvemos a encontrar es con el mismo amor y cariño; gracias a ese día que no llevabas resistol.

A mis girls, Karen Salgado y Mariana Mastache, a ustedes porque son unas personas increíbles y me han brindado un espacio seguro durante estos tiempos escalonados. Nos tocó crecer a la par en muchos aspectos y me siento afortunade de contar con su amistad. Saquen otra tarde de café y juegos. Karen, gracias por acompañarme desde el inicio de mi carrera, te quiero montonsotes por ese ser tan puro que eres. Maggie sólo quiero añadir que estoy muy impresionade con la forma en la que escribes y construyes, estoy muy orgullose de ti.

A Wendy, porque no tienes idea lo mucho que me ayudaste para comenzar mi camino para estar bien conmigo misme. Por todo lo que aprendimos y vivimos en algún momento.

A la comunidad no binarie y queer que pude ir conociendo mientras yo me iba conociendo, Yu Zavala, Nube, Martín Meza, Kia, Alex Castilo. Cada une de ustedes aportó en mi algo que no podría devolverlo.

A mis roomies de estos dos años, en particular a David Rojas con quien compatí más tiempo y anécdotas, sé que serás un buen hombre y un buen médico.

A todos y todas mis antepasados porque soy niete de quienes sembraron el maíz en extensos campos y hoy ese maíz que cultivaron se ha convertido en poder controlar las temperaturas más bajas del universo conocido.

Finalmente, a mi misme. Por ser valiente, por aprender a amarme, por cuidarme; pero también por cagarla, por caerme, por tener miedo, por creer que no podía. Porque sin alguna de esas versiones mías yo no estaría escribiento esto, esto que amo.

No se me olvidó, pero desentonaría mucho. A CONAHCYT, ahora la Secretaria de Ciencia, Humanidades, Tecnología e Innovación (SECIHTI), por otorgarme la fuente económica de la que me sustenté los últimos dos años: la beca de posgrado del programa de Becas Nacionales. De la misma forma, a la beca PAPIIT del proyecto IN104523 a la cual tuve acceso en la recta final de este trabajo.

Contents

List of Tables

List of Figures

Exploring a Third Spin Species in Ultracold Fermi Gases: Beyond Conventional Two-Component Systems

by

Juan Pablo Lemus Saldivar

Abstract

At the Ultracold Matter Laboratory (LMU), the properties of degenerate Fermi gases of ^{6}Li are studied at temperatures below the micro-Kelvin range. This fermionic isotope features a broad Feshbach resonance around 30 mT, which allows for the modulation of interactions between its two lowest-energy hyperfine states through the scattering length a_s. This fact enables the exploration of regimes from a Bose-Einstein Condensate (BEC), where molecular pairs are formed, to a BCS regime, characterized by extended Cooper-like pairs, as well as the crossover region between these two, known as the BEC-BCS crossover.

In this thesis we investigate the accessibility of a third hyperfine state, $|F = 3/2, m_F = -3/2\rangle \equiv |3\rangle$, resulting from Zeeman splitting in the resonance region of the states $|F = 1/2, m_F = -1/2\rangle \equiv |1\rangle$ and $|F = 1/2, m_F = +1/2\rangle \equiv |2\rangle$. The region is centered around 70 mT, where the energy separation between the states $|1\rangle - |2\rangle$ and $|2\rangle - |3\rangle$ is on the order of 80 MHz.

The third state from the two existing ones is populated through radiofrequency (RF) antenna emission. The design and construction of this RF antenna, adapted to the experimental conditions of the LMU, to realize the $|2\rangle \leftrightarrow |3\rangle$ transition, is presented in this work. Additionally, we present details about the design, construction, and implementation of two antennas.

Finally, we present the measurements of Rabi oscillations between the hyperfine states conducted in different interaction regimes. The formation of new pairs, $|1\rangle - |3\rangle$ and $|2\rangle - |3\rangle$, is also studied, taking advantage of the proximity of the Feshbach resonances of any pairs possible. To conclude, we analyzed the behavior of a fermionic sample of three species, which is such a promising platform for advanced physics research.

Exploring a Third Spin Species in Ultracold Fermi Gases: Beyond Conventional Two-Component Systems

por

Juan Pablo Lemus Saldivar

Resumen

En el Laboratorio de Materia Ultrafría (LMU), se estudian las propiedades de los gases de Fermi degenerados de ^{6}Li a temperaturas inferiores al rango micro-Kelvin. Este isótopo fermiónico presenta una amplia resonancia de Feshbach de alrededor de 30 mT, lo que permite modular las interacciones entre sus dos estados hiperfinos de menor energía mediante la longitud de dispersión a_s. Esto permite la exploración de regímenes que van desde un Condensado de Bose-Einstein (BEC), donde se forman pares moleculares, hasta un régimen BCS, caracterizado por pares extendidos de tipo Cooper, así como la región de cruce entre estos dos, conocida como cruce BEC-BCS.

En esta tesis investigamos la accesibilidad de un tercer estado hiperfino, $|F = 3/2, m_F = -3/2\rangle \equiv |3\rangle$, resultante del desdoblamiento Zeeman en la región de resonancia de los estados hiperfinos $|F = 1/2, m_F = +1/2\rangle \equiv |1\rangle$ y $|F = 1/2, m_F = -1/2\rangle \equiv |2\rangle$. La región se centra alrededor de 70 mT, donde la separación energética entre los estados $|1\rangle - |2\rangle$ y $|2\rangle - |3\rangle$ es del orden de 80 MHz.

El tercer estado, a partir de los dos existentes, se pobla mediante la emisión de una antena de radiofrecuencia (RF). En este trabajo se presenta el diseño y la construcción de esta antena de RF, adaptada a las condiciones experimentales del LMU, para lograr la transición $|2\rangle \leftrightarrow |3\rangle$. Además, presentamos detalles sobre el diseño, la construcción y la implementación de dos antenas.

Finalmente, presentamos las mediciones de las oscilaciones de Rabi entre los estados hiperfinos realizadas en diferentes regímenes de interacción. También estudiamos la formación de nuevos pares, $|1\rangle - |3\rangle$ y $|2\rangle - |3\rangle$, aprovechando la proximidad de las resonancias de Feshbach de cualquier par posible. Para concluir, analizamos el comportamiento de una muestra fermiónica de tres especies, una plataforma prometedora para la investigación en física avanzada.

Introduction

Within the framework of the second quantum revolution, the development of quantum technologies emerges from the ability to manipulate systems governed by the principles of quantum mechanics. Among these platforms, we have quantum macroscopic wave matter systems that obey quantum mechanical properties known as ultracold atomic gases. Atomic gases such as superconductors [4], topological materials [5], semiconductors [6], quantum dots, and NV-diamonds [7] appear on the list as strong promising systems for quantum technology platforms. Each one has advantages and disadvantages that align with the application perspectives.

In ultracold quantum systems, controlling internal degrees of freedom is the most important property. In this form, the cooled gases represent an exceptional promising system for pulling up to useful quantum devices. In particular, the control of the geometry and collectivity interactions, while the controlled study of such systems has unraveled fundamental phenomena like Bose-Einstein condensation [8–10], superfluidity [11], and thermodynamical phase transitions depending on the dimensionality of the trapped gases [12]. In this form, superfluidity remains an enigmatic property that can be used in quantum materials and technologies. In this thesis, we point out one of the possibilities of integrating another degree of freedom.

Quantum gases fall into two fundamental categories: bosonic and ferminic, according to whether the constituent atoms obey Bose-Einstein or Fermi-Dirac statistics. Their specific internal degrees of freedom, such as spin, determine which of these statistics applies to a given atomic species. In fermionic many-body and macroscopic systems, the Pauli exclusion principle plays the central role, determining the characteristic behavior of these systems. In this work, we focus on the ultracold Fermi gases because we cooled an isotope of Lithium, ^{6}Li. We emphasize the experimental accessibility of this fermionic system and open up a new perspective on controlling and manipulating the quantum properties.

The community of ultracold gases has been working to optimize the routines for generating samples below 500 nK. There is a great diversity of experiments on Bose gases, but the Fermi gases are more complicated in producing a quantum degenerate state [13, 14]. Until today, different atomic fermionic species have been brought to quantum degeneracy: ^{40}K [15], ^{6}Li [16], ^{173}Yb [17], ^{161}Dy [18] and ^{167}Er [19].

The Laboratorio de Materia Ultrafría (LMU) is an experimental setup designed to work

in topological defects and density structures in Fermi gases. The first stage at this laboratory is the generation and precision control of a degenerated fermionic isotope sample of Lithium (^{6}Li). This laboratory was born in response to the global context of quantum physics research and is dedicated to studying and developing technologies that contribute to the growing scientific knowledge. This national project is known as LANMAC (Laboratorio Nacional de Materia Cuántica).

The LMU degenerated Fermi gas was produced in 2018, and a few months later, the first molecular BEC in Mexico and the Latin American region [20], just 15 years after the pioneering work by D. Jin and her team [13]. D. Jin also realized the first Fermi degenerate gas [15] and produced for the first time, ultracold molecules from a Fermi gas [14]. In this context, the LMU has demonstrated the ability to realize with an ultracold cloud of ^{6}Li ground-state, with the possibility to tune the interactions allowing to access both the molecular Bose-Einstein condensate (BEC) or the Bardeen-Cooper-Schrieffer (BCS) state or a unitary-crossover state.

The degenerate Fermi gas of the LMU consists of two hyperfine states of the ground state of ^{6}Li. Given the conditions under which the ultracold sample is manipulated, a topic developed in detail throughout this work, it is possible to access a third hyperfine state. The third state is populated by applying a radio-frequency (RF) signal that excites one of the initial states. Around the world, laboratories working with these fermionic states have access to the third using the technique mentioned above [21–24]. Obtaining a system of three species allows us to verify known results. It opens the door to many other phenomena unexplored or less explored in physics, such as Efimov states, Fermi impurities, balanced samples with strong interactions, and similar three-body problems.

This work focuses on generating the third spin species by studying its properties and constructing the antenna required to drive the transition between states. The purpose is to broaden the scope of LMU's methods and research directions. In this manner, we can establish the current context and briefly describe the content structure of the chapters of this thesis.

We introduce in Chapter 1 the ^{6}Li system, starting by studying its hyperfine levels, and we determine the ground state (2^2S), giving the principal elements used for cooling. Then, we discuss some properties of the fermion nature of ^{6}Li, preparing to describe the experimental setup of the LMU.

In Chapter 2, we explore the behavior of neutral fermions trapped at very low temperatures. We explore two spin-fermionic species in a harmonic trap interacting at low energies. Here, we use the scattering theory to remark the principal highlights of indistinguishable fermions and to bind pairs. The scattering between pairs and bound states are described by a parameter known as $s-$wave scattering length, a_s, which depends strongly on the magnetic field. For the special case of ^{6}Li, we manipulate the interactions via an external magnetic field produced by a current source. This phenomenon is called *Feshbach Resonances*.

In Chapter 3, we review the Zeeman effect to find a third state accessible using a radiofrequency (RF) excitation. The technique to obtain the third species is applying an RF

emission from an antenna designed and developed in this work. The antenna was made to meet the required conditions of the experiment. We present the final and functional model of the antenna and the experimental protocol to add to the experimental setup of the LMU.

All measurements performed with the RF antenna are presented in Chapter 4. We start the test of the antenna in the non-interacting region (52.7 mT) for the two lowest hyperfine states, in other words, the *zero-crossing* value of the scattering length. In the next sector in the BEC region (73.0 mT), two of the three available pairs exhibit identical scattering lengths. We explore RF transitions for this magnetic field and show the spectroscopy results for the transferred states and the representative Rabi oscillations.

The closing of this work is presented in Chapter 5, which highlights the most important results and gives an overview of the perspectives that can be applied. We emphasize that the results presented here correspond to the specific conditions of the LMU.

Chapter 1

Lithium system in the LMU

The study of macroscopic quantum systems began not so long ago [25], and the first feasible experiments in this area are even closer. We will briefly explore the primary concepts and preliminary aspects of atomic physics, statistical physics, and the experimental procedure. We start the chapter by introducing the fermionic atom of Lithium, which is a fundamental tool for developing the research at LMU. It is important to note that in this chapter, we discuss how this alkaline atom is considered, following the answer to *why LMU selected* ^{6}*Li*.

1.1 Lithium-6 as hydrogen-like atom

The lithium atom is the second element in the periodic table with a unique valence electron. With its $n = 1$ shell fully occupied, it becomes the first neutral alkali atom with a nucleus containing more than one proton. For this reason, lithium is a suitable candidate for applying hydrogen-like atom model to determine its ground state and electronic configuration. Consequently, the ground state of the lithium atom is $^2S_{1/2}$. The presence of a filled inner shell results in an effective shielding effect.

In nature, there are two stable isotopes of lithium, ^{7}Li with four neutrons and ^{6}Li with only three. The basic difference between these isotopes is the statistics that follow: ^{7}Li is a boson, while ^{6}Li is a fermion, whose relative abundance for ^{7}Li is 92.2% and ^{6}Li is 7.8%. Due to the imbalance, our samples are enriched. Table 1-1 summarizes some fundamental physical properties of atomic ^{6}Li taken from [26, 27].

1.1.1 The Fine Structure

The electronic configuration of the ground state for ^{6}Li is $1s^2 2s^1$, while the first excited state configuration is $1s^2 2p^1$. The difference in energy between both states is accessible optically, around 671 nm, a red transition in the visible spectrum. The standard framework to obtain the energy levels of this atom is through the central-field approximation, which refers to the valence electron as independent and assumes that the nucleus and the closed inner electron shells generate a spherically symmetric electric field.

Property	Symbol	Value	Reference
Atomic Number	Z	3	
Nucleons (Number Mass)	A = Z + N	6	
Natural abundance	η	7.59(4)%	[28]
Atomic Mass	m	$9.988\ 341\ 4(2)\times10^{-27}$ kg	[29]
Total electronic spin	S	1/2	
Total nuclear spin	I	1	
Nuclear magnetic momentum	μ	$0.822\ 044\ 63(37)\mu_N$	[30]

Table 1-1: Recap of physical properties of ^{6}Li.

The first consideration is the effect of the spin from the valence electron, $\hat{\mathbf{S}}$, on the orbital momentum of its orbit, $\hat{\mathbf{L}}$, better known as the spin-orbit coupling. In simple terms, we can simplify the interaction by dipolar approximation. The Hamiltonian term that describe this interaction in the mentioned approximation is [31]:

$$\hat{\mathcal{H}}_{\mathrm{SO}} = \frac{e}{2\mathrm{m}_e^2 c^2 \hbar^2}\left(\frac{1}{r}\frac{d\Phi}{dr}\right)\hat{\mathbf{L}}\cdot\hat{\mathbf{S}}, \tag{1-1}$$

where m_e is the mass of the valence electron, c is the speed of light, and $\hbar$ is Planck's constant. r is the relative position of the electron in the central field, and Φ is the electric potential given by the Coulombian interaction with the effective presence of the nucleus and electron shell.

Following the hydrogen atom treatment, we define the total electronic angular momentum, $\hat{\mathbf{J}}$, as a sum:

$$\hat{\mathbf{J}} = \hat{\mathbf{L}} + \hat{\mathbf{S}}. \tag{1-2}$$

The eigenvalue associated with $\hat{\mathbf{J}}$ is J, which is given by the sum of angular momentum (1-2), and satisfies the restriction

$$|L - S| \leq J \leq L + S. \tag{1-3}$$

L and S are the quantum numbers associated with orbital angular momentum and electron spin.

In this basis, the spin-orbit coupling term can be expressed through the operator $\hat{\mathbf{J}}^2$:

$$\hat{\mathbf{J}}^2 = \hat{\mathbf{L}}^2 + \hat{\mathbf{S}}^2 + 2\hat{\mathbf{L}}\cdot\hat{\mathbf{S}}. \tag{1-4}$$

Using this relation, we can identify that the set of operators $\hat{\mathbf{J}}^2$, $\hat{\mathbf{L}}^2$, $\hat{\mathbf{S}}^2$ and the projection $\hat{\mathbf{J}}_3$ define the complete set of a commuting system in the coupled basis $|L, S; J, m_J\rangle$[1]. We conveniently substitute the form of (1-4) into (1-1) and used the perturbation theory [32], we

[1]The uncoupled basis take in count the squared operators $\hat{\mathbf{L}}^2$ and $\hat{\mathbf{S}}^2$, with its respective projections $\hat{\mathbf{L}}_3$, $\hat{\mathbf{S}}_3$, and the basis in the ket representation is $|L, S; m_L, m_S\rangle$

obtain the shift of energy:

$$\Delta E_{\mathrm{SO}} = \frac{\zeta}{2}\left[J(J+1) - L(L+1) - S(S+1)\right], \tag{1-5}$$

where,

$$\zeta = \frac{e}{2\mathrm{m}_e^2 c^2 \hbar^2}\left\langle \frac{1}{r}\frac{d\Phi}{dr}\right\rangle. \tag{1-6}$$

We are interested in the ground and the first excited states of the ^{6}Li. In the spectroscopy representation, the ground state ($L = 0$ and $S = 1/2$) corresponds to the term 2^2S, and the excited state ($L = 1$ and $S = 1/2$) is 2^2P. Using (1-3), we check that the fine structure for the ground state has a shift, and the spectroscopy representation adds the J-value: $J = L + S = 0 + 1/2 = 1/2$; therefore we have $2^2S_{1/2}$. In the other case, the 2^2P state, where a degeneracy exists, and the fine structure separates into two levels given by the two possible values given by (1-3), $J = 1/2, 3/2$. Then, the spectroscopy nomenclature for these two states is $2^2P_{1/2}$ and $2^2P_{3/2}$, respectively.

As we depicted in the sketch of Fig. 1-1, both possible transitions $2^2S_{1/2} \leftrightarrow 2^2P_{1/2}$ and $2^2S_{1/2} \leftrightarrow 2^2P_{3/2}$ are the $D-$lines spectroscopy transitions. These two spectral lines are used to calibrate the laser frequencies employed in the experimental cooling of the atoms. The main properties of transitions $D_1 : 2^2S_{1/2} \leftrightarrow 2^2P_{1/2}$ and $D_2 : 2^2S_{1/2} \leftrightarrow 2^2P_{3/2}$ are collected into the Table 1-2 and Table 1-3 respectively [2].

Property	**Symbol**	**Value**	**Reference**
Wavelength (vacuum)	λ	670.992 477 nm	†
Wavenumber (vacuum)	$\mathrm{k}/2\pi$	14 903.296 792(23) cm^{-1}	[33, 34]
Frequency	ν	446 789 596.109 4(8) MHz	[35, 36]
Lifetime	τ	27.1055(10) ns	[34]
Natural Linewidth	Γ	5.872 4 MHz	†
Saturation Intensity	I_{sat}	7.59 $\mathrm{mW/cm}^2$	†

Table 1-2: Optical properties of the spectroscopy D_1-line of ^{6}Li. The † symbols represent quantities analytically derived from measured values

Property	**Symbol**	**Value**	**Reference**
Wavelength (vacuum)	λ	670.977 380 nm	†
Wavenumber (vacuum)	$\mathrm{k}/2\pi$	14 903.632 116(18) cm^{-1}	[33, 34]
Frequency	ν	446 799 648.889 8(16) MHz	[35, 36]
Lifetime	τ	27.1025(5) ns	[34]
Natural Linewidth	Γ	5.872 4 MHz	†
Saturation Intensity	I_{sat}	2.54 $\mathrm{mW/cm}^2$	†

Table 1-3: Optical properties of the spectroscopy D_2 line of ^{6}Li. The † symbols represent quantities analytically derived from measured values

[2] We omit some uncertainties because they are orders of magnitude smaller than those presented here.

1.1.2 The Hyperfine Structure

The presence of the nucleus introduces a new correction to energy; it is known as *hyperfine structure*. In this form, the structure arises from $\hat{\mathbf{J}}$, and the nuclear angular momentum, $\hat{\mathbf{I}}$. The following Hamiltonian gives the hyperfine term,

$$\hat{\mathcal{H}}_{\text{hf}} = A\hat{\mathbf{I}} \cdot \hat{\mathbf{J}}. \tag{1-7}$$

The constant A is determined by measuring this coupling. As in the fine structure, we define the total atomic angular momentum $\hat{\mathbf{F}}$ as the sum $\hat{\mathbf{J}} + \hat{\mathbf{I}}$. Thus, the eigenvalue F is restricted by the expression

$$|J - I| \leq F \leq J + I. \tag{1-8}$$

We can apply the same treatment in fine structure, which gives the general expression for the energy shift correction and has the following solution

$$\Delta E_{\text{hf}} = \frac{A}{2}\left[F(F+1) - J(J+1) - I(I+1)\right]. \tag{1-9}$$

Considering the $2^2S_{1/2}$ state, then $J = S$, and $F = I \pm 1/2$. Furthermore, particularly the ^{6}Li has a nuclear atomic spin $I = 1$. For this reason, the degeneracy of the ground state breaks into two energy levels labeled by the quantum numbers $F = 1/2$ and $F = 3/2$. The separation between these states is

$$\Delta E_{\text{hf}}(F = 3/2) - \Delta E_{\text{hf}}(F = 1/2) = (I + 1/2)A = \tfrac{3}{2}A. \tag{1-10}$$

Following these ideas in the ^{6}Li ground state, we can establish the value for the splitting $\Delta E_{\text{hf}}(2^2S_{1/2}) = 228.205\ 259(3)$ MHz and the hyperfine constant $A = 152.136\ 839(2)$ [37, 38].

1.2 The influence of electric and magnetic fields

External electric and magnetic fields are essential in atomic experiments, as they influence the energy states of atoms. This section briefly reviews how these external potentials affect atomic energy levels, a crucial consideration when working in the ultra-low temperature regime.

1.2.1 The Electric Field

The natural response of the atom is to be polarized under the influence of an external electric field $\mathbf{E}$, such as those generated in laser cooling and trapping techniques. This condition represents the existence of an atomic electric dipole moment $\mathbf{d}$. The interaction term, under the dipole approximation, is given by the expression [31]

$$\hat{\mathcal{H}}_{\text{SE}} = -\hat{\mathbf{d}} \cdot \mathbf{E}. \tag{1-11}$$

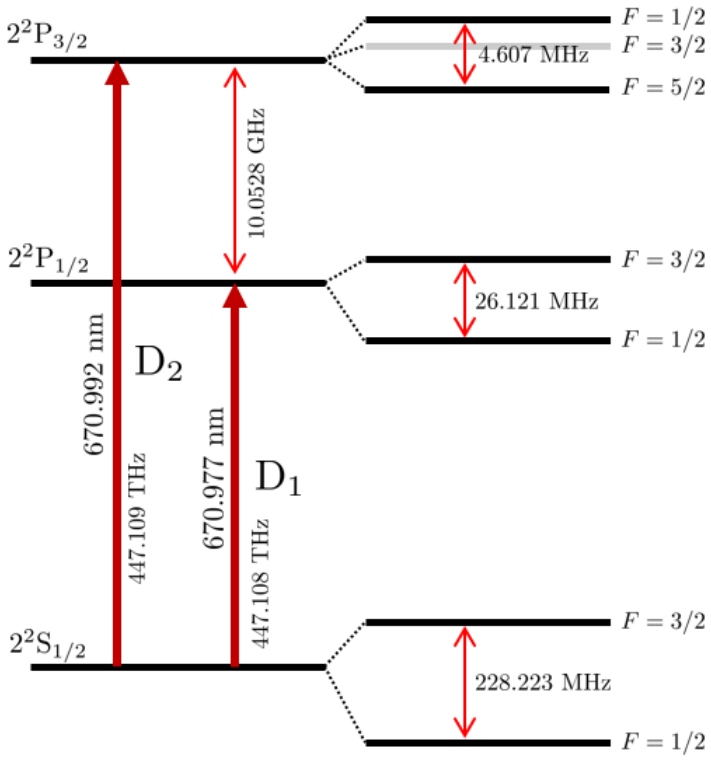

Figure 1-1: Diagram of the splitting energy for the states of ^{6}Li in the consideration of the fine and hyperfine structure.

This Hamiltonian modifies the energy levels of the atoms; this effect is known as the Stark effect [39]. When the contribution is smaller than the kinetic or potential energies, the treatment to obtain these energy shifts is through the perturbation theory. In the absence of an external field, there is no dipole moment; for this reason, the first-order correction vanishes [40]. Then, the first non-vanishing correction is the second-order term for the ground state, which is given by

$$\Delta E = \sum_n \frac{\left|\langle n|\,\hat{\mathcal{H}}_{\mathrm{SE}}\,|0\rangle\right|^2}{E_0 - E_n}, \tag{1-12}$$

where the energy of the ground state is E_0, the subindex n represents all the excited states.

The atomic polarizability, denoted by α, corresponds to the expectation value of the electric dipole moment operator. While polarizability is generally a tensor quantity, it reduces to a rank-0 tensor, i.e., a scalar, for the ground states of alkali atoms. In these cases, the dominant contribution arises from the valence electron. Compared to hydrogen, whose polarizability is given by $\alpha_{\mathrm{H}} = (4\pi\epsilon_0)\cdot(9a_0^3/2)$, alkali atoms exhibit polarizabilities that are approximately 30 to 90 times larger [40]. This increase is primarily due to the greater number of electrons in the filled inner shells [41].

On the other hand, when an atom is placed in an electric field gradient, specific properties

of the field, such as intensity, polarization, and detuning, become crucial for controlling confined atoms. In particular, by employing electric fields that are far red-detuned from atomic transitions, one can generate a dipole force that can be used for the confinement and manipulation of atomic samples.

1.2.2 The Magnetic Field

We emphasize the effect of a magnetic field and use this to determine the transition shifts to manipulate the confined atoms. External magnetic fields are used in different stages of the experimental sequences, e.g., in the laser cooling process or the interaction tuning.

All the responses of atomic samples are called the Zeeman effect[3] [42,43]. We can describe this interaction with the Hamiltonian term

$$\hat{\mathcal{H}}_{\mathrm{ZE}} = -\hat{\boldsymbol{\mu}} \cdot \mathbf{B}, \tag{1-13}$$

where operator $\hat{\boldsymbol{\mu}}$ represents the total magnetic moment of the atom, which is related to the sum of the electronic and nuclear moments, as follows

$$\hat{\boldsymbol{\mu}} = -g_J \mu_{\mathrm{B}} \hat{\mathbf{J}} + g_I \mu_{\mathrm{N}} \hat{\mathbf{I}}. \tag{1-14}$$

The correction of the energy levels by comparing the strength of the interaction term between the magnetic field $\hat{\mathcal{H}}_{\mathrm{Z}}$, and the hyperfine coupling term $\hat{\mathcal{H}}_{\mathrm{hf}}$ given by the eq. (1-7). Thus, the interaction term (1-13) as modified by the following term

$$\hat{\mathcal{H}}_{\mathrm{ZE}} = -\frac{1}{\hbar}\left(\mu_B g_J \hat{\mathbf{J}} - \mu_N g_I \hat{\mathbf{I}}\right) \cdot \hat{\mathbf{B}}, \tag{1-15}$$

where μ_B is the Bohr magneton, μ_N is the nuclear magneton, and g_J and g_I are the *Landé* factors for the electron and nucleus, respectively.

We separate the study of this effect into three parts [32]. In the first case, we have the weak strength region of the magnetic field, characterized by the relation $|\mathcal{H}_{\mathrm{Z}}| \ll |\mathcal{H}_{\mathrm{hf}}|$. For this case, we use the coupled basis $|F, J, I; m_F\rangle$ and take $\mathcal{H}_{\mathrm{Z}}$ as a perturbation. The energy shift is $\Delta E = (\mu_B/\hbar) g_F m_F |\mathbf{B}|$, where the coefficient [44]

$$g_F = g_J \frac{F(F+1) + J(J+1) - I(I+1)}{2F(F+1)} + g_I \frac{F(F+1) + I(I+1) - J(J+1)}{2F(F+1)}.$$

In the opposite case, where $|\mathcal{H}_{\mathrm{Z}}| \gg |\mathcal{H}_{\mathrm{hf}}|$, we have the strong limit known as the Paschen-Back region. As a consequence, the Zeeman term dominates the dynamics; therefore, the appropriate basis is the uncoupled basis $|J, I; m_J, m_I\rangle$. Here, the energy shift becomes $\Delta E = (\mu_B/\hbar)\left(g_J m_J + g_I m_I\right)|\mathbf{B}|$. At last, the intermediate case that connects both extremes corresponds to the Breit-Rabi regime, where $|\mathcal{H}_{\mathrm{Z}}| \approx |\mathcal{H}_{\mathrm{hf}}|$. There is no general analytical

[3] Zeeman has won the Nobel Prize for his studies on the effects on the energy levels of atoms under an external magnetic field.

solution to the shift energy for cases where any of the quantum numbers are different from 1/2 [41]. Fortunately for our purposes, in the ground state of Lithium ($L = 0, S = 1/2$), as well as for any hydrogen-like atom, there exists an analytical solution known as the Breit-Rabi formula [45]:

$$\Delta E(F, m_F) = -\frac{\Delta E_{\text{hf}}}{2(2I+1)} + g_I \mu_N |\mathbf{B}| m_F \pm \frac{\Delta E_{\text{hf}}}{2}\left(1 + \frac{4m_F\epsilon}{2I+1} + \epsilon^2\right)^{1/2}. \tag{1-16}$$

Note, that we use the dimensionless quantity $\epsilon = (\mu_B g_J + \mu_N g_I)|\mathbf{B}|/\Delta E_{\text{hf}}$, and the hyperfine energy shift $\Delta E_{\text{hf}} = A(I + 1/2)$ presented in (1-10).

1.3 Working with a fermion isotope

We have discussed the natural analysis of a hydrogen-like atom, which is a main property of the ^{6}Li. However, we need to check the other characteristic of this isotope, which is its fermionic nature. For indistinguishable particles, we identify two classifications: *boson* and *fermion*. The former, bosons, possess a symmetric wave function and purely integer spins. The latter, fermions, their wave function is antisymmetric and has half-integer spins. This classification is the connection between spin and statistics proposed by Pauli [46]. In statistical physics, we use the Bose-Einstein (BE) distribution for bosons and the Fermi-Dirac (FD) distribution for fermions.

This work focused on fermionic atoms. Their statistic, in this case is determined by the number of neutrons and protons in the nucleus and the valence electrons [40]. Considering only the valence electron in the atomic structure for an odd number of nucleons, i.e., the sum of neutrons and protons, we have a fermion.

One of the most relevant differences between fermions and bosons is the degeneracy of their ground state. There are no limitations for bosons for two or more identical bosons to occupy the same quantum state, which can derive in the macroscopical phenomena of BEC. This phenomenon does not occur for fermions because the Pauli principle of exclusion forbids it. The result of this occupancy of every energy level under the Fermi energy, E_{F}, which is the last occupied energy state. This state is called *Fermi Sea*.

1.3.1 Free Fermi Gas

We consider a system of N identical fermions that satisfy the FD distribution, which in the Grand canonical ensemble is [47]

$$f(E, \mu, T) = \frac{1}{e^{(E-\mu)/k_{\text{B}}T} + 1}. \tag{1-17}$$

This expression describes the occupation probability with energy E, a chemical potential μ, and temperature T of the system. The chemical potential μ is fixed by the condition of the

conservation of the total number of fermions N, which is given by the expression:

$$N = \int f(E)g(E)dE, \tag{1-18}$$

where $g(E)$ is the density of states with energy E.

At zero temperature, the chemical potential corresponds to the energy of the last occupied state, i.e., E_{F}, and has the following form

$$E_{\mathrm{F}} \sim \mu(N, T = 0). \tag{1-19}$$

The Fermi energy defines a natural energy of the system, which allows us to compare different physical properties. For example, we can define the Fermi temperature as

$$T_{\mathrm{F}} = E_{\mathrm{F}}/k_{\mathrm{B}}, \tag{1-20}$$

or the Fermi wave number,

$$k_{\mathrm{F}} = \sqrt{(2\mathrm{m}E_{\mathrm{F}})}/\hbar. \tag{1-21}$$

In this limit, eq. (1-17) is a Heaviside (step) function

$$n(E, T = 0) = \begin{cases} 1, & E < \mu \\ 0, & E > \mu. \end{cases} \tag{1-22}$$

To find an explicit form of eq. (1-18), we need to consider a homogeneous system[4], and the consideration of the spin s given by our fermions. Taking as volume V and taking $V \to \infty$ to replace the sum for an integral over all the space[5].

Thus, integrating the density of states $g(E) \propto \sqrt{E}$, and multiply by the distribution (1-22), we obtain

$$N = \frac{2s+1}{(2\pi)^3} V \int_{|\mathrm{k}|<|\mathrm{k_F}|} d^3\mathrm{k} = \frac{2s+1}{(2\pi)^3} \frac{4\pi V}{3} \mathrm{k}_{\mathrm{F}}^3. \tag{1-23}$$

Reordering this equation, we can write the Fermi moment as:

$$\mathrm{k}_{\mathrm{F}} = \left(\frac{6\pi^2 n}{2s+1} \right)^{1/3}, \tag{1-24}$$

with $n = N/V$. Therefore, the Fermi energy is

$$E_{\mathrm{F}} = \frac{\hbar^2}{2\mathrm{m}} \left(\frac{6\pi^2 n}{2s+1} \right)^{2/3}. \tag{1-25}$$

The expression for E_{F} is just an introduction to the next chapter, considering two species

[4] In Chapter 2 we study the harmonic trapped case.

[5] We are substituting $\sum_r \to (2s+1)\frac{1}{\Delta \mathrm{k}} \int d^3\mathrm{k}$.

for fermions distinguishable by their spin projections. As we mentioned, the LMU can explore the properties of superfluidity through interactions between pairs of fermions. At this point, we do not consider two non-identical species of fermions.

The following describes the experimental setup and explains how we obtained these two components. Then, in the following chapter, we discuss the properties of the interactions between the fermionic atoms of Lithium below the critical temperature.

1.4 The experimental sequence in the LMU

Obtaining a degenerate Fermi gas requires a rigorous process, which takes only 14 seconds, which is the time duration of a conventional routine to create a quantum gas of Lithium. This section explains the experimental sequence from the cooling process to the imaging system.

We begin with an oven with a total thermal classical gas. At the final stage, we obtain an integrated density distribution of the quantum cloud by the absorption imaging process [48]. The shadow of the samples shows a cigar-shaped geometry, and we load it in imaging software developed for this proposal. After that, we analyze and obtain the physical parameters, such as temperature, number of atoms, optical density, widths, etc.

1.4.1 Zeeman Slower

The ^{6}Li are supplied by an oven operating at a temperature of approximately 720 K. This oven releases the atoms in a gaseous state, which are expelled and accelerated through a nozzle ($\sim 400\ \mu$m) to form a highly directional atomic beam. The atomic flux, initially moving at the velocity near 800 $\mathrm{m \cdot s^{-1}}$, enters the first cooling stage: the Zeeman slower [49]. This device consists of a set of magnetic coils arranged along a tube with 56 cm of length, generating a maximum magnetic field of 80 mT. The primary function of the Zeeman slower, as its name implies, is to reduce the atomic beam velocity to 15 $\mathrm{m \cdot s^{-1}}$, enabling efficient capture of the atoms for the next stages in the main chamber or "science chamber".

The Zeeman slower works by combining an inhomogeneous magnetic field with a counter-propagating laser beam relative to the atomic motion. The laser interacts with the atoms so that their internal structure is in resonance, inducing gradual deceleration. As the atoms are in motion, they present the Doppler effect, and to compensate for it, the magnetic field adjusts the resonance frequency via the Zeeman effect. The inhomogeneity of the magnetic field allows the atoms to remain in resonance with the laser frequency throughout the deceleration process. Additionally, the laser frequency is red-detuned by approximately $\sim 70\Gamma$, where Γ is the natural linewidth of the atomic transition shown in Tables 1-2 and 1-3. Appendix A discusses the significance of frequency shifts for accommodating the specific requirements of each process.

Upon completion of this cooling stage, the ^{6}Li atoms reach a mean velocity of 15 $\mathrm{m \cdot s^{-1}}$, corresponding to a temperature of approximately 150 mK.

1.4.2 Magneto-Optical Trap

In the outside science chamber, a pair of coils arranged in *anti-Helmholtz* configuration is positioned, i.e., the current is counter-flowing in each coil. These coils carry a current of approximately 40 A. They are submerged in a water flow to maintain their room temperature at around 290 K and prevent them from heating up and affecting their functioning. Anti-Helmholtz configuration creates an inhomogeneous magnetic field featuring a zero-point at its center, with an axial gradient of about 0.30 $\mathrm{T} \cdot \mathrm{m}^{-1}$.

At the null region magnetic field, the geometric center between the coils, six counter-propagating laser beams intersect, each with a diameter of approximately 2.54 cm. This combination of magnetic fields and laser light forms a magneto-optical trap (MOT). Each laser beam incorporates two frequencies: a repumping and a cooling beam in the D_2 transition ($2^2S_{1/2} \rightarrow 2^2P_{3/2}$); as shown in Fig. 1-1. The repumping beam is red-detuned by approximately 10Γ, while the cooling beam is red-detuned by 8Γ.

This configuration allows for confining the cloud in configurational and velocity spaces, and producing a sample of 10^9 atoms at the temperature of 5 mK.

1.4.3 Bright and Gray Molasses

The magneto-optical trap (MOT) is constrained by a cooling limit imposed by photon scattering, known as the Doppler limit [50], which in our case is around the 150 μK. In this form, additional techniques must be implemented to overcome this barrier. The first method, although inefficient, is named D_2 bright molasses. This technique involves the free expansion of the MOT atoms for 0.5 ms, using a red-detuned frequency from another cooling laser relative to the D_2-transition. Counter-propagating laser beams generate a polarization gradient that induces Sisyphus cooling[6]. However, a critical physical limitation arises because the hyperfine splitting of the excited state in the D_2-line is comparable to the natural linewidth (Γ), i.e., around 6 MHz, which makes bright molasses inefficient [52].

A second cooling stage is implemented using the D_1 transition ($2^2S_{1/2} \rightarrow 2^2P_{1/2}$); see Fig. 1-1. This technique, known as gray molasses, reduces the temperature of the atoms previously cooled in the bright molasses. In this form, the gray molasses combine Sisyphus cooling and velocity-selective coherent population trapping (VSCPT) [53, 54]. The tuning of the light beams prepares the sample to obtain exclusively the ground state of ^{6}Li: $2^2S_{1/2}$.

This technique for ^{6}Li has been reported in the literature [55, 56], with similar results achieved at LMU [57, 58]. After implementing gray molasses, the temperature of 10^8 atoms can be reduced to approximately 50 μK.

[6]Optical pumping technique based on the transfer of population between the different sub-levels of the ground configuration [51]

1.4.4 Optical Dipole Trap

At the end of the last stage, the atoms are in optimal conditions to be transferred to a conservative trap, which, in our case, corresponds to an Optical Dipole Trap (ODT) combined with a curved magnetic field. After multiple sub-Doppler cooling, the ODT is charged to a maximum power of around 200 W of a far-detuned laser beam. The detuning concerning any transition of the hyperfine structure of ^{6}Li, in this case, an infrared (IR) laser beam with a wavelength of 1069 nm.

The ODT is not a collimated laser beam; it is tightly focused at 50 μm centrally inside the science chamber, and aligned with the cloud to maximize transfer efficiency. In order to optimize this transference, the cold cloud is positioned with coils that generate a magnetic field compensation. When the atoms interact with ODT, they behave as induced dipoles and become confined within the focused region characterized by the Rayleigh length [59], approximately 7 mm in this setup.

The curvature of the conservative gradient arises from the field generated by the Feshbach coils. In fact, the magnetic field has two goals: to confine the sample in the center and to manipulate the interactions.

1.4.5 Evaporative Cooling

We finalize with a process known as *evaporative cooling*, which is implemented for a harmonic trap [60]. Evaporative cooling consists of ramping down the ODT high-power intensity to a low power to reduce the potential bowl and obtain only the most cooled atoms; the rest is evaporated, i.e., the "warmed atoms" are let off the trapping.

The ramp process consists of two parts: the first is an exponential decrease ramp from the high-power 195 W to 6 W, executed by the ODT during 2 seconds; the second is an exponential decrease ramp, from the ~ 6 W to the last power around 30 mW. This sequence takes 1.5 seconds to obtain the quantum degeneracy with typical equilibrium phase parameters, including temperatures < 100 nK and a population of approximately 10^4 atoms.

1.4.6 Feshbach coils

As mentioned, to manipulate the quantum gas interaction, a magnetic field is tuned for ^{6}Li sub-Zeeman states of the ground state $2^2S_{1/2}$, particularly $F = 1/2$ with projections $m_{\mathrm{F}} = \pm 1/2$. The coils in the Helmholtz configuration, i.e., currents flowing in the same direction, produce the required magnetic field. Beyond the central plane between the coils, the magnetic field displays a slight curvature that can confine atoms in one spatial dimension of our interest, in this case, the direction of propagation of the ODT beam, a feature exploited for the conservative trap [2].

The Feshbach coils are placed along the gravity axis of the science chamber. The magnetic field at the center of the chamber is, for the ultracold atomic sample, constant and aligned with the vertical axis, $\mathbf{B}_{\mathrm{F}} = B_0 \mathbf{e}_z$. The target value of the B_0 is selected during the last

evaporative ramp described above. It corresponds to the resonance value of the interactions of the two atomic hyperfine projections m_F, $B_0 = 83.4$ mT, corresponding to a flux current of ~ 160 A. The collision rate is high because the gas at this magnetic point has a stronger interaction.

Moreover, to reach other values of B_0, in other words, to reach other interaction regimes, we execute a magnetic field sweep during 100 ms. The current values that set the magnetic fields were calibrated considering the Breit-Rabi formula (1-16), which allows us to observe the degenerate atomic gas in different regimes. Since Feshbach resonances are linked to the nature of interactions, we will explore their origin in Chapter 2.

1.4.7 High resolution Imaging System

Currently, the LMU utilizes two imaging systems:

- Diagnostic imaging determines the atomic number, temperature, and spatial geometry. This imaging system consists of a CCD camera and optical elements placed perpendicular to the axis of gravity. This setup was mounted over the platform with the optics, with horizontal access to the science chamber. The layout comprises optical devices that obtain the destructive image of the sample. This action is destructive to the state of the cloud because we use the absorption technique image [48]. The CCD camera acquires the light pulses of ~ 4 μs.

- High-resolution imaging, customized for research objectives. This image has optical access on the vertical axis, i.e., along with gravity, and another CCD camera is located on a platform over the science chamber. A custom high-resolution microscopy system was designed and implemented by LMU [61]. This system achieves high magnification ($\times 7$) and required spatial resolution (< 2 μm), enabling precise observation of collective excitations within the Bose-Einstein condensate (BEC) [62].

As seen in Fig. 1-2, the image requires a mathematical computation of three matrix arrays for each shot image. The first is light with a *shadow* given for the absorption of the atoms; the second array consists of light without atoms (previously removed by the first light); and one last array is the background (no light present), just a picture of the environment light received by the CCD. The analysis of these arrays is described in the thesis of LMU [62].

The physical parameters of the cloud are extracted through image processing. Here, we have just mentioned the fundamental concepts and techniques used. The relation between the incident light intensity I_0 and the transmitted I is given by the Beer–Lambert law [51], which allows us to determine the optical density (OD) of the sample, i.e., the amount of light absorbed. This is expressed as $\mathrm{OD} = -\ln(I/I_0)$.

The optical density is directly related to the atomic density along the propagation axis of the imaging beam via $n(x, y) = \mathrm{OD}(x, y)/\sigma$, where σ is the absorption cross-section. In this form, we obtain the two-dimensional density distribution of the atomic sample. Then, the

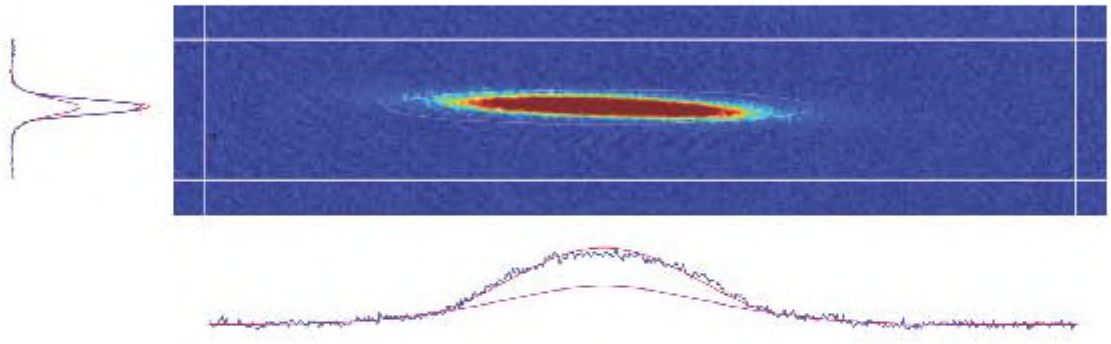

Figure 1-2: In situ absorption image of a molecular Bose-Einstein condensate (BEC) formed from ^{6}Li. The side panels show the integrated optical density (OD) profiles along the vertical and horizontal directions.

total number of atoms is determined by integrating the density profile $n(x, y)$ across the two spatial dimensions of the imaging plane.

Another fundamental property of the system is the temperature, which to be measured requires releasing the cloud from the confinement potential, a procedure known as time-of-flight (TOF) [63]. As shown in Fig. 1-2, the density distribution in the image can be projected onto each axis, yielding one-dimensional profiles from which the widths $s_{x,y}$ can be extracted. The evolution of these widths over the TOF provides an estimate of the expansion velocity. Consequently, the temperature can be approximated as $T = \frac{m}{k_B}\left(\frac{ds_{x,y}}{dt_{\mathrm{TOF}}}\right)^2$.

1.4.8 Control System

Every field, light beam, laser, and electronic device forming the Fermi degenerate gas is controlled via a custom program developed in LabVIEW® for fermionic superfluid experiments. The program synchronizes sequences of instructions through routines that include analog signals (e.g., ramps for the ODT or magnetic field sweeps) and digital signals (e.g., triggers for devices requiring operational commands, such as shutters). These instructions are compiled into a synchronized sequence within the control software [64].

The digital and analog signal-generating cards are homemade in a rack as a control hub. The timing resolution between sequential instructions is 1 μs, ensuring precise coordination, from tenths of μs to hundredths of s in all experimental parameters and sequences.

Chapter 2

The two body interactions in the dilute sample

Our interest is focused on how the hyperfine fermionic species interact at low temperatures inside an external potential. For this reason, we will explore in this chapter the main ideas that allow us to understand how the atoms behave in these conditions. We start by reviewing an ideal Fermi gas trapped in a harmonic potential. Then, we will consider a two-component system where the parameter of collisions governs the interactions. After that, we will identify the accessible regions for two non-identical fermions across the Feshbach resonances [2].

2.1 Trapped Fermi Gas

Before we turn our attention into the two-body interaction problem, we will make a technical stop to address the boring case of the non-interacting system called Fermi gas[1].

Then, we start with a set of N neutral fermions that in first quantization have the following Hamiltonian,

$$\hat{\mathcal{H}} = \sum_{\nu=1}^{N} \left(-\frac{\hbar^2}{2\mathrm{m}} \nabla_\nu^2 + V\left(\mathbf{r}_\nu, t\right) \right). \tag{2-1}$$

Considering a system of identical fermions, each with mass m.

It is important to keep in mind that this is a many-body problem. Therefore, we employ statistical physics, a powerful tool for treating many-body systems. We already presented the fermionic density distribution (1-23) but only considered a single spin species. Now, we present the version for non-identical species identified by the subindex σ,

$$\langle n_{\nu,\sigma} \rangle = \frac{1}{e^{(E_\nu - \mu_\sigma)/k_\mathrm{B}T} + 1}. \tag{2-2}$$

Reducing the calculations, two species were used without interactions. Here the chemical

[1] This is a habitual joke because in physics, the most closer to reality are situations where everything interacts with everything else. However, this simplified system provides us with much information.

potential, μ_σ, is fixed by the normalization condition [65, 66]

$$N_\sigma = \sum_\nu \langle n_{\nu,\sigma} \rangle \,. \tag{2-3}$$

In this manner, if the system has two spin species, they are usually represented as up-$\uparrow$ and down-$\downarrow$, then $\sigma = \uparrow, \downarrow$. We consider the system in contact with a reservoir [1], which lets us impose that the atom number $N_{\uparrow,\downarrow}$ is conserved in the trap.

The following expression describes the depth of confinement

$$V(\mathbf{r}) = \frac{\mathrm{m}}{2}\left(\omega_x^2 x^2 + \omega_y^2 y^2 + \omega_z^2 z^2\right). \tag{2-4}$$

The prolate trap in the LMU follows the relation between the trapping frequencies: $\omega_x \approx \omega_y > \omega_z$. The ratio of cloud size is around $15:1$. We define the geometric mean frequency as

$$\bar{\omega} = (\omega_x \omega_y \omega_z)^{1/3}, \tag{2-5}$$

a relation that continuously appears along the expressions.

We use an approximation, where the thermal energy $\beta \equiv k_\mathrm{B} T$ is much larger than the level spacing of the harmonic external potential $\hbar\omega_{x,y,z}$. Then, considering a phase space cell $\{\mathbf{r}, \mathbf{p}\}$, we obtain the occupation

$$f(\mathbf{r}, \mathbf{p}) = \frac{1}{e^{\left(\frac{\mathbf{p}^2}{2\mathrm{m}} + V(\mathbf{r}) - \mu_\sigma\right)\beta} + 1}. \tag{2-6}$$

Note that we consider $T \neq 0$ in this approximation, a thermal gas, which has a density distribution

$$n_{th,\sigma}(\mathbf{r}) = \int \frac{d^3\mathrm{p}}{(2\pi\hbar)^3} f(\mathbf{r}, \mathbf{p}) = -\frac{1}{\lambda_\mathrm{dB}^3} \mathrm{Li}_{3/2}\left(-e^{(\mu_\sigma - V(\mathbf{r}))\beta}\right). \tag{2-7}$$

We omit the subindex σ; the expression is for every spin. We have three important elements, the first one is the de Broglie wavelength given by

$$\lambda_\mathrm{dB} = \sqrt{\frac{2\pi\hbar^2}{\mathrm{m} k_\mathrm{B} T}}. \tag{2-8}$$

The second one is the Polylogarithm of order n, which is defined by the integral[2]

$$\mathrm{Li}_n(\mathrm{z}) = \frac{1}{\Gamma(n)} \int_0^\infty d\mathrm{t} \frac{\mathrm{t}^{(n-1)}}{e^\mathrm{t}/\mathrm{z} - 1}. \tag{2-9}$$

Another useful expression is the sum $\mathrm{Li}_n(\mathrm{z}) = \sum_{k=1}^\infty (\mathrm{z}^k/k^n)$. The last term to mention is the fugacity: $\mathrm{z} = e^{\mu\beta}$, representing the occupancy tendency of the particle to be in the state with

[2] Other notations in the literature use the letter f to express these functions from fermions ($f(\mathrm{z}) = -\mathrm{Li}_n(-\mathrm{z})$). We prefer to use the $\mathrm{Li}_n(\mathrm{z})$ form to avoid the excess or confusion with the notation of this work.

energy $E = \mu$.

If we take the $T = 0$ approximation, the function (2-6) becomes the step function, and (2-7) has the following form

$$n(\mathbf{r}) \to \int_{|\mathbf{p}|<\sqrt{2\mathrm{m}(\mu - V(\mathbf{r}))}} \frac{d^3\mathrm{p}}{(2\pi\hbar)^3} = \frac{1}{6\pi^2}\left[\frac{2\mathrm{m}}{\hbar^2}(\mu - V(\mathbf{r}))\right]^{3/2}. \tag{2-10}$$

We need to integrate over the entire configuration space to obtain the Fermi energy:

$$E_\mathrm{F} = \hbar\bar{\omega}\,(6N)^{1/3}. \tag{2-11}$$

The calculation at $T = 0$ serves as a reference for the case of finite-temperature. For the ultracold systems, the finite-temperature is considered $T \leq T_\mathrm{F}$. In this situation, the spatial profile of a trapped Fermi gas depends on the ratio $k_\mathrm{B}T/\epsilon_\mathrm{F}(\mathbf{r})$, where $\epsilon_\mathrm{F}(\mathbf{r})$ is the local Fermi energy. In the outer regions of the trap, where $k_\mathrm{B}T \gg \epsilon_\mathrm{F}(\mathbf{r})$, the gas behaves classically, $n(\mathbf{r}) \propto e^{-\beta V(\mathbf{r})}$. In the inner regions $k_\mathrm{B}T \ll \epsilon_\mathrm{F}(\mathbf{r})$, the density follows the zero-temperature form (2-10), i.e. quantum behavior. The transition between these regimes is smoothly captured by the Polylogarithm function (2-7) [1].

We seek to understand under what conditions these interactions occur for systems with two interacting fermions. The following section explores the conventional treatment for interactions between two particles under an ultralow temperature in a dilute sample.

2.2 Scattering problem at low temperatures

The next step to consider is that the particles interact in the case of two-body interactions. λ_dB is comparable to the interparticle distance in ultracold gases. Then, given a contact collision, the effects of the interacting potential decrease, making it a good approximation for the interactions of a dilute ultracold sample.

To study the quantum mechanical scattering of two neutral distinguishable bodies, we propose the time-independent Schrödinger equation for the two particles described by the wave function $\Psi(\mathbf{r}_1, \mathbf{r}_2)$. Using the standard procedure for the two-body system, we use the center-of-mass (CM) and relative coordinates frame. The reduced mass is $\mathrm{m}/2$ because the two atoms have the same mass. The free particle formalism governs the CM motion.

The ansatz wave function $\Psi(\mathbf{r}_1, \mathbf{r}_2)$ is transformed so that we consider only the relative coordinates in the laboratory frame. In this form, the wave function $\psi(\mathbf{r})$ describes a free particle approximation where the asymptotic region will see the short-range scattering effects (see Fig. 2-1). Then, we can propose the wave function after the collision as

$$\psi(\mathbf{r}) \to e^{i\mathbf{k}\cdot\mathbf{r}} + \psi_{out}(\mathbf{r}). \tag{2-12}$$

Far from the interaction region, the outgoing wave function component is described by a spherical wave multiply by a function $f(\mathbf{k}', \theta)$ called the scattering amplitude. The $\mathbf{k}'$ is

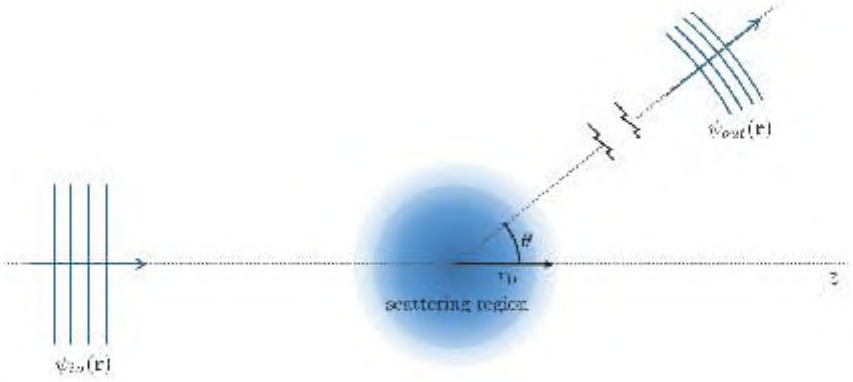

Figure 2-1: Schematic representation of the scattering problem, indicating study regions located far from the scattering zone (blue gradient).

the resulting scattered wave vector, and θ is the observation angle defined by the incident particle direction. Selecting the axis of motion of the incident wave as z and assuming that the interaction between the atoms is radially symmetric, then, the dependence of $\mathbf{k}'$ is negligible and the scattering wave is

$$\psi(\mathbf{r}) = e^{\imath \mathrm{k} z} + f(\theta)\frac{e^{\imath \mathrm{k} r}}{r}. \tag{2-13}$$

Another relevant quantity to take into account is the differential cross-section $d\sigma/d\Omega$, defined as the ratio of the current of probability per unit solid angle in the scattered wave divided by the current of probability per unit area in the incoming wave [66]. The relation with the scattering amplitude is given by

$$\frac{d\sigma}{d\Omega} = |f(\theta)|^2 . \tag{2-14}$$

The following procedure considers several approximations about the interaction, allowing the partial waves method to be used. This technique suitable for obtaining the explicit form of the scattering amplitude. However, it is only convenient in cases where the interaction potential is central and the kinetic energy is comparable to the interaction energy [67].

Expanding the wave function (2-13) in Legendre polynomials $\mathrm{P}_\ell(\cos\theta)$, as follows

$$\psi(\mathbf{r}) = \sum_{\ell=0}^{\infty} A_\ell \mathrm{P}_\ell(\cos\theta) R_{\mathrm{k}\ell}(r). \tag{2-15}$$

where A_ℓ are the expansion coefficient fot the $\ell-$term of the sum; $R_{\mathrm{k}\ell}(r)$ is the radial function in the relative coordinate r, which satisfied the radial equation [67]

$$R''_{\mathrm{k}\ell}(r) + \frac{2}{r}R'_{\mathrm{k}\ell}(r) + \left[\mathrm{k}^2 - \frac{\ell(\ell+1)}{r^2} - \frac{2m}{\hbar^2}U(r)\right] R_{\mathrm{k}\ell}(r) = 0, \tag{2-16}$$

with $U(r)$ the interaction potential. If we consider the asymptotic case of $r \to \infty$, the solution

of the radial function is

$$R_{\mathrm{k}\ell}(r) = A_\ell \mathrm{j}_\ell(\mathrm{k}r) + B_\ell \mathrm{n}_\ell(r). \tag{2-17}$$

The polynomials $\mathrm{j}_\ell(r)$ and $\mathrm{n}_\ell(r)$ are known as the spherical Bessel functions of first and second kind [68], respectively. Rewriting this last expression in terms of the *phase shift*, produced by the scattering potential for each ℓ component of the orbital angular momentum [67]; $\delta_\ell = \arctan(-B_\ell/A_\ell)$. Then,

$$R_{\mathrm{k}\ell}(r) = \frac{C_\ell}{\mathrm{k}r} \sin\left(\mathrm{k}r - \tfrac{\pi}{2}\ell + \delta_\ell\right). \tag{2-18}$$

Using the expansion in Legendre polynomials of eq. (2-13) and the expression obtained for the radial function (2-18), we can identify that $C_\ell = \imath^\ell\,(2\ell+1)\,e^{\imath\delta_\ell}$ and

$$f(\theta) = \frac{1}{2\imath\mathrm{k}} \sum_{\ell=0}^{+\infty} (2\ell+1)\left(e^{2\imath\delta_\ell} - 1\right) \mathrm{P}_\ell(\cos\theta). \tag{2-19}$$

Thus, the cross-section is obtained by integrating over the solid angle after making the substitution of (2-19) into (2-14). The cross-section has the following expansion

$$\sigma = \frac{4\pi}{\mathrm{k}^2} \sum_{\ell=0}^{\infty} (2\ell+1)\left(e^{2\imath\delta_\ell} - 1\right) \mathrm{P}_\ell(\cos\theta). \tag{2-20}$$

For a finite-range potential, the phase shift is proportional to $\mathrm{k}^{2\ell+1}$, being k small compared with the inverse of the effective range of the scattering potential $1/r_0$, called the limit of low energies [69]. Thus, all the partial amplitudes f_ℓ with $\ell \neq 0$ are smaller than $\ell = 0$. The lowest order is called $s-$wave scattering. Then, neglecting $\ell > 0$, the total amplitude is

$$f(\theta) \simeq f_{\ell=0} = \frac{1}{2\imath\mathrm{k}} \left(e^{2\imath\delta_0(\mathrm{k})} - 1\right). \tag{2-21}$$

Expanding the phase shift for $\ell = 0$ (see reference [67]), in a power series of k^2, takes the form

$$\mathrm{k}\cot\delta_0 = -\frac{1}{a_s} + \frac{1}{2} r_0 \mathrm{k}^2 + \mathcal{O}(\mathrm{k}^4). \tag{2-22}$$

r_0 is the effective distance of the scattering potential. Under the low energy approximation $\mathrm{k}r_0 \ll 1$, creating as a consequence one of the most relevant parameters for this work: *scattering length* of $s-$wave, defined by

$$a_s = \lim_{\mathrm{k}\ll r_0^{-1}} \left(-\frac{\tan(\delta_0)}{\mathrm{k}}\right). \tag{2-23}$$

The scattering amplitude (2-21), and the total cross section (2-20) can be expressed as follow

$$f(\theta) = -\frac{a_s}{1 + \imath\mathrm{k}a_s}, \qquad \sigma = \frac{4\pi a_s^2}{1 + (\mathrm{k}a_s)^2}. \tag{2-24}$$

In the case of $ka_s \ll 1$, typically for ultralow temperature gases, the total cross section is determined only by the scattering length.

The wave function $\psi(\mathbf{r})$ must reflect the symmetry character of the particles involved in the collision because the particles are identical. For the fermions case, the wave function is antisymmetric. The anti-symmetrized version of $\psi(\mathbf{r})$ give the modification of (2-14) into

$$\frac{d\sigma}{d\Omega} = |f(\theta) - f(\pi - \theta)|^2 . \tag{2-25}$$

Integrating this expression for $s-$wave scattering, we obtain that the total cross-section of the two identical fermions vanishes[3]. In this situation, the following term of the partial wave expansion is the $p-$wave $\ell = 1$. Here, the interaction of two identical fermions is possible. However, the $p-$wave scattering is suppressed due to the ultralow temperature regime.

2.3 Interaction of two distinguishable fermions

Back to the idea of having trapped fermions, now we can consider a balanced system of two fermionic species differing by the spin projection $\sigma = \uparrow, \downarrow$. As we studied before, these two classes of fermions can interact, and the scattering length of s-wave describes their interaction.

Obtaining a single parameter that describes the interaction is useful for classification and manipulation. For this task, it is more convenient to use the dimensionless parameter to measure the strength and sign of the interaction. The ratio[4] of the interatomic distance related with the scattering length is $(k_F a_s)^{-1}$.

Note that the cross sections are always positive, and it is zero only in the case of non-interacting channels. However, the a_s can take any sign, even be infinite, but the cross section remains always finite and positive. We discuss some limits to classify the main regions to form bound states.

2.3.1 Weak Repulsive Interactions

We begin with $(k_F a_s)^{-1} \to +\infty$, in this region, the fermions of opposite spin form weakly-interacting molecules, and their ground state is the BEC. This molecule behaves as a boson. For the weakly interacting gases of molecules, the system can be described by the Gross-Pitaevskii equation (GPe) [71, 72]

$$\imath\hbar\frac{\partial}{\partial t}\psi(\mathbf{r},t) = \left(-\frac{\hbar^2\nabla^2}{2M} + V_M(\mathbf{r}) + g|\psi(\mathbf{r},t)|^2\right)\psi(\mathbf{r},t). \tag{2-26}$$

The many-body wave function $\psi(\mathbf{r},t)$ in the equilibrium condition can be rewritten into a product of a time-dependent phase and a local-dependent wave function, i.e., $\psi(\mathbf{r},t) = \chi(t)\varphi(\mathbf{r})$.

[3] Opposite case for identical bosons, whose value is $8\pi a_s^2$.

[4] In the literature usually use the negative value, $\zeta = -(k_F a_s)^{-1}$, to describe this classification [70].

The mass M corresponds to the sum of the masses of the two fermions. Here, $V_M(\mathbf{r})$ is the confining external potential that the molecule feels.

The non-linear term of the GPe corresponds to the term of the mean-field. Factor g relates to the intensity of interactions between molecules, with a correction factor, and is given in terms of the $s-$wave scattering length as follows [73]

$$g = 0.6\frac{4\pi\hbar^2 a_s}{M}. \tag{2-27}$$

The analysis and study of the GPe to describe condensates is one of the most explored areas of many-body physics. However, we focus on the fermionic case, so the discussion of the BEC with the GPe formalism concludes here. For more information, we recommend the reference [66].

2.3.2 Weak Attractive Interactions

When the collision is weak and has a negative value in a_s, it means $(\mathrm{k_F}a_s)^{-1} \to -\infty$, the result is described by the BCS theory [74, 75]. The difference with the BEC interacting region is that the fermions with opposite spin and momentum form states called Cooper pairs [76]. The analogue of the mean-field GPe is the BCS Hamiltonian.

The cooling techniques limit the experimental accessibility of this region because it is necessary to drastically reduce the temperature below the Fermi temperature to obtain this superfluid state. The transition temperature T_c becomes exponentially small as one decreases the value of $T_c \approx 0.28\frac{E_\mathrm{F}}{k_B}e^{-\pi/(2k_\mathrm{F}|a_s|)}$ [77]. Moreover, one of the most significant results of the BCS theory is the gap equation (Δ). The gap tends to $\Delta \propto e^{-\pi/(2\mathrm{k_F}a_s)}$ [70, 77].

2.3.3 Strongly Interacting

When the scattering length diverges $a_s \to \pm\infty$, which corresponds to $\mathrm{k_F}a_s \to 0$, the fermions exhibit a universal behavior; for this reason, it is commonly called Unitary. In the universal quantum gas, the interatomic distance, given by $n^{-1/3}$, and the Fermi energy is the unique relevant quantity [78]. Remarkably, the resulting equation of state for this region is identical to the non-interacting Fermi gas (2-10) [1].

Recapitulating, Fig. 2-2 shows a phase diagram of the interactions between fermions distinguishable as a function of the temperature (compared with the Fermi temperature). The dashed line represents the temperature of molecule formation: above the line, the fermions are unpaired, and below the line, they start to form pairs. The full line represents the characteristic temperature to present superfluidity behavior in the ultracold sample.

We can observe that both lines of the diagram are different in the repulsive interaction region, describing three sections: above the pair formation temperature (a Fermi gas of two components), between pair formation and the presence of superfluidity (thermal molecules), and the region below the critical temperature (molecules that can form a BEC). The diagram

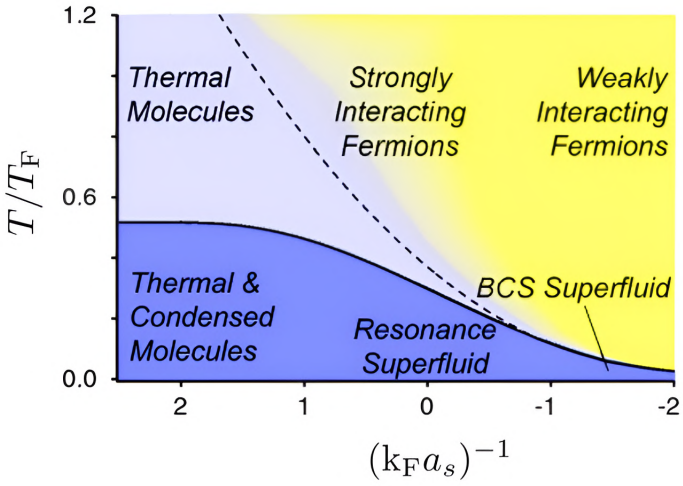

Figure 2-2: Phase diagram of interacting Fermi trapped mixtures as a function of the dimensionless temperature T/T_F. The solid line shows the critical temperature T_c for superfluidity, while the dashed line marks the pairing formation limit. Adapted from Ref. [1].

was originally constructed by [79], and this version is taken from [1].

2.3.4 Mean-Field Shift

We cannot ignore that we are working in the domain of many-body systems. Then, the interactions between atoms cause an energy shift, which is usually described by the mean-field effect. In other words, the atom interacts with the others in an effective interaction [22].

Thus, in a fermionic sample of two species (labelled as 1 and 2) in the low-energy regime, where s-wave collisions predominate, the energy difference between these two species will be

$$\Delta E_{12} = \hbar\nu_{12} + \hbar\nu_{\mathrm{mf}}. \tag{2-28}$$

ν_{12} is the natural resonance frequency for a non-interacting system, while the frequency ν_{mf} corresponds to the mean-field shift effect.

A formal deduction of this correction can be found in [66], but it will be sufficient to follow the qualitative deduction of [80]. As we have seen in the section on scattering, it is important to know that the colliding particles are distinguishable. The potential felt by a fermion with mass m is proportional to the atomic cloud of density

$$\mathsf{U} = \frac{4\pi\hbar a_s}{\mathrm{m}} n. \tag{2-29}$$

Turning back to the two species, the potential given in (2-29) leads us to know the explicit form of ν_{mf}, which is

$$\nu_{\mathrm{mf}} = \frac{4\pi\hbar a_{s_{12}}}{\mathrm{m}} n_\sigma. \tag{2-30}$$

Subindex σ indicates the population opposed to the state where the energy is corrected. We assume that the mass is the same in any case. The mean-field shift correction is relevant to this work because it will be applied when generating a species from an existing one.

2.4 The Feshbach resonances

As we have seen in the development of this chapter, fermions trapped in the ultra-low temperature regime will behave differently depending on the intensity and sign of their interaction.

One of the appealing features of lithium is its broad ability to modify the interactions through a magnetic field. This phenomenon is known as Feshbach resonance, also *Fano-Feshbach resonance* [2]. Feshbach described this phenomenon from the point of view of nuclear physics [81, 82]. On the other hand, Fano simultaneously described this behavior from the atomic physics perspective [83].

A good first approach to understanding Feshbach resonances is to take the results from the scattering problem for a spherical well potential. It is important to mention that Feshbach's resonances are not equivalent to potential resonances, but this analogy allows us to understand the essence of this phenomenon [84].

We remark on one of the fundamental results using this approach, and we refer to the relation between binding energy and the scattering length near the resonance in the positive case, that is

$$E_b = -\frac{\hbar^2}{m a_s^2}. \tag{2-31}$$

This result is essential to the experimental formation of pairs because it is more convenient to form a pair in the region where a_s diverges on the Unitary regime, and the binding energy is too small, i.e., no greater cost to form pairs.

We need to consider that the atom has a more complex structure, and in the presence of magnetic fields, this plays a relevant role in the interactions. More specifically, the two internal structures of atoms, electronic and nuclear spin, form a potential hyperfine structure with the following form

$$V_{\mathrm{hf}} = A\left(\mathbf{s}_1 \cdot \mathbf{i}_1 + \mathbf{s}_2 \cdot \mathbf{i}_2\right), \tag{2-32}$$

where the constant A is analogous to the case of the hyperfine structure of only one atom. The total spins are obtained by the sum of angular momentum formalism $\mathbf{S} = \mathbf{s}_1 + \mathbf{s}_2$ and $\mathbf{I} = \mathbf{i_1} + \mathbf{i_2}$, electronic and nuclear respectively.

The total electronic spin $\mathbf{S}$ results are not convenient for the interaction given by V_{hf}. As a consequence, we rewrite (2-32) as the sum of two potentials, where one of these contains the singlet and triplet split [85]:

$$V_{\mathrm{hf}} = \frac{A}{2}\mathbf{S}\cdot\mathbf{I} + \frac{A}{2}\left(\mathbf{s}_1 - \mathbf{s}_2\right)\cdot\left(\mathbf{i}_1 - \mathbf{i}_2\right) = V_{\mathrm{hf}}^{+} + V_{\mathrm{hf}}^{-}. \tag{2-33}$$

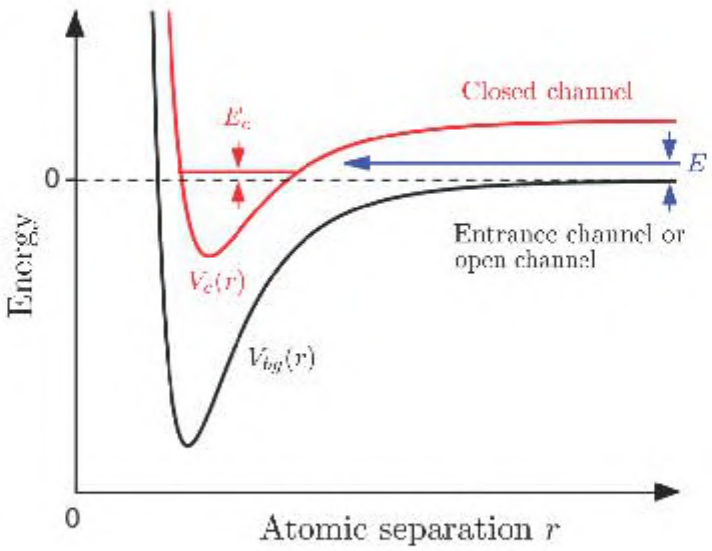

Figure 2-3: Two channel diagram of an atom-atom collision with energy E. The Feshbach resonance occurs when $E \approx E_c$. Image taken from [2] and edited.

In an explicit term V_{hf}^{-}, we have the coupling of the triplet (symmetric electron states) with the singlet (antisymmetric electron state). Note that, its dependence on $\mathbf{s}_1 - \mathbf{s}_2$, it means the relative spin orientation [1]. If there were no coupling between the singlet V_c and the triplet potential V_{bg}, the atoms would scatter off each other in $V_{bg}(\mathbf{r})$, changing their phase shift.

We can use Fig. 2-3 to sketch the behavior of the interaction. The singlet potential constitutes a *closed channel* (red potential in Fig. 2-4), meaning its continuum states are energetically inaccessible as scattering final states due to energy conservation constraints [1,86]. A Feshbach resonance emerges when the incoming scattering state, the *open channel* (black potential in Fig. 2-4), becomes resonant with a bound state in this closed-channel singlet potential. The energy of the colliding atoms E aligns with the energy of the closed-channel bound state.

In the absence of inelastic collision channels, the $s-$wave scattering length can be tuned by the magnetic field near the Feshbach resonance, followed by the equation [85]

$$a_s(B) = a_{bg}\left(1 - \frac{\Delta B}{B - B_0}\right), \tag{2-34}$$

where a_{bg} corresponds to the existing background; ΔB is the magnetic resonance width, and B_0 is the magnetic value of the center of resonance or the divergence of scattering length. We omit the derivation of this model; then, we require Scattering Theory in its most formal form [84].

2.5 Tunability of the interactions

As mentioned, we can tune the interaction between atoms by using a constant magnetic field over the sample. This configuration was described in Chapter 1 and consists of two coils in a Helmholtz configuration [87], providing a resolution close to 0.02 mT in the region of the ultracold cloud. Its manipulation is through an analog signal that allows the current values to be ramped.

Remembering that the initially atomic sample consists of the two hyperfine states of the $2^2S_{1/2}$ state for $F = 1/2$ and $F = 3/2$ allows us to form two other types of pairs. We will use the compact version to denote the accessible low-seekers hyperfine states:

$$|F = 1/2, m_F = +1/2\rangle \equiv |1\rangle\,, \tag{2-35}$$

$$|F = 1/2, m_F = -1/2\rangle \equiv |2\rangle\,, \tag{2-36}$$

$$|F = 3/2, m_F = -3/2\rangle \equiv |3\rangle\,. \tag{2-37}$$

We establish the other notation based on RGB colors (red-green-blue), see Fig. 2-4. This color convention will become relevant later in identifying the pairs graphically.

Figure 2-4: Convention for the three lowest hyperfine states of ^{6}Li used throughout this work, identified with an RGB color code: $|1\rangle$ (Blue), $|2\rangle$ (Green) and $|3\rangle$ (Red).

After the molasses process, exposed to the section of the experimental setup in Chapter 1, we arrive at the last cooling stage with the atoms in the $|1\rangle$ and $|2\rangle$ states in a $52(1) : 48(1)$ proportion, close to having a balanced sample. These atoms present a Feshbach resonance around the 83.2 mT with a width of $\Delta B \approx 30$ mT [52].

We define the interaction strength between two fermions, g_{ij}, as follows

$$g_{ij} = \frac{4\pi\hbar^2}{\mathrm{m}} a_{s_{ij}}\,, \tag{2-38}$$

where m corresponds to the mass, our advantage is that, in every case, the mass is the same. We specified the scattering length with the subindex $ij = \{12, 23, 13\}$.

Fig. 2-5 shows the Feshbach resonance for the $|1\rangle - |2\rangle$ mixture. This figure use the reported data in [3]. The positive region of g_{12} (between 55 and 75 mT) corresponds to the BEC region (light purple zone), and the pair formed are diatomic molecules of size of the order of $a_{s_{12}}$. The negative values for g_{12} (between 85 and 100 mT) corresponds to the BCS region (light orange zone). The pair formed is the Cooper pair, and its characteristic size in the position space is much greater than the sample because the binding is formed in the momentum space. Finally, the divergence region of g_{12} (near 83 mT) corresponds to the

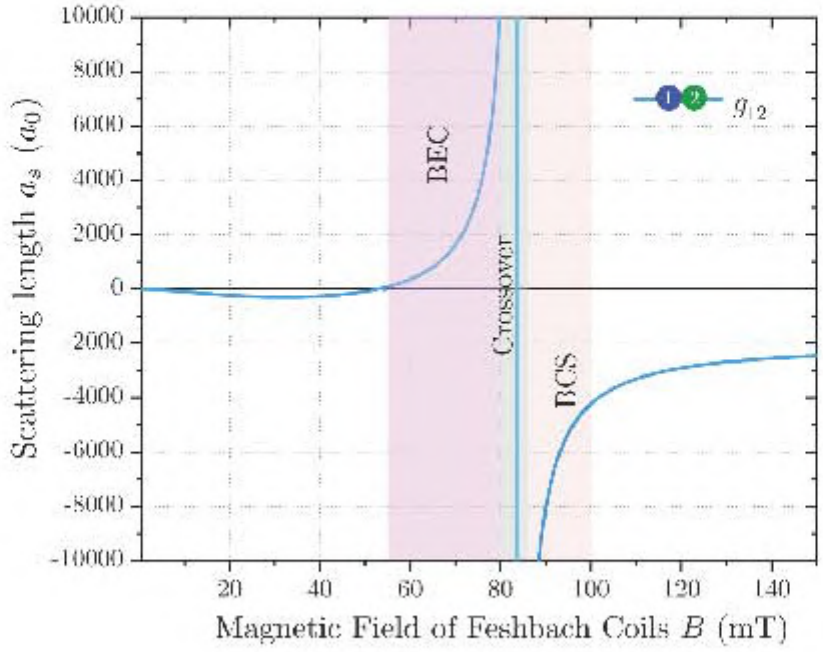

Figure 2-5: Feshbach resonance for the two lowest hyperfine states of ^{6}Li. The resonance has a width of ~ 30 mT, with the scattering length diverging at 83.2 mT. The data plotted was obtained from [3].

Unitary region (light green zone) where the pair formation is a superposition between the two other regions.

A correction for the Lithium case to fit the Feshbach resonances is proposed in [88]. The addition is a factor (α) that increases when the magnetic field is far from the resonance B_0

$$a_s(B) = a_{bg}\left(1 - \frac{\Delta B}{B - B_0}\right)(1 + \alpha(B - B_0))\,. \tag{2-39}$$

The curve shown in Fig. 2-5 results from complex numerical computations; in this form, the equation presented before is a rough approximation.

2.5.1 Three hyperfine states of ^{6}Li

Introducing the third state, in the conditions of pair collisions, we have three accessible Feshbach resonances, which are depicted in Fig. 2-6. The summary of the principal quantities are collected in Table 2-1, which is considered the most recently measurements in the ^{6}Li case [3].

We note the proximity between the three possible Feshbach resonances. This implies that the same experimental configuration can be employed to investigate the remaining two pairs that are not utilized. This particular condition motivates our interest of have access to the third species.

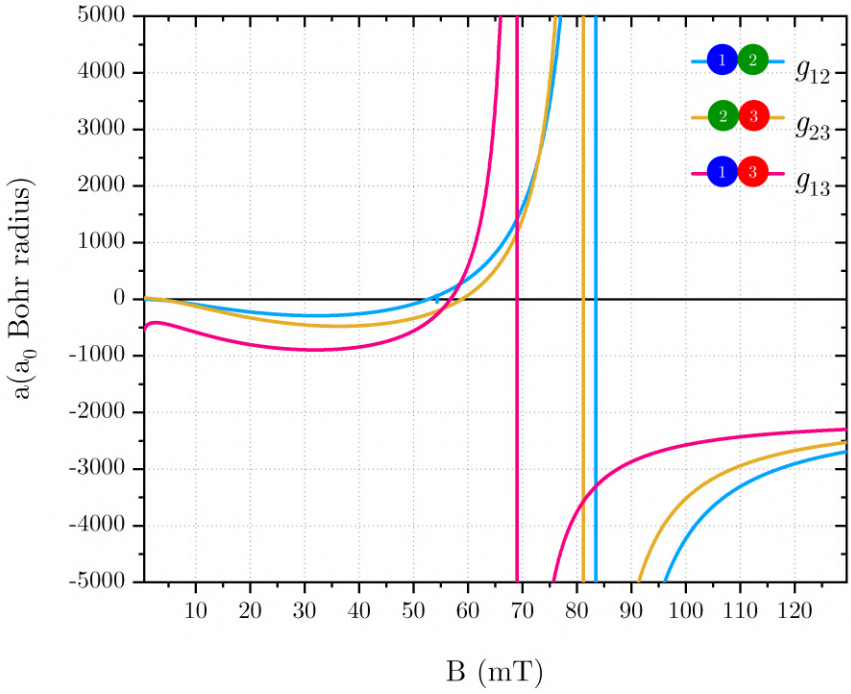

Figure 2-6: Feshbach resonances for the three possible pairings of the lowest hyperfine states of ^{6}Li. Main parameters are summarized in Table 2-1.

Paired states	a_{bg} (a_0)	B_0 (mT)	ΔB (mT)	α (mT^{-1})	**Reference**
$\|1\rangle - \|2\rangle$	-1582(1)	83.218(8)	26.23(3)	0.004	
$\|2\rangle - \|3\rangle$	-1642(5)	80.976(5)	20.02(5)	0.002	[3, 52, 88]
$\|1\rangle - \|3\rangle$	-1770(5)	68.968(8)	16.66(3)	0.003 95	

Table 2-1: Properties of the Feshbach resonances for the three pairing combinations of the lowest hyperfine states of ^{6}Li. a_{bg} is the background scattering length (in Bohr radii, a_0); B_0 is the resonance position; ΔB is the resonance width; and α linear correction parameter (in mT^{-1}).

Chapter 3

RF Transitions

In the context of ultracold gases, various techniques are used to study the properties of these rich systems. For this work, RF spectroscopy is central in generating the third state and performing various measurements and adjustments on our laboratory sample.

The first applications of RF spectroscopy in ultracold atoms emerged simultaneously with the development of techniques for manipulating ultracold matter [89]. Several examples highlight the power and versatility of this technique: measuring the pairing gap in a strongly interacting Fermi superfluid [90, 91], determining thermodynamic and geometric quantities [92–94], and preparing spinor Bose-Einstein condensates (BECs) through evaporative cooling processes [95, 96].

Following Törmä [97], we could consider RF spectroscopy a two-level system, where the ultracold gas has a suitable transition between two internal states. To have consistency with our notation, we represent these two states as $|i\rangle$ and $|j\rangle$ (for $i, j = 1, 2, 3$). A fundamental characteristic of RF lithium spectroscopy is that the wavelength of the applied RF field significantly exceeds all other characteristic length scales within the system, typically surpassing the size of the experimental setup. Consequently, the associated momentum of the RF field is negligible compared to other relevant momentum scales, such as the Fermi momentum. In the development of this Chapter, we will review each of the characteristics mentioned above.

Then we will study the response of the atomic sample to the presence of the Feshbach magnetic field, particularly the Zeeman effect on energy splitting. Then, we will mention the possibility of performing RF spectroscopy to occupy the third state and how to implement it, which will be through an antenna based on the one built by the Roati group [21] and adapted to our experimental setup. In the last part, we will detail the construction and characterization of this electronic device.

3.1 ^{6}Li under the B-Feshbach field

In Chapter 1 we explored the influence of magnetic fields on the electronic structure of an atom. Then, we discussed in Chapter 2 the Feshbach resonances as a particularly useful

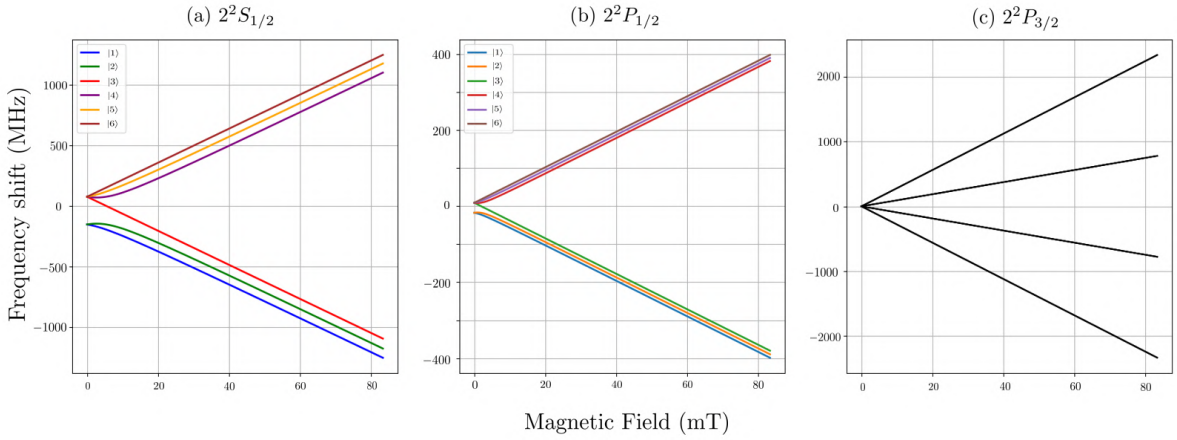

Figure 3-1: Zeeman splitting of the (a) ground state (a) $2^2S_{1/2}$ and the first excited state (b) $2^2P_{1/2}$ and (c) $2^2P_{3/2}$ of ^{6}Li, calculated for the range of magnetic fields accessible in the experiment.

property of ^{6}Li. In this case, it involves a constant magnetic field in the region of the sample. As a consequence of the presence of the magnetic field, the energy levels will suffer a shift, which can be studied through the Zeeman effect in the hyperfine structure.

The range of the magnetic field with optical access for imaging, i.e., the possibility of taking an image by absorption method, is given by the frequency shift produced by the Zeeman effect. The accessible range is from 50.00 mT to 100.00 mT, which means we use the Breit-Rabi formula (1-16). We need to consider some constant values to obtain the behavior described by the eq. (1-16). In the case of the Landé coefficients for the electron and nucleus for Lithium, we have $g_J = 2.002\ 301\ 4(7)$ and $g_I = -0.000\ 447\ 654\ 0(3)$, respectively [37].

Following these ideas, we show the Fig. 3-1 with the Zeeman effect for the states (a) $2^2S_{1/2}$, (b) $2^2P_{1/2}$ and (c) $2^2P_{3/2}$. This last state cannot be solved with the Breit-Rabi formula, so it is solved numerically diagonalizing the complete Hamiltonian.

Using the values of properties for the ground state of ^{6}Li, we can obtain the difference of the two lowest hyperfine levels, $\Delta E_{\text{hf}} = 228.205\ 259(3)$ MHz [37, 38]. This value is relevant for the computation of the frequency for imaging. Another consideration is the energy change for the state $2^2P_{3/2}$; this is the level we use to excite the ground state for the image process.

We focus on three specific magnetic regions, as previously shown in Fig. 3-2. The first region corresponds to the non-interacting $|1\rangle - |2\rangle$ at 52.7 mT; the second at 69.0 mT, and the last at 73.0 mT. In all three cases, the transitions between $|1\rangle$ and $|2\rangle$, as well as between $|2\rangle$ and $|3\rangle$, occur at frequencies on the order of ~ 80 MHz in the RF range.

3.2 Magnetic-dipole transitions

As mentioned above, the RF wavelength is significantly larger than the ultracold cloud. Specifically, the wavelength of an 80 MHz RF wave is approximately 3.75 m in free space. In

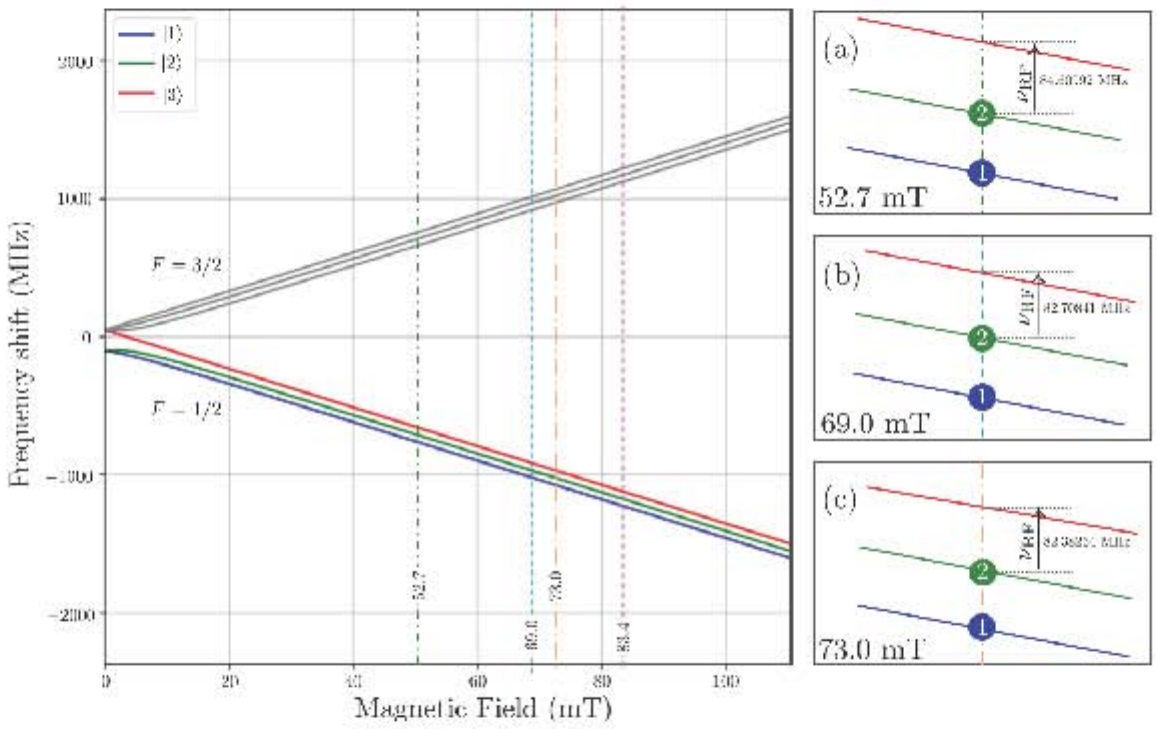

Figure 3-2: Left: Zeeman shift of the ground state hyperfine levels of ^{6}Li.(Breit-Rabi solution). Dashed vertical lines mark four magnetic fields of interest. Right: Schematic representation of the interaction regimes at these fields: (a) Zero-crossing for the pairs at 52.7 mT. (b) BEC regime for the $|1\rangle - |2\rangle$ and $|2\rangle - |3\rangle$ pairs at the $|1\rangle - |3\rangle$ resonance in 69.0 mT. (c) Region where $a_{s_{12}} = a_{s_{23}}$ at 73.0 mT. The RF transition frequency for $|2\rangle \longrightarrow |3\rangle$ is indicated.

comparison, the size of the atomic sample is typically three orders of magnitude smaller, on the order of 10^{-4} m or less. This large disparity of scales allows us to assume that, at the position of the atomic sample, the effective RF field is spatially uniform. This assumption is analogous to the dipolar approximation, where the spatial variation of the field over the size of the atomic system is negligible.

In this scenario, the magnetic dipole transition mediates the interaction between the RF field and the atoms. The Hamiltonian that can describe this interaction is:

$$\hat{\mathcal{H}}_{\mathrm{RF}} = -\boldsymbol{\mu} \cdot \mathbf{B}\,(t)\,, \tag{3-1}$$

where $\boldsymbol{\mu}$ is the magnetic dipole atomic vector given by eq. (1-15). Consider that the RF field is polarized in the region of the atomic sample, i.e., $\mathbf{B}\,(t) = B_{\mathrm{RF}} \cos(\omega t + \delta)\mathbf{e}_\epsilon$, with $\mathbf{e}_\epsilon$ the polarization unitary vector. Then, the interaction (3-1) will take the following form

$$\hat{\mathcal{H}}_{\mathrm{RF}} = -\frac{1}{\hbar} B_{\mathrm{RF}} \cos(\omega t + \delta) \left(\mu_B g_J \hat{\mathbf{J}} - \mu_N g_I \hat{\mathbf{I}}\right) \cdot \mathbf{e}_\epsilon, \tag{3-2}$$

where ω is the RF angular frequency, and δ is a general phase. In the experiment, δ is chosen by a function generator, but for simplicity, we choose it in the sequence to be zero.

At the end of the experiment sequence explained in Chapter 1, we turn a magnetic field on, and the quantum samples are generated in the presence of this field. Therefore, a constant offset defines the quantization axis as aligned with the vertical (gravity direction) axis. For convenience, we label this axis as z.

In this form, we must ensure that the component of the RF field orthogonal to the Feshbach magnetic field is non-zero and maximizes the transitions more effectively. For this reason, working with a polarization $\mathbf{e}_\epsilon \perp \mathbf{e}_z$, the only permissible transitions are the $\sigma^{\pm}$ [41]. Then, we need to verify that the desired transitions are of this type.

Using the representation of the coupled basis $|F, m_F\rangle$ into the uncoupled $|m_J, m_I\rangle$, we obtain that

$$\begin{aligned} |1\rangle &= \alpha\,|-1/2, 1\rangle - \beta\,|1/2, 0\rangle \\ |2\rangle &= \beta\,|-1/2, 0\rangle - \alpha\,|1/2, -1\rangle \\ |3\rangle &= |-1/2, -1\rangle \end{aligned} \tag{3-3}$$

where $\alpha = \sqrt{1/3}$ and $\beta = \sqrt{2/3}$ are the Clebsh-Gordan coefficients. With this information, we can verify that the two transitions $|1\rangle \longrightarrow |2\rangle$ and $|2\rangle \longrightarrow |3\rangle$ are possible only with the polarization $\mathbf{e}_-$ and satisfy the selection rules $\Delta F = 0$, $m_F = 1$ and $\Delta F = 1$, $m_F = -1$, respectively.

In this type of matter-field interactions, the Rabi frequency characterizes the population exchange between the two states [31, 41] and has the following form

$$\Omega_R = \frac{\mu B_{\mathrm{RF}}}{2\hbar}. \tag{3-4}$$

Therefore, the main task for this experimental project is to construct the appropriate electronic element to generate a field with these characteristics. This device has an antenna that aims to optimize the emission amplitude in the component orthogonal to the Feshbach field.

3.3 Generating the RF-field

As already mentioned, the design, construction, and characterization of an antenna that can emit frequencies around 80 MHz will be our target for the rest of this Chapter. The antenna, in principle, is an electronic device that uses the surrounding medium as a propagation medium. The most relevant properties of antennas are the radiation pattern, polarization, gain, and impedance [98]. For our purposes, we adapt the characterization and geometry using information from groups such as Roati [99], Jochim [100], and Grimm [101], who use similar RF antennas for the same purposes.

3.3.1 Design of the antenna RF

We know now the specific values of the RF transitions between $|1\rangle$, $|2\rangle$, and $|3\rangle$, which are of the order of 80 MHz, and result as a possible value to obtain through an RF signal produced by an antenna. We must consider some elements and characteristics that we explore in this section.

The efficient radiation of an antenna depends on the size of the radiative element [102,103]. For our case, taking as a reference, the antenna length must be approximately 3.75 m, which corresponds to the wavelength in a vacuum. This length in a medium as a coaxial cable is the order of 2 m. For the dimensions of the fermionic lithium experiment, it is impossible to put an antenna of this size, and it never works efficiently. For this reason, the size of our antenna is far from an efficient radiation of RF. We must compensate for these restrictions with high power.

In this form, we design an amplifier circuit for an RF signal, whose scheme is presented in Fig. 3-3. In the sketch, we show the antenna and its connections. This circuit is a peripheral device, integrated into the control system described in the Chapter 1.

The wave generator used to obtain the pulses of the desired frequency is the KEYSIGHT® wave generator 33600A, controlled by an external trigger digital signal[1]. To send a selected frequency, we define the waveform as sinusoidal. The amplitude of the signal cannot be higher than 20 dBm, and for the limitations and efficiency of the amplifier, we operate under 10 dBm. The trigger is selected as external[2]. We must be careful not to have a delay; otherwise, in the trigger menu, it can be omitted.

This signal output comes from channel 1 in the wave generator and is sent to an ultrafast response attenuator of Mini-circuits®. This attenuator is a switch triggered[3] to turn off the

[1] Channel 8C of the control console
[2] back of the device
[3] channel 4C

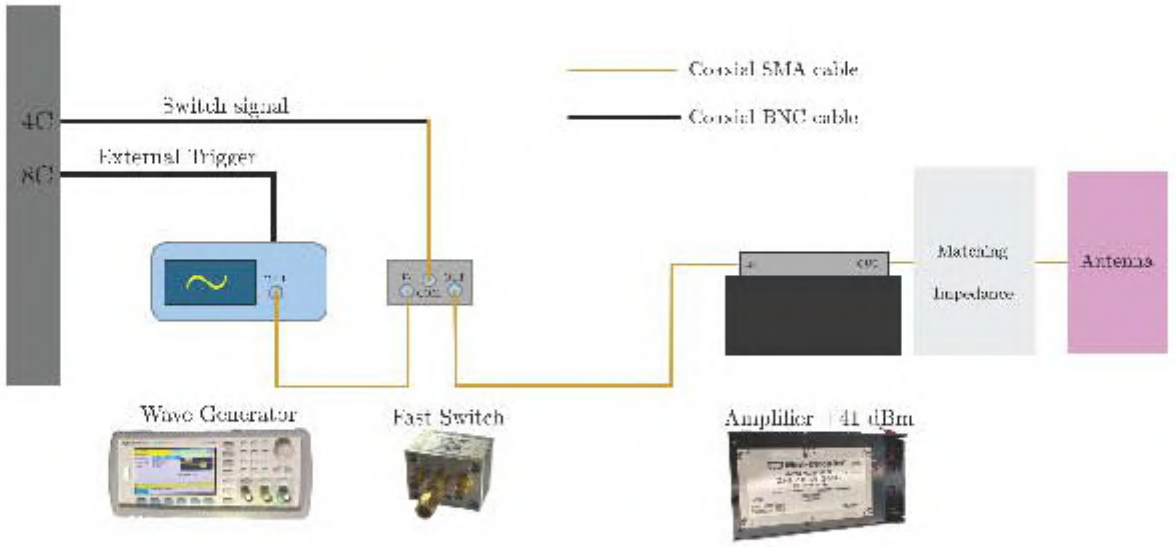

Figure 3-3: Sketch of the diagram generating and amplifying the RF signal. The Wave generator is controlled by an external trigger (8C), which crosses the switch controlled by the control system (4C) and arrives at the amplifier.

signal more efficiently. The output signal continues arriving at an amplifier through an SMA cable.

We use the Mini-circuits® Amplifier ZHL-100W-GAN+, powered by a power source, Delta Electronics®, with 30 V at 8 A. When introducing a signal under 7 dBm, the output signal amplifies +41 dB. In the range between 7 dBm and under 20 dBm[4], the output signal is lower than +41 dB. This characterization was measured using an attenuator of +40 dB and seeing the upper signal in the ZVL Network Analyzer (Rohde & Schwarz®).

Finally, the RF signal travels through an SMA cable from the output of the amplifier to the antenna near the atoms. The terminals were connected to a PCB board so the SMA cables could be connected.

3.3.2 Antenna

The antenna must be placed as close to the atomic sample as possible because the magnetic dipole decays as the cube of the distance [102, 104, 105]. This condition requires us to place the antenna at the window of the vertical axis, the closest to the sample. This restriction has another tiny detail: The window of the vertical axis is for the optical access to the MOT and the imaging beam. Furthermore, this vertical access consists of a cylinder that contains the MOT coils refrigerator system. Then, the antenna must be adequate for these conditions.

An antenna loop is the most convenient option. However, a ring loop is not the solution because the required magnetic field must be orthogonal to the Feshbach field and oriented toward gravity. The best candidate for our antenna is a loop with bean form [21].

[4]This is the maximal value that can be used in the input; we recommend operating under 18 dBm.

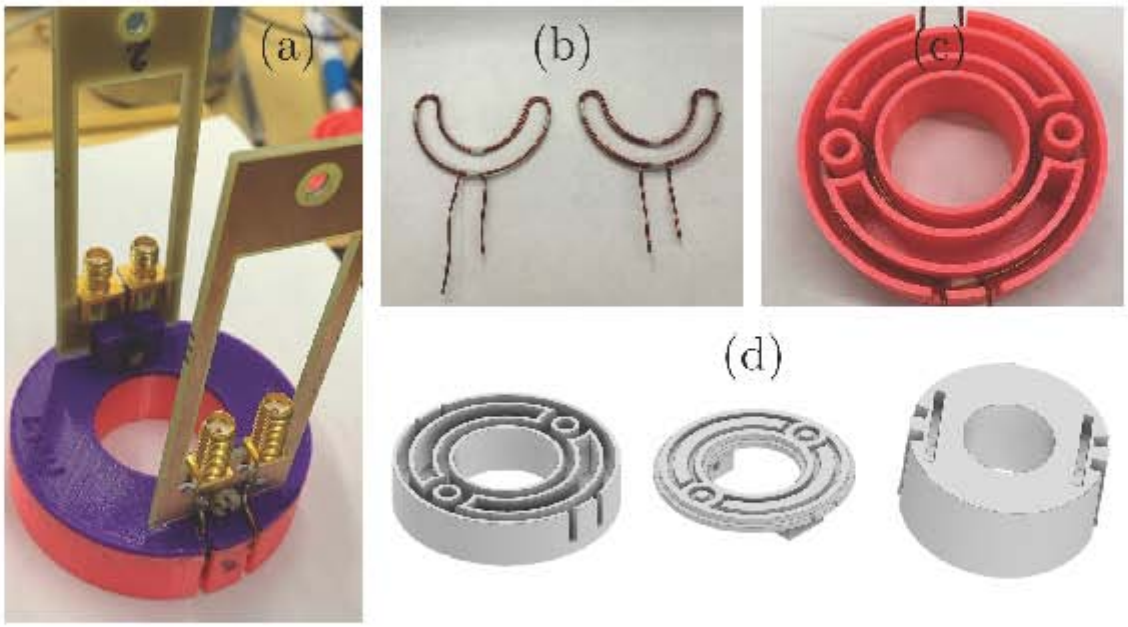

Figure 3-4: Design and assembly of the RF antennas. (a) Final antenna structure with soldered PCB boards and antenna wires. (b) Bent copper wires forming two-loop (left) and three-loop (right) designs. (c) 3D-printed mount for the antennas. (d) 3D model (Autodesk INVENTOR) of the complete assembly, showing the support, cover, and height-adjustment accessory.

Fig. 3-4 presents the final antenna form and the sketch made in the (e) 3D modeling software INVENTOR® and (c) then printed with a 3D printer PRUSA® . (b) The copper wires were bent using a lathe. Each loop has a length of 37.70(5) cm, comparable to the $\lambda/10$ in the vacuum. We are in the range of a short antenna for this case. This particular characteristic gives us a high inductive reactance, and its behavior is that of a magnetic dipole.

3.4 Characterization of the antenna

To optimize the orthogonal projection field of the antenna, we need to ensure a maximal signal radiated. The first option is to use a *balun*(balanced-unbalanced lines transformer), an impedance transformer designed to couple a balanced transmission circuit and an unbalanced transmission circuit [98]. Instead of having the antenna referenced to the ground, the balun creates a signal with a half-period phase shift, which improves the emission by balancing it. We can generate the phase shift using a cable of the appropriate length to achieve the required imbalance, a half-wave balun ($\lambda/2$ balun).

Figure 3-5 shows the connection circuit diagram. Here, the cable labeled $\lambda/2$ corresponds to the measured lengths once the phase velocity of the RF wave in the coaxial cable is known. This extension of the antenna provides the effect of a balun. The second factor that optimizes the antenna radiation is the impedance matching of the circuit to 50Ω, which is achieved

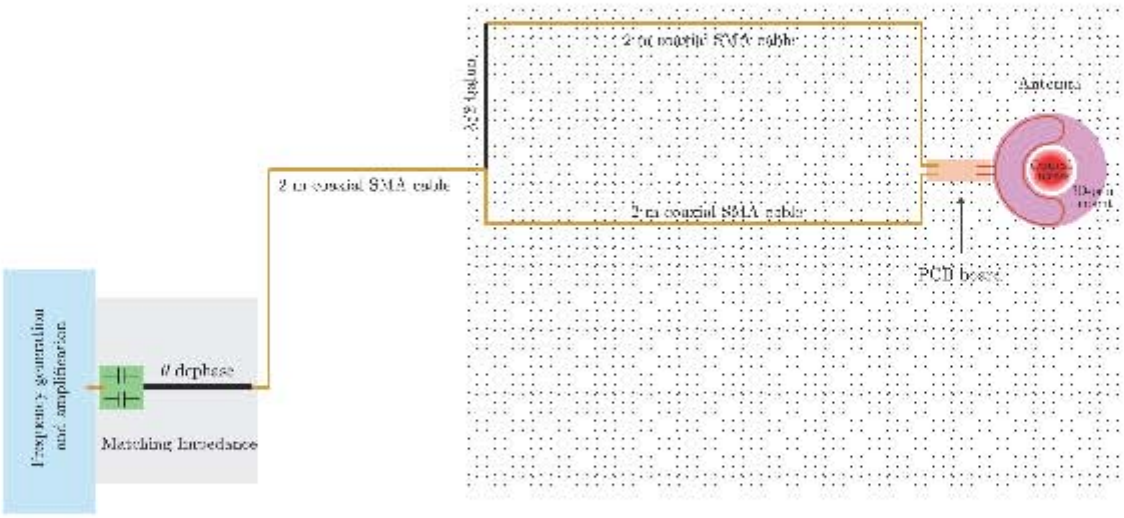

Figure 3-5: Circuit diagram for the RF antenna system. The signal from the amplifier passes through an impedance-matching network (grey box) containing a phase-shifting BNC cable and capacitor circuit. It is then split by a $T-$junction, with one path leading to the antenna and the other to a $\lambda/2$ balun for impedance matching.

using a circuit with variable capacitors.

3.4.1 Phase velocity of an RF wave

The current feeding of the antenna is transmitted through an SMA coaxial cable, so it is important to know the propagation velocity of the RF wave in this material, i.e., the *phase velocity*:

$$v_p(\nu) = \frac{c}{\sqrt{\epsilon}}, \tag{3-5}$$

where ν corresponds to the frequency and ϵ the dielectric constant of the material. Then, we measure the proportion in terms of a free propagation c, and the procedure is detailed below.

The RF signal generated by the KEYSIGHT was sent through a 2-meter BNC cable to an oscilloscope with a bandwidth of up to 2 GHz. The signal was fed into one oscilloscope channel, where a signal T-splitter was connected. The SMA cable under test, which was assembled for us in the LMU, was then attached to the T-splitter, and its output was sent to another channel of the same oscilloscope.

It is important to remark that the signal was not completely split because the oscilloscope's input impedance is 1 MΩ, while the SMA cable has a characteristic impedance of 50 Ω. The phase difference between the two received signals was measured and is shown in Fig. 3-6. To verify the results, another cable was tested with a length of 2 meters. The SMA cable used for the measurement had a 1.010(5) meters length and produced a phase shift of π radians.

In our case, it was calculated for the characteristic frequency at the transition between states $|2\rangle$ and $|3\rangle$ for a Feshbach field of 73.0 mT, 82.406 9 MHz. We can determine our material's phase velocity scaling factor. Since the phase shift corresponds to half a period,

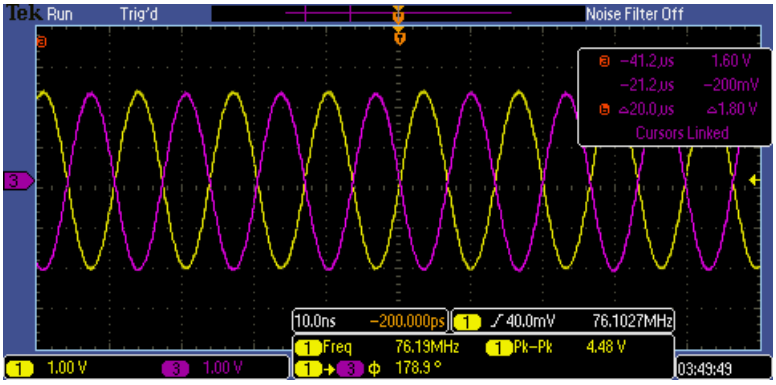

Figure 3-6: Oscilloscope screenshot showing the test of a dephased wave propagating through a coaxial BNC cable.

we multiply the frequency $\nu_{23}(73\ \text{mT}) = 82.406\ 9$ MHz by the length of the whole period 2×1.010 m and divide by the speed of light in free space c. This calculation yields a scaling factor of 55.53(5)%.

We discarded the possibility of a 3π phase shift because, under this assumption, the scaling factor would be around 30%, which is inconsistent with the material's properties and would result in inefficient signal propagation.

Substituting the frequency with the $|1\rangle - |2\rangle$ transition $\nu_{12}(73\ \text{mT}) = 76.102\ 5$ MHz, we find that the required cable length for a half-wavelength balun is 1.094 meters for this case.

We have reviewed the balance of the transmission line. However, it is also crucial to ensure that the impedance of the circuit is matched to 50 Ω with zero imaginary part (purely resistive); these parameters are the optimal efficiencies of any antenna. This adjustment is important to minimize power reflection in the circuit, which can degrade signal integrity or damage the RF amplifier [106].

To demonstrate the significance of impedance matching, we performed measurements in an *ex-situ* configuration, maintaining the approximately same distances between the antenna and the atomic sample. The magnetic field component of interest was measured using the TekBox EMC Probe Set test antennas. The results of these measurements are shown in the adjacent Fig. 3-7, highlighting the impact of proper impedance matching on the maximum efficiency of the system and the reduction of reflections.

The signal received by the test antenna is amplified using a ZFL-500LN+ amplifier (Mini-Circuits), which has a response of +28 dB for the frequencies corresponding to the transitions we are working with. The amplitude and waveform of the signal were verified using an oscilloscope with a maximum bandwidth of 2 GHz. The emission frequency was also monitored using the Network Analyzer (Rohde & Schwarz) in spectrum analyzer mode, with a bandwidth of 300 Hz.

Fig. 3-7 shows the effect on the emission in the ex-situ measurements, where for a matching system, the emission is notably more than the non-matching case. The data in the graphic presents a linear response from the circuit of the antenna, but in the case of the non-matched

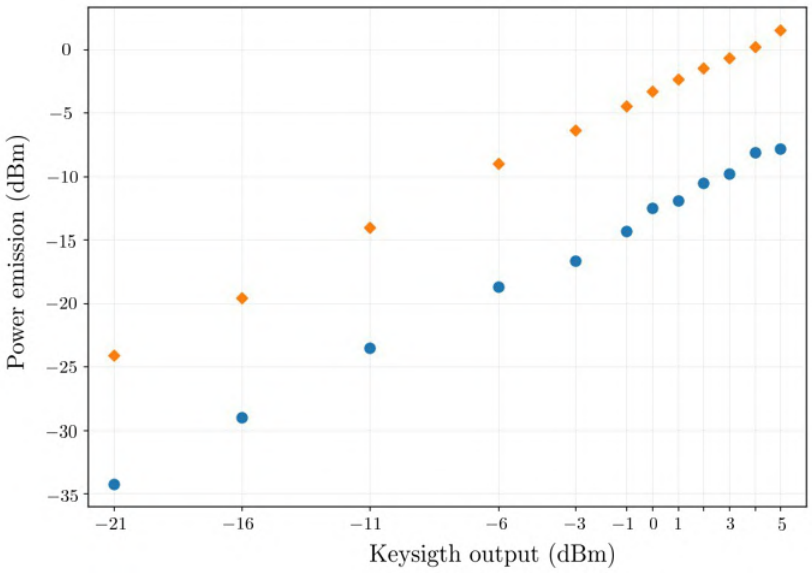

Figure 3-7: Comparison of antenna emission without impedance matching (blue dots) and with impedance matching (orange diamonds). Data were obtained using the antenna probe setup.

antenna (blue dots), presents a saturation in the higher power set emitted by the function generator.

To integrate the half-wave balun, we had to extend the antenna terminals to bring them closer to the position of the amplifier (located under the main optical table). Figure 3-5 shows the resulting circuit design for the antenna.

The circuit's response was examined using the network analyzer by evaluating the scattering matrix's S_{22} parameter for this configuration [102,107]. This component contains the reflection coefficient data.

We extracted the impedance data, including its real and imaginary components. With this information, we determined the circuit modifications needed to minimize the imaginary part and obtain an almost purely resistive impedance 50 Ω.

Reduce the Imaginary Impedance

The imaginary part of the impedance corresponds to the reactance X of the circuit. This value is formed by the inductive part Z_L (positive value) and the capacitive part Z_C (negative value) of the circuit, both given by

$$Z_L = \imath\omega L, \qquad Z_C = -\frac{\imath}{\omega C}. \tag{3-6}$$

The frequency of the alternating current (AC) is ω, the inductive response of the circuit L, and the capacitive response C. Using the network analyzer. If the value of the reactance is negative, we know that we need to integrate an inductor device equivalent to the negative

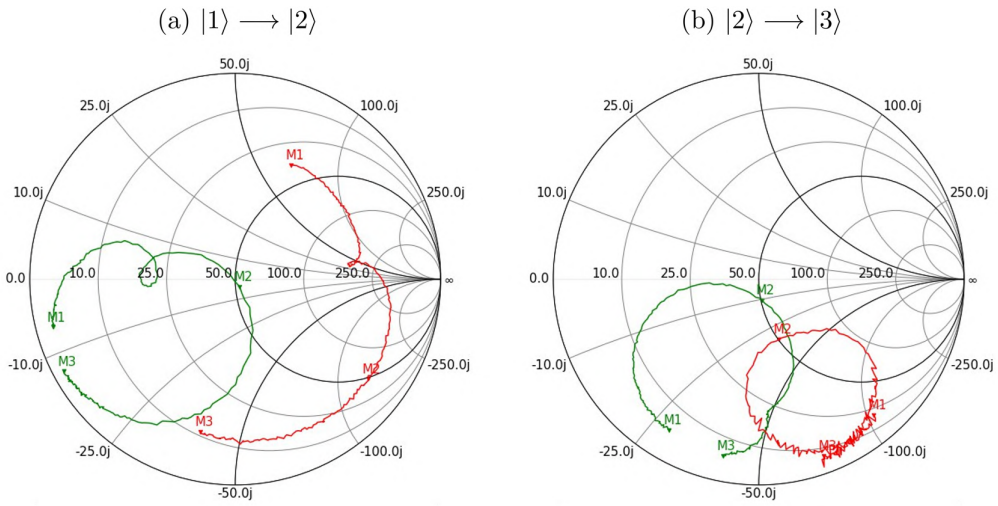

Figure 3-8: Smith charts of the S_{22} parameter for the antenna circuits. In both maps, the red trace shows the original impedance values from 70 (M1) to 90 MHz (M3), while the green trace represents the matched impedance at 50 Ω. The marker M2 is set at (a) 76.11 MHz and (b) 82.43 MHz.

value. In the other case, we need a capacitor element to set the imaginary part to zero.

In our case, the value was negative and around to $100 - 200$ Ω. The solution contemplates the elaboration of a dephase BNC cable. This cable helps us to set the imaginary part in the region values of ± 100 mΩ. The cable length corresponds to the dephase angle for the frequency of interest to rotate the curve on the Smith Chart. Also known as the Reflection-coefficient chart, it is a conform mapping of the passive impedances [98].

Set the Real Impedance

To obtain a signal with a 50 Ω in the real part of the impedance (resistance),

$$Z_R = R. \tag{3-7}$$

We use a circuit of variable capacitors (GZC12100, Sprague-Goodman) ranging from 9 to 120 pF. By adjusting the capacitance, we obtain the value of 50 Ω. This procedure was realized in both antenna circuits. The differences are shown in Fig. 3-8, where the two curves represent the signal obtained by the Network analyzer and mapping into a Smith chart in a 20 MHz range centered in the mean frequency for each transition.

3.5 Antenna Mounting

After integrating the antenna into the experimental setup, we observed the radiation's true effects in the ultracold lithium cloud. This test provided valuable information on the radiated power since the signal was detectable in all electronic devices. We took advantage of this

observation and placed a test antenna over the analog and digital terminal consoles. We could verify the emission's realization by monitoring the RF pulse on an oscilloscope.

Fig. 3-9 presents the final version of the antenna. This figure consists of four images: (a) shows a 3D scheme of the position of the antennas in the science chamber system; we used the post holder PH6E of Thorlabs to reach the necessary height to be close to the lower vertical window of the science chamber. The upper window was not a possibility due to the presence of the microscope objective for the high-resolution imaging system. Chart (b) shows a photograph of the antenna assembly before being inserted into the optical access cylinder.

The antenna was placed as carefully as possible, neither disrupting optical access nor misaligning in the vertically propagating beams system. Fig 3-9(c) shows the measures used to avoid those mentioned above; (d) is the final position of the antennas.

Two antennas were inserted into the plastic mold: one designed for the $|1\rangle - |2\rangle$ transition with a two-loop configuration, and the other for the $|2\rangle - |3\rangle$ transition with a three-loop configuration. The number of wire turns was optimized based on preliminary observations to reduce low-efficiency challenges. Furthermore, impedance matching analysis confirmed that the two-loop antenna performed best at 76 MHz, while the three-loop configuration had optimal response at 82 MHz.

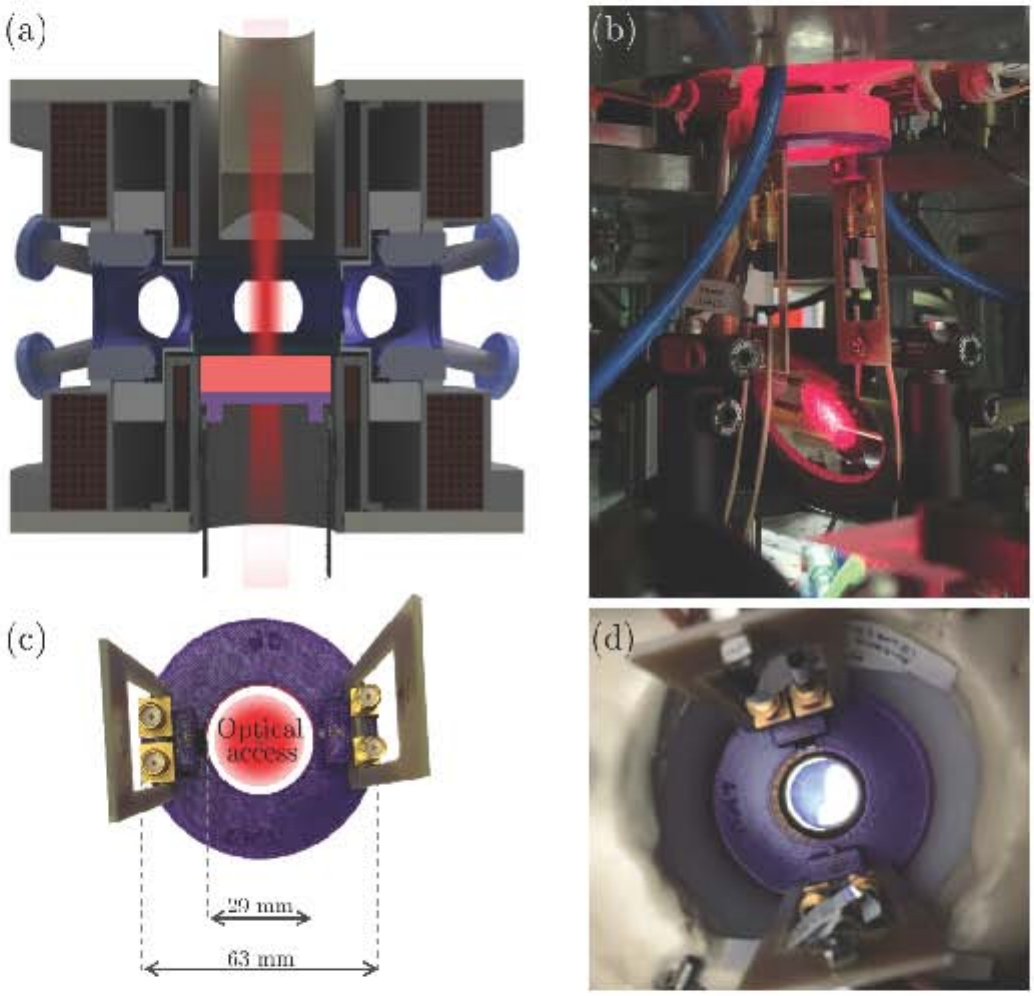

Figure 3-9: Final antenna installation. (a) 3D schematic of the antenna position relative to the science chamber. (b) Photograph of the antenna assembly before insertion into the vertical access port. (c) Key dimensional constraints of the mount to avoid obstructing optical beams. (d) Final installed position of the antennas.

Chapter 4

Measurements with RF emissions

At this point, we are ready to observe the first results of the use of the RF signal to access the third state $|3\rangle$, but also to adjust the antenna prepared for the transition to excite the $|1\rangle$ to $|2\rangle$ state. In this sense, this Chapter compiles the main results of the first tests of the antennas installed in the LMU experimental system, and we will highlight many of the operational considerations.

Observing the initially unpopulated state is the most basic indication of antenna performance. For this purpose, we will present the protocol for observing the population of interest. Finally, we will show the Rabi oscillation observed with both antennas.

The magnetic field of choice for this investigation was 73 mT. Unlike most third-state transfer experiments implemented (in other groups) around the BCS regime ~ 87 mT [21, 22]. We specifically explored the regime where the $|1\rangle - |2\rangle$ and $|2\rangle - |3\rangle$ interactions share identical scattering lengths (see Fig. 2-6).

4.1 First Considerations

The first step is to ensure accessibility of the state, which means that the imaging light we send must be suitable for exciting the state. Following the idea of the imagining process, we remove it using light in resonance with the excited state, $2^2P_{3/2}$. This frequency of light is controlled via the software control, which in particular operates the imaging AOM[1] centered at 200 MHz or the other at 350 MHz, each with a tuning range of ± 50 MHz. The choice of AOM depends on the total energy shift required to excite the target state (see Appendix A).

In Table 4-1, we present the frequency center value of the absorption imaging process used to observe the required state. This table only shows the case of the two projections of $F = 1/2$ from the ground state. Note that the first test with antennas produced a balanced sample of $|1\rangle$ and $|2\rangle$ states.

[1]The Acusto-Optic Modulator is a device that can control the transmitted power, frequency, and/or spatial direction from a laser beam.

State	**AOM**	**Frequency** (MHz)			
		52.7 mT	69.0 mT	73.0 mT	83.4 mT
$\|1\rangle$	rep	–	200.0	200.0	–
	cool	–	–	–	94.0
	200 MHz	–	–	–	–
	350 MHz	–	307.9	337.25	302.0
$\|2\rangle$	rep	190.0	200.0	190.0	–
	cool	–	–	–	94.0
	200 MHz	223.5	–	–	–
	350 MHz	–	345.2	365.5	369.7

Table 4-1: Center frequency settings (in MHz) for the acousto-optic modulators (AOMs) used to image specific spin states at various magnetic fields. *rep* and *cool* refer to the repumper and cooling laser beams, respectively. A dash (−) indicates the setting was not used for that specific state and field.

4.2 The non-interacting system

As we have mentioned in Chapter 1, we prepare the atomic gas during the evaporative cooling stage at the 83.4 mT field; then, to arrive at the 52.7 mT field, we need to achieve a magnetic sweep crossing to the weakly repulsive interacting region, where the atoms paring as diatomic molecules. For this reason, we have a limitation in obtaining an ideal gas because the formation of pairs is highly probable in the positive scattering lengths.

Our solution for breaking these pairs is the execution of two magnetic sweeps. The first is from 83.4 mT to 50.0 mT, arriving at this last magnetic field value, where the scattering length is negative and "weak", such as the dissolution of any pair formed throughout the positive range. A second sweep is executed from 50.0 mT to arrive at the 52.7 mT where the interactions are null, in the literature known as *zero crossing* (Fig. 4-1). Both sweeps during 100 ms, and the separation between both is similar to the time sweep duration, and a thermalization time of around 90 ms.

It is worth mentioning that on October 18, 2024, we reached for the first time at LMU the realization of an ideal atomic gas. Fig. 4-2 shows the first image of this new accessible regime for the LMU with a good noise signal.

Working with the ideal fermionic gases mixture $|1\rangle - |2\rangle$. In this condition, we apply the following protocol for the antenna $|1\rangle - |2\rangle$ (see a diagram of Fig. 4-3):

1. Make an image of the atoms in both states, verifying the presence of these two states. We concentrate on the state $|2\rangle$, monitoring the presence of the state $|1\rangle$ in intervals.

2. Execute a shot of resonant light for 4 μs to eliminate every atom at the state $|2\rangle$. This action is called *blast* and would be a recurrent technique to prepare the system and

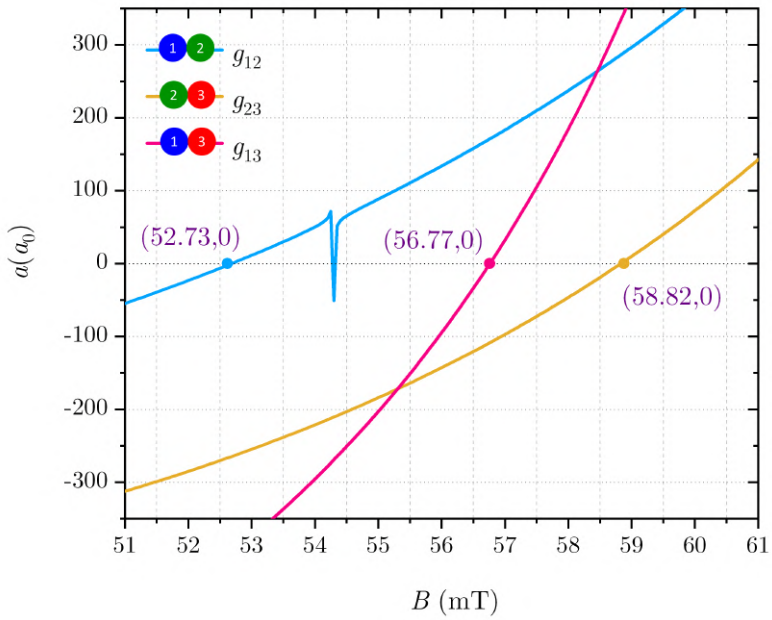

Figure 4-1: Zero crossing for the three types of pairs formed with the lowest hyperfine states of ^{6}Li.

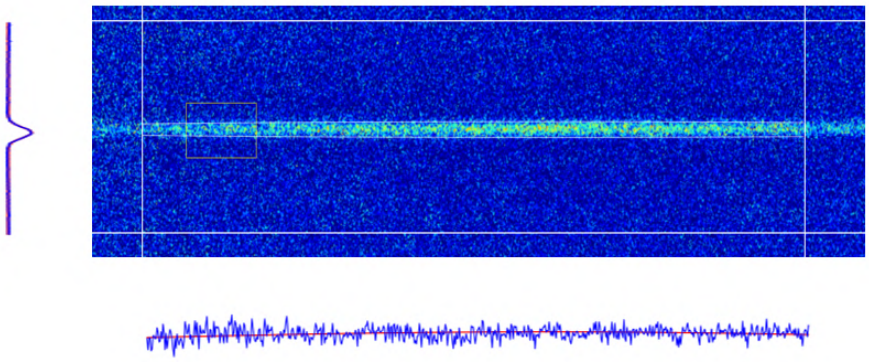

Figure 4-2: First realization of a non-interacting $|1\rangle - |2\rangle$ Fermi gas mixture at LMU. The image was obtained at the final stage with a high-power ODT. The side panels show the integrated density profiles, shown here as references.

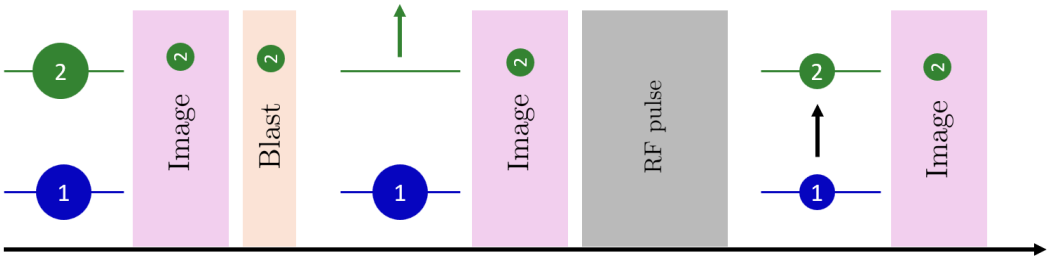

Figure 4-3: Implemented protocol for the realization of the first transference $|1\rangle \longrightarrow |2\rangle$ in the gas ideal condition. See the more detailed procedure in the algorithm described in the text.

Parameter	Symbol	Value
Magnetic Field	B_0	52.3(2) mT
Transfer Frequency	ν_{12}	75.600 9(7) MHz
Shift Frequency†	$\Delta\nu_{12}$	$\sim$ 300 kHz
Pulse Time	t_{RF}	500 ms‡
Power set	P_{K}	-2 dBm

Table 4-2: Parameters used to see the first transference $|1\rangle \longrightarrow |2\rangle$ (see Fig. 4-4). †This shift is to respect of the theoretical value. ‡This extended pulse damages the amplifier; we recommend omitting it to operate at these times. The power set is the KEYSIGHT output.

probe the re-population of the state to evaluate. Then, check the presence of the atoms in $|1\rangle$.

3. Verify the effect of the blast by seeing the image of the state $|2\rangle$. There must not be any atoms.

4. Activate the RF emission. Controlled by the subroutine: *RF-constant.sub*[2] in the control system program. The duration, t_{RF}, of this pulse, is shown in the table 4-2.

5. Make an image of the state $|2\rangle$. To observe the transferred atoms, we perform a sweep of the frequency sending for the KEYSIGHT, moving in the scale of 1kHz in the vicinity of the $\nu_{12}(52.7\ \mathrm{mT}) = 75.32$ MHz.

Fig. 4-4 shows the first transference of atoms in the non-interacting regime. We select this regime to avoid the mean-field shift. We expected to verify the theoretical values, but the signals could not distinguish any population fluctuation in each state. Then, we cannot perform detailed RF spectroscopy in this region, but we have guaranteed the antenna's functionality $|1\rangle - |2\rangle$.

Until this point, the efficiency of the antenna was not optimal. We reaffirm this sentence for the instability number after the transference. The following results were obtained with all the considerations described in Chapter 3.

[2]Consists of the sequence 4C-ON, 8C-ON, 8C-OFF, 4C-OFF, with the separation of the time pulse.

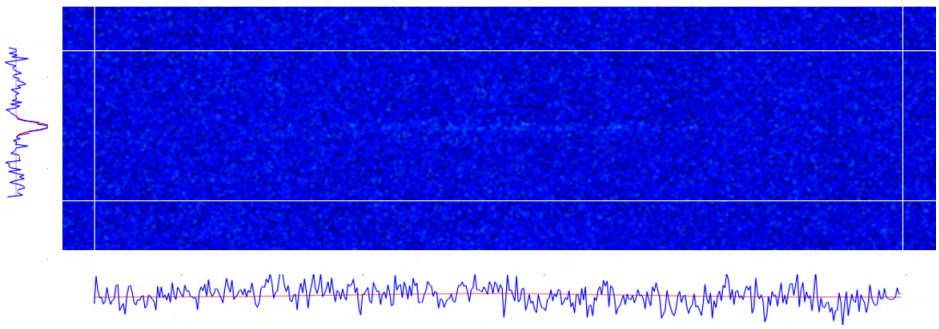

Figure 4-4: Absorption image demonstrating the first successful $|1\rangle \longrightarrow |2\rangle$ RF transfer observed in the ideal gas regime at LMU (February 18, 2024). The side panels show the integrated density profiles, shown here as a reference.

As a comment, we can implement another technique consisting of the automated sweep to excite the sample under the Landau-Zener transition, usually called *adiabatic transition* [69, 108].

4.3 Optimizing the RF spectroscopy

Operating with the antennas in the optimal condition described in Chapter 3, we were able to observe more stable transfers; the oscillations in the number of the newly populated state already fluctuated by 10%. Because the RF emission had been optimized, we could see the transfers for orders of less than a millisecond ($\leq$ 1 ms).

The sequence for verifying reduced transfer times involves two key steps: First, we establish successful state transfer with $20 - 50$ ms pulses, an order of magnitude shorter than initial attempts. Subsequently, we progressively decrease the pulse duration while monitoring the transfer efficiency.

A critical experimental consideration is that the time-image realization must be delayed by at least 500 μs after the RF pulse termination. This delay is necessary because the 100 MHz AOMs are affected by the proximity in terms of time between the RF-antenna signal and the RF range operation of the AOMs.

Fig. 4-5 displays the results for the shortest achieved pulse durations ($\sim$ 800 μs), demonstrating how transfer efficiency varies with output emitted power, which is controlled via input power settings in the KEYSIGHT. The observed oscillatory behavior confirms Rabi dynamics; for fixed pulse durations, the transfer probability follows the expected Rabi oscillation profile as a function of applied RF power, described by (3-4).

Then, each emitted power has a different period of the Rabi oscillation. The optimal power corresponds to the maximal transferred atoms in the minimal duration of the pulse. For this reason, if we see the transferred atoms after a long RF pulse, the transferred number has fluctuations around the 80% because the emission of a non-optimal condition antenna

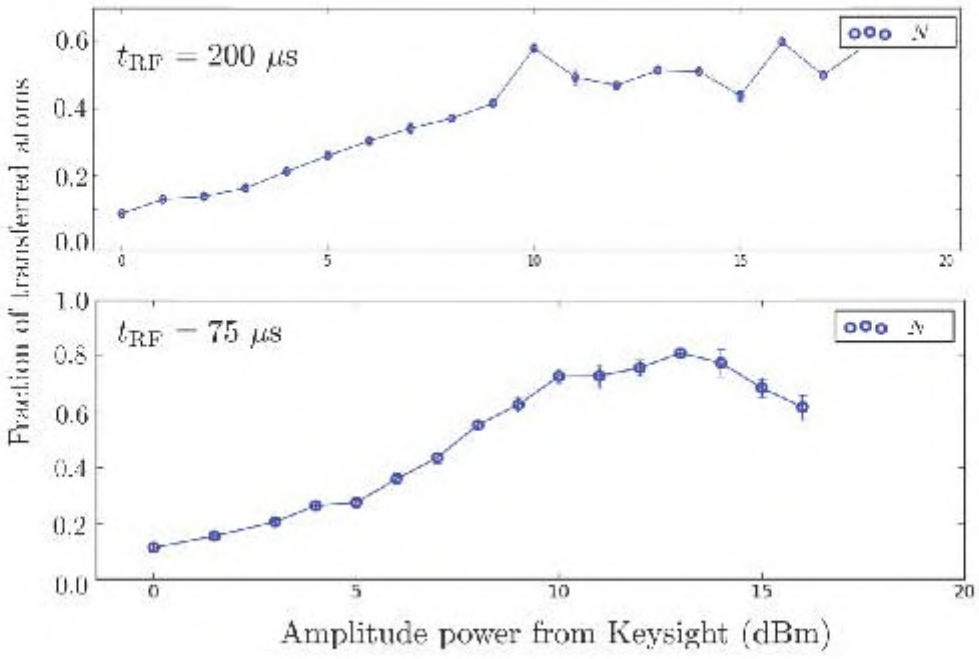

Figure 4-5: Transfer efficiency as a function of RF power. (Top) $|1\rangle \longrightarrow |2\rangle$ transfer at a final ODT power of 50 mW. (Bottom) $|2\rangle \longrightarrow |3\rangle$ transfer at a final ODT power of 70 mW. The fraction transferred is calculated relative to the initial population of the initial state.

is unstable. At the same time, it allows us to discard the fact that the fluctuations in the number of transferred atoms originate in an unstable Feshbach magnetic field.

We observe a tendency to saturated transference after the 10 dBm; we refer this factor to the response of the amplifier. With this information, we work with the interval between 7 and 10 dBm, the amplifier increases +41 dB, which means $\sim$ 100 W. Although we cannot measure the radiated power directly from the antenna at the current position, atoms are the best sensor of its efficiency.

4.4 A strong-interacting system

The selected magnetic field to work with this phenomenon is 73.0 mT, value for which the interaction strength of two types of interactions $|1\rangle - |2\rangle$ and $|2\rangle - |3\rangle$ are equal, as we can see in Fig. 4-6. Performing a sweep like the one conventionally done at 69.0 mT is enough for this interaction regime. At 73.0 mT, the frequency between the $|1\rangle$ and the $|2\rangle$ is 79.109 96 MHz.

The initial attempt to perform the $|1\rangle \longrightarrow |2\rangle$ transfer followed the same protocol developed for the non-interacting case. Modifying the blast parameters, i.e., intensity and duration, with the caution not to destroy both states simultaneously. The solution instead emerged from optimizing the blast timing within the experimental sequence. Before presenting our developed protocol for strongly interacting systems, we explain the blast characteristics beyond the weakly interacting regime.

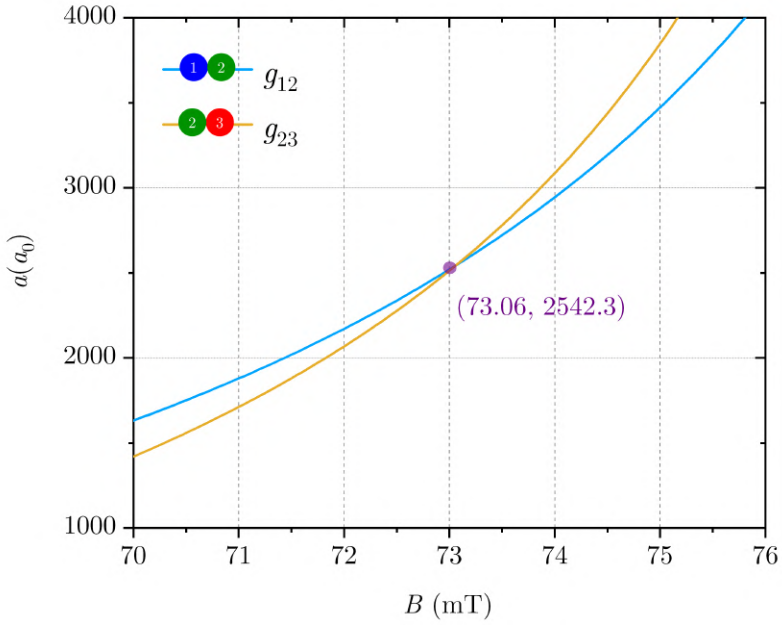

Figure 4-6: Image of the Feshbach resonances for the pairs $|1\rangle - |2\rangle$ and $|2\rangle - |3\rangle$, which have the same scattering length. The Feshbach resonance for the remainder pair is not shown because it is located in the BCS region.

The blast sequence is our primary method for state-selective removal, achieved by exciting atoms to a non-ground electronic state. This procedure constitutes the first light pulse in our imaging subroutine. We modified the standard imaging sequence for this specific operation by eliminating the two subsequent light pulses and turning off all camera triggers. The required frequency for this operation corresponds to the AOM frequency imaging specified in Table 4-1. For the interacting regimes, the blast is performed before being below the critical temperature and before the magnetic field sweep. It is important to note that the blast is done at an offset of the Feshbach field of 83.4 mT, because the binding energy is small compared with other positive values of the $a_s > 0$.

Therefore, the protocol to obtain the first optimal transference at 73.0 mT is the next:

1. Realize the blast of the state $|2\rangle$ during 15 μs. This blast is made when the atomic gas is purely thermal.

2. Make an image of the atoms in both states. We watch the image of the state $|2\rangle$ without losing view of the presence of the state $|1\rangle$.

4. Activate the RF emission. Controlled by the subroutine: *RF-constant.sub* in the control system program. The characteristics of this pulse are shown in the Table 4-3.

5. Perform a sweep of the frequency sending for the KEYSIGHT, moving in the scale of 1kHz in the vicinity of the $\nu_{12}(73.1\text{mT}) = 76.109\ 96$ MHz.

Parameter	Symbol	Value
Magnetic Field	B_0	73.1(3) mT
Transfer Frequency	ν_{12}	76.116 7(2) MHz
Transfer width	$\Gamma_{\nu_{12}}$	2.6(1) kHz
Shift Frequency†	$\Delta\nu_{12}$	~ 7 kHz
Pulse Time	t_{RF}	0.800(10) ms
Power set	P_{K}	+10 dBm

Table 4-3: Parameters used to see the transference $|1\rangle \longrightarrow |2\rangle$ at 73.0 mT (see Fig. 4-7). The power set is the KEYSIGHT output.

Here, the distribution of atoms along the confinement trap is optimal for adjusting the frequency by observing the transferred number. Similar to the imaging process, we scan the frequency and save the population data of each state. We obtain the following graph (Fig. 4-7) with a Lorentzian fitting.

In table 4-3, we change the value of the magnetic field after a recalibration of the magnetic field. Adding Fig. 4-7 reveals a transition with a width of 2.6 kHz, which could be associated with the final temperature value [90]. Some references [21, 22, 109] indicate that the effect of the mean-field is suppressed or in the order of the ~ 5 kHz (in our case). We can consider that the $\Delta\nu_{12}$ comes from the mean-field effect, but it may also include the effect of fluctuation in the Feshbach magnetic field magnitude B_0.

The error bars shown in Fig. 4-7 are obtained with the standard deviation of a set of around seven measures for frequency, being more stable at the top of the transference and in the lower values. The main reason is that the noise difficult counting the minimal transferred atoms.

4.5 Rabi Oscillation in $|1\rangle \longrightarrow |2\rangle$

Once we obtained the transference central frequency $|1\rangle \longrightarrow |2\rangle$, the next step is to study the full transference, duration of the RF signal emission is called $\pi-$pulse, given by the period of the Rabi oscillation, with the Rabi frequency (3-4).

Following the results of the measurements given by Fig. 4-5, the optimal power emitted by KEYSIGHT is 10 dBm. Using the same protocol to observe the first transference, at the 50 mW as the final value of the ODT power, we obtained a Rabi frequency of $\Omega_{R_{12}}/2\pi = 1,329 \pm 13$ Hz and a period of 752 μs. This oscillation is presented in Fig. 4-8, where we selected two images from the imaging software to illustrate the difference in the population observed.

The $\pi-$pulse of the RF transfer corresponds to the full transference, while the $\pi/2-$pulse sends the atoms into a superposition between the two states. All these values are measured and presented in the table 4-4.

We conclude the results of the first measurements for the transference $|1\rangle \longrightarrow |2\rangle$ realized in the LMU. One of the most important results of this procedure is that we can balance the sample in a portion of 50% of each state, which is important to maintain the superfluid state

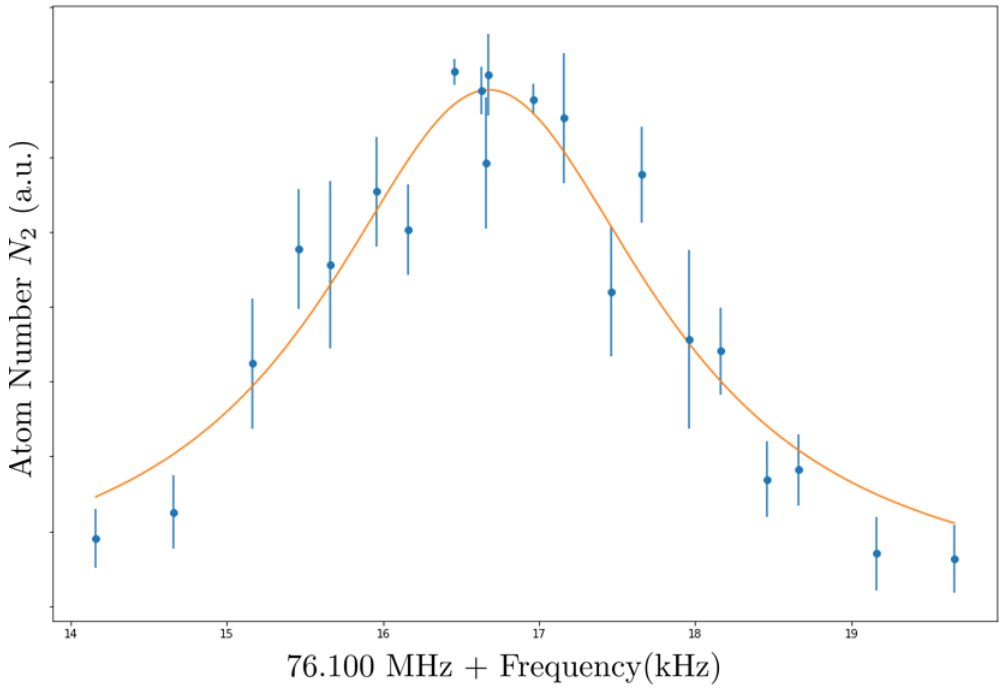

Figure 4-7: RF spectroscopy of the $|2\rangle$ state population after a $|1\rangle \longleftrightarrow |2\rangle$ transfer pulse at $B_0 = 73.0$ mT. The data is fit with a Lorentzian function (orange line)), yielding a center frequency of $\nu_{12} = 76.116\ 68(2)$ Hz and a width of $\Gamma \sim 2.6$ kHz.

Parameter	**Symbol**	**Value**
Power set	P_K	+10 dBm
Rabi Frequency	$\Omega_{R_{12}}$	$2\pi \times 1,329(13)$ Hz
Period	τ_{12}	752(4) μs
$\pi-$pulse	t_π	376(4) μs
$\pi/2-$pulse	$t_{\pi/2}$	188(4) μs

Table 4-4: Principal parameter from the Rabi oscillation for the transfer $|1\rangle \longrightarrow |2\rangle$ measured in the LMU (see Fig. 4-8).

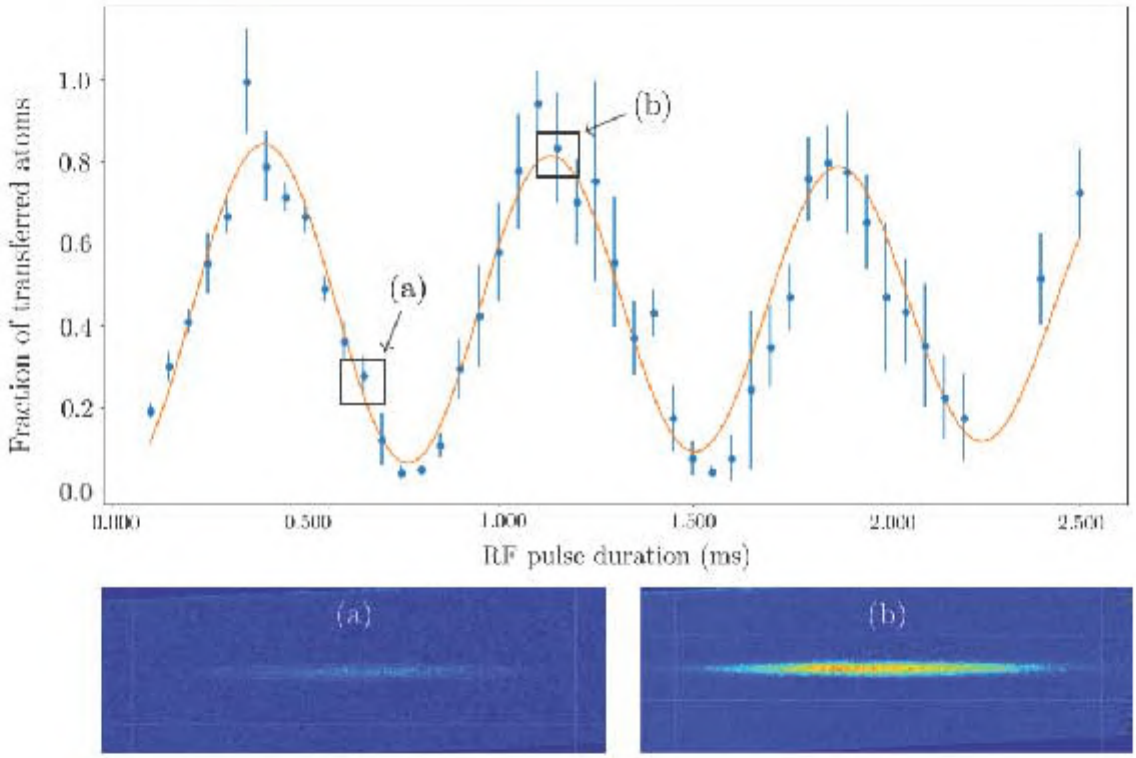

Figure 4-8: Rabi oscillation of the state $|2\rangle$ at the final value of the evaporation ramp associate to 50 mW in control. We identify two images of the cloud (a) for a few transferred atom numbers and (b) one image of the higher transferred.

State	AOM	Frequency (MHz)		
		69.0 mT	71.0 mT	73.0 mT
$\|3\rangle$	rep	200.0	180.0	–
	cool	–	–	90.0
	200 MHz	–	–	–
	350 MHz	325.0	370.0	307.5

Table 4-5: Center frequency settings (in MHz) for the acousto-optic modulators (AOMs) used to image the $|3\rangle$ state at various magnetic fields. A dash (−) indicates that the specific laser beam configuration was not used for imaging at that particular field value

Parameter	Symbol	Value
Magnetic Field	B_0	73.0(3) mT
Transfer Frequency	ν_{12}	82.346 8(4) MHz
Shift Frequency	$\Delta\nu_{23}$	~ -25 kHz
Pulse Time	t_{RF}	180(4) μs
Power set	P_{K}	10 dBm

Table 4-6: Parameters used to see the transference $|2\rangle \longrightarrow |3\rangle$ at 73.1 mT (see Fig. 4-9). The power set is the KEYSIGHT output.

for a long time. The next section explores the first manipulation of the third lower hyperfine state of ^{6}Li.

4.6 The third state

We calculate the energy shift required to observe the state $|3\rangle$ at 73.0 mT. We obtain the central frequency for making an image at this magnetic field using the Breit-Rabi formula. The optimal frequency values for the AOMs are presented in Table 4-5.

We do a similar procedure to obtain this state, explained with the following protocol:

1. Realize the blast of the state $|1\rangle$ with a light shot of 15 μs. This blast is made before crossing the critical temperature for the offset $B_0 = 83.4$ mT.

2. Make an image of the atoms in both states. It means, that we watch the image of the state $|2\rangle$ and in some iterations verify the presence of the state $|1\rangle$.

4. Do not forget to set the frequency and amplitude of the signal in the wave generator.

5. Activate the RF emission. Controlled by the subroutine: *RF-constant.sub* in the control system program. The characteristics of this pulse are shown in the table 4-6.

6. Perform a sweep of the frequency sending for the KEYSIGHT, moving in the scale in steps of 1kHz in the vicinity of the $\nu_{23}(73.0\ \mathrm{mT}) = 82.382\ 4$ MHz.

RF spectroscopy for the state $|3\rangle$ is shown in Fig. 4-9. Here, the shift $\Delta\nu_{23}$ is negative compared to the theoretical value, which is negative and of the order of 20kHz. For this final

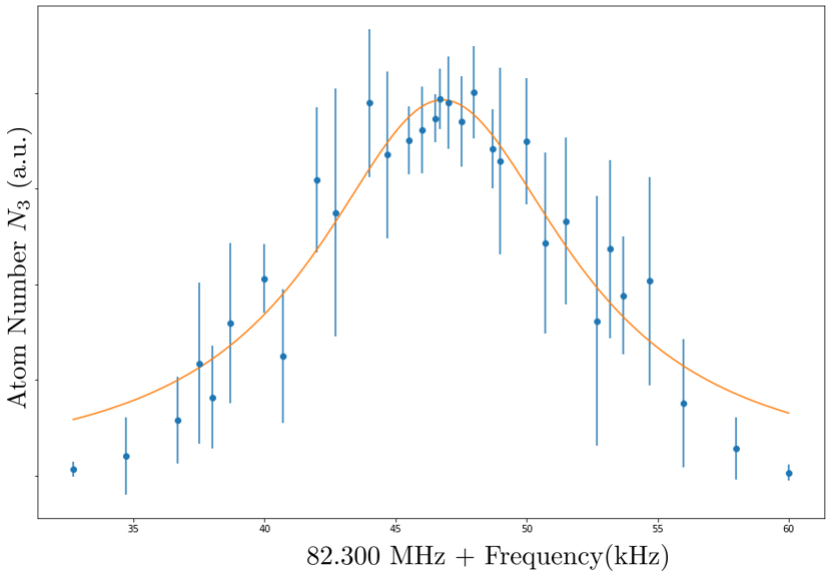

Figure 4-9: RF spectroscopy for the transfer to the $|3\rangle$ state at $B_0 = 73 - 0$ mT. The Lorentzian fit gives a center frequency of $\nu_{23} = 82.346\ 8(4)$ and a width of 11.78 kHz.

value of the power in the last evaporation ramp, we could assume three relevant aspects: (1) the frequency shift of the mean-field, (2) the final temperature of the atomic sample, and (3) the real offset of the magnetic field B_0.

Another aspect to note is the size of the error bars in Fig. 4-9, which, as in Fig. 4-7, are of the order and can represent the fluctuation of the magnetic field. Proceeding as in the case of transfer $|1\rangle \longrightarrow |2\rangle$, the next step is the measurement of the Rabi oscillation.

The Rabi oscillation for the state $|3\rangle$ is a fundamental part of integrating this technique in the experiments where the mean times are in the order of milliseconds. Then, with a power set in the output of the wave generator of +10 dBm, more or less 100 W in the output of the amplifier, the Rabi oscillation is present in Fig. 4-10.

In Fig. 4-10, we integrate a series of four images that correspond to four distinct moments into the Rabi oscillation, from (a) a transfer of less than 30% to (d) a complete transfer. For a final value of 50 mW of the last evaporation ramp, the Rabi frequency is $\Omega_{R_{23}}/2\pi = 2,800 \pm 30$ Hz and a period of $\tau_{23} = 357$ μs.

Other characteristic values for this phenomenon are collected in the Table 4-7. We highlight the maximum transfer time, $\pi-$pulse, $t_\pi = 178.5$ μs. This short time, in comparison with the lifetime of the ultracold sample (~ 500 ms), was obtained thanks to all the improvements presented in this work. It is ideal for integrating into the future routines of the collective excitations or exploring problems with impurities or balanced samples of three species.

The last figure contains two Rabi oscillations in the same system but from two possible perspectives: the transferred state and the complementary state, where the atoms are transferred. In the following, we discuss the most important elements of Fig. 4-11.

The two measurements show the Rabi oscillation for the transfer $|2\rangle \longrightarrow |3\rangle$. The red data

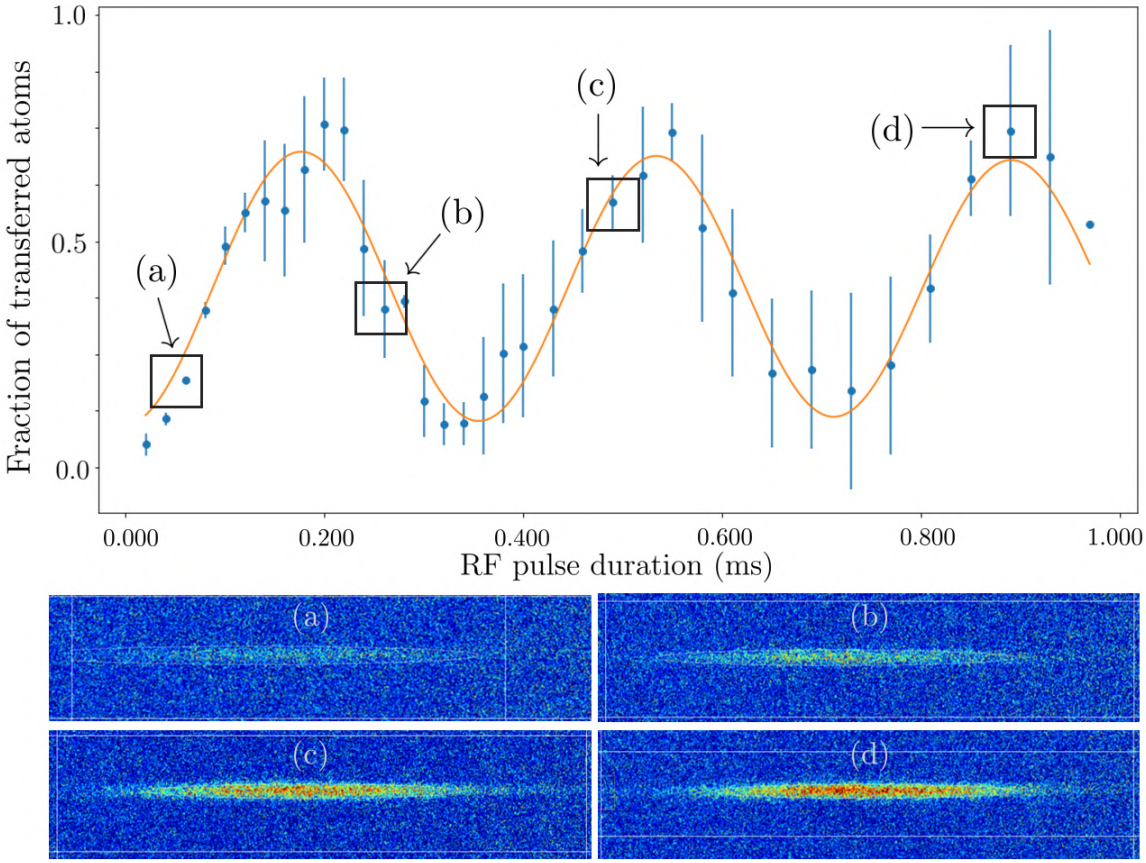

Figure 4-10: Rabi oscillation of the state $|3\rangle$ at the final value of the evaporation ramp associate to 50 mW sent in control program. We use four images to depict (a) a poor transference, (b) a transference in the near of a $\pi/2-$pulse, (c) a transference of more than the 75%, and (d) a fully transferred $|3\rangle$ system.

Parameter	**Symbol**	**Value**
Power set	P_K	+10 dBm
Rabi Frequency	$\Omega_{R_{23}}$	$2\pi \times 2,800(31)$ Hz
Period	τ_{23}	357(4) μs
$\pi-$pulse	t_π	178.5(4) μs
$\pi/2-$pulse	$t_{\pi/2}$	89.3(4) μs

Table 4-7: Parameters from the Rabi oscillation for the transfer $|2\rangle \longrightarrow |3\rangle$ measured in the LMU (see Fig. 4-10).

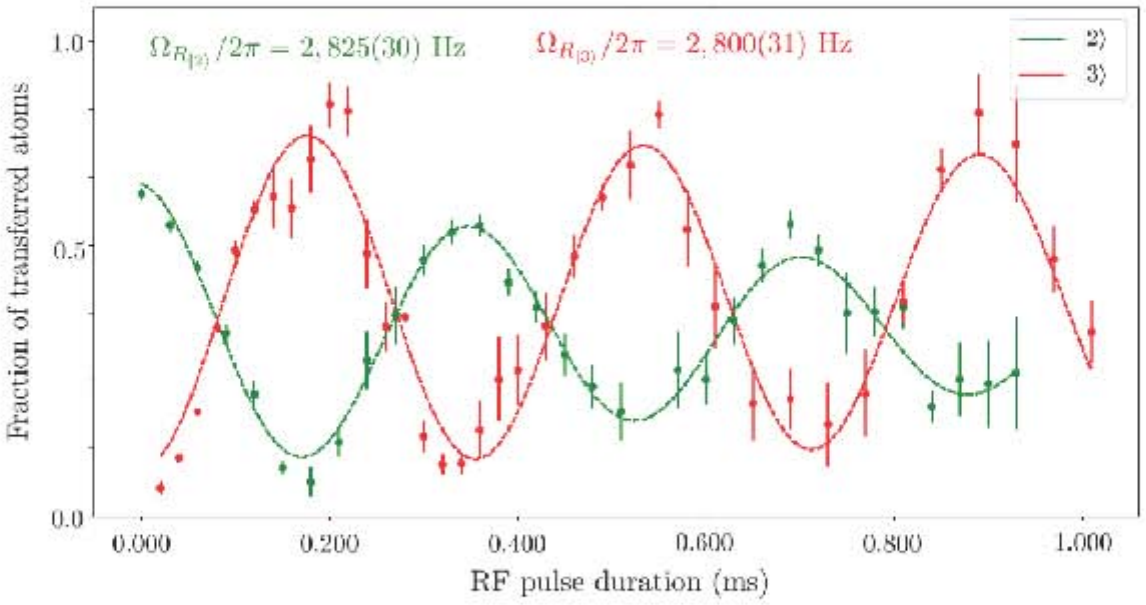

Figure 4-11: Rabi oscillations for the $|2\rangle \longrightarrow |3\rangle$ transfer at $B_0 = 73.0$ mT, showing the complementary populations of state $|2\rangle$ (green, 36 mW ODT) and state $|3\rangle$ (red, 50 mW ODT). The oscillations are counter-phase and share the same frequency $\Omega_{R_{23}}/2\pi = 2.8$ kHz. Damping in the green data is attributed to increased interactions at lower temperature.

is for the population of the state $|3\rangle$, while the green data is for the population of the state $|2\rangle$. The most important difference is that the final evaporation value conditions are not the same: for state $|2\rangle$, the value is 36 mW, while for state $|3\rangle$, it is 50 mW. However, the RF pulse condition is the same in both.

The error bars correspond to the standard error and are therefore shown differently compared to Fig. 4-10. We can observe that in both cases, the pulse increases, and the data dispersion also increases. This effect is attributed to both the amplifier and the antenna output.

We can notice the attenuation in the state $|2\rangle$ population oscillation, which is not noticeable with state $|3\rangle$. This effect is caused by the fact that when we reach a lower temperature, the interactions between the states start to complicate the transfer.

A final factor to rule out is that both events show the same frequency, with the respective counter-phase. Both Rabi frequencies are ordered at 2.8 kHz. This result is appropriate for the times manipulated in the experiment. It shows that the proximity of the antenna (overcoming the decay of the radiated magnetic field) and impedance optimization (reducing reflections in the signal) were crucial.

4.7 Remarks

We need to clarify some details to bring a successful RF transfer:

- We need to pay attention to and exercise caution regarding the loads in the input

and output of the amplifier. In principle, in the output we have a short circuit with an antenna terminal by its very low impedance, around tenth Ω, but connecting any element of high power radiation is necessary. In the input, checking that the amplifier is turned on before applying any signal is necessary. These cautions are very important to avoid damaging the device.

- The position of the antenna is critical due to the physical conditions of the experiment, in particular, the framework in steel. 5 cm marks the difference between transfer and not.
- We recommended only one antenna for any RF frequencies. We implemented a dual-antenna configuration because we do not have a commercial balun optimized for the operating range.
- We note that the originally used long pulse durations ($\sim 10^{-1}$ s) pose risks to high-power amplifiers, even when driven with low input power from the KEYSIGHT source. The pulse duration can disturb the electronics involved in the experimental sequence. We emphasize avoiding such extended pulse durations in future operations.
- From the beginning, it is necessary to design an antenna inside the science chamber, with an orthogonal position related to the quantization axis.

Following these technical considerations, we realized operational tests with the antenna system described in Chapter 3.

Chapter 5

Conclusions and Perspectives

5.1 Conclusions

The main objective of LMU is to manipulate and control quantum matter, specifically with ultracold Fermi gases. The selection of the fermionic isotope of lithium is far from arbitrary; rather, it reflects its profound potential for revealing complex quantum phenomena. Although this work provides the fundamental tool and technique to perform transitions in the hyperfine Zeeman states accessible in the LMU experiment, it underscores the significance of lithium-based systems. Working with lithium presents substantial experimental challenges, and this text exposes the use and function of the RF technique to incorporate into the LMU. A summary of the main results follows, accompanied by a brief discussion and a forward-looking perspective on promising avenues for future research.

In Chapter 1, we provide a brief overview of the lithium atom, treating it as a hydrogen-like system and using concepts accessible to an advanced undergraduate or graduate physics student. The second part introduces the lithium-6 isotope and its fermionic nature, reviewing the case of a free Fermi gas and delving into the experimental setup capable of cooling the lithium gas to some of the lowest temperatures in the known universe.

Then, we introduce the physical foundations that make up the lithium system. In Chapter 2, we briefly explain that a fermionic system at ultra-low temperatures has enabled LMU to explore the behavior of degenerate systems at low energies. The formation of molecular pairs in the context of BEC or Cooper pairs within the BCS interaction regime, covering the crossover between both. This ability to transition between interaction regimes for pairs of distinguishable atoms is known as Feshbach resonance tuning.

Feshbach resonances play a crucial role. Lithium presents a particularly compelling case due to the broad Feshbach resonance observed between the hyperfine states commonly employed in experiments. Furthermore, as demonstrated in this work, including the next accessible hyperfine state gives rise to two additional resonances, corresponding to the remaining pairwise combinations. These resonances are located nearby and exhibit comparable widths.

The main results obtained in the laboratory system are presented from Chapter 3 onwards.

Chapter 3 highlights one of the most significant infrastructure advances at the LMU: the development of radio frequency (RF) antennas. This Chapter details the design and fabrication of two antennas optimized to efficiently emit within the $75 - 83$ MHz range while minimizing signal reflection. Unfortunately, their simultaneous operation is currently limited by the absence of a high-power RF switch or secondary amplifier. However, the results are from manipulating only the waveform generator integrated into the control system.

As we demonstrate in this work, the LMU already has access to a third hyperfine state, as well as manipulation of transference between state $|1\rangle$ and $|2\rangle$ through the RF signals emitted by the antennas developed in Chapter 3. That is, the antennas work. It should be noted that the results presented here reflect the final optimized configurations, the product of extensive iterative refinements that ultimately produced the central satisfactory results of this study.

RF spectroscopy has a well-established history in cold and ultracold systems [22, 89, 94–96], particularly in LMU, with initial efforts documented in [110]. While this work builds on the fundamental concepts and impedance matching circuits described therein, our present project has been developed independently, with substantial modifications and new components designed from scratch.

With Chapter 4, we can conclude several aspects of relevance: We have shown the first non-interacting Fermi gas of two species observed. For the 73 mT case, we have access to the third state as well as the concrete manipulation between state $|1\rangle$ and $|2\rangle$. With these results, we can establish the beginning of the manipulation of three states in the quantum sample of the LMU.

We have achieved the effective transfers $|1\rangle \longrightarrow |2\rangle$ and $|2\rangle \longrightarrow |3\rangle$ for the 73 mT magnetic field offset with the frequencies of $\nu_{12} = 76.116\ 7(2)$ MHz and $\nu_{23} = 82.346\ 8(4)$ MHz respectively. Also, we have measured the Rabi oscillations for each transition, obtaining frequencies of a few kilohertz: $\Omega_{R_{12}}/2\pi = 1,329(13)$ Hz and $\Omega_{R_{23}}/2\pi = 2,800(31)$ Hz.

As a last comment about the experimental work performed, we emphasize that the RF pulses should be emitted according to what we established in the comments of Chapter 4, seeking to have less than one-millisecond emission. Another consideration is the possibility of the visualization of the third state, which reveals a shift in the frequency image comparable with the molecular binding of the initial states $|1\rangle - |2\rangle$, and the possibility of the suppressed mean-field effects is carried on this shift. This last observation opens more possibilities for exploration and new opportunities to understand the behavior of systems with three components.

5.2 Perspectives

Under the current conditions at LMU, the outlook is promising and with a wide range of opportunities, particularly with the recent accessibility of the third hyperfine state. In what follows, we outline several ideas and prospective directions for investigating the controlled manipulation of three hyperfine states of ^{6}Li within the framework of quantum matter.

5.2.1 Exploration in other Regimes

When writing this Thesis, we successfully characterized population transfer to state $|3\rangle$ for the 73.0 mT Feshbach magnetic field, one of the three fields of interest mentioned in Chapter 3. Due to experimental constraints, we have excluded the 52.7 mT from further consideration: the resulting atomic cloud geometry would require significant modifications to the high-resolution vertical imaging system. The next natural step is to extend the visualization of this phenomenon to other accessible magnetic field regions through the anticipated limitations imposed by the available AOM frequency ranges. Characterizing the feasibility of observing the state $|3\rangle$, our advantage in such cases lies in the remainder of the optical molasses process, which allows us to determine the regions accessible by the current system.

As mentioned above, one of the closest applications is the characterization of magnetic field stability [3] because these transitions are a more accurate tool for determining the value of the magnetic field. Following our results, the shift frequency $\Delta\nu_{23} \sim -20$ kHz present in the state $|3\rangle$ transfer would reveal a field uncertainty of up to 0.4 mT, taking into account of a mean-field shift of the order of the saw in transfer $|1\rangle \longrightarrow |2\rangle$.

5.2.2 Inheritance of excitations

This work was conceived in parallel to the main focus of the LMU: the study of turbulence in superfluids of fermionic origin. The middle step, the current position, is the study of collective excitations in superfluids [111]. Furthermore, access to a third spin species and manipulation of the populations for the case where a single antenna can be optimized for the entire required frequency range would provide insight into one of the phenomena that have been recently explored.

Faraday waves are one of the excitations currently being studied in the LMU [111], and the objective is to study this phenomenon in the non-repulsive regimes (unitary and BCS). One technique is to perform population transfers without requiring ultrafast magnetic field sweeps. The ability to transfer the populations should be considered when at least two of the three accessible states are present. That is, studying the transition of a molecule to a non-localized pair.

Soon, the LMU will be able to perform confinement in an oblate trap. In addition to manipulating the optical potential, it gives control over the confinement and behavior of the sample. In these geometries, the study of excitations in the density of the sample has already been studied [112]. Therefore, studying with three species in this new geometry enriches the possibilities of exploring the inheritance of the collective modes produced in the superfluid system.

5.2.3 Impurities

By manipulating the duration of the RF pulses, which are in the time resolution range of the experiment, the portion of transferred atoms can be controlled, thus having a third species

playing the role of impurity. The technique consists of transferring a little part of any state into another vacuum state, for example, having a mixture $|1\rangle - |2\rangle$ apply the RF signal to excite a few of the existing $|2\rangle$ into the $|3\rangle$.

Integrating a fermionic impurity into a bosonic superfluid gas could be studied from quasiparticle polaron theory [113, 114], whose experimental realization is not far off. In the same direction, an experimental realization in a system of composite of bosons, formed by bound fermions, and a fermionic impurity could reproduce the observations by [115].

5.2.4 Mixtures

Research with three distinguishable fermion species opens the potential to arrive at balanced populations, no impurities, and broad-tuning interactions along the Feshbach resonances (see Fig. 2-5), making the combinations BEC-Unitary (69.0 mT) or BEC-BCS (73.0 mT).

Turning the sample from a weakly interacting $|1\rangle - |2\rangle$ into a strongly repulsive Fermi gas $|1\rangle - |3\rangle$ was explored in [116], this realization made at the 69.0 mT magnetic field offset, the Feshbach resonance for the $|1\rangle - |3\rangle$ interactions. Since the LMU system shares the fundamental conditions with the cited experiment, we could perform the higher transfer from state $|2\rangle$ into the state $|3\rangle$, obtaining a different mixture for the initial conditions.

Another possibility to reproduce is the study and measurements of binding pair energy through the Feshbach resonance, as in [90]. Having this result, we can translate to a system with a balanced mixture of atoms in the three accessible spin species of ^{6}Li [23].

In all cases, it is necessary to investigate the experimental implementation of the corresponding protocols adapted to the requirements of the LMU.

5.2.5 Superfluidity

The superfluidity phenomenon for an ultracold fermionic system is related through the critical temperature crossing, as shown in Fig. 2-2. The LMU has experience producing superfluids by the mixture $|1\rangle - |2\rangle$. Therefore, the next step may be exploring the superfluidity in a three-component spin system. In the actual panorama, work explores this physical behavior [77, 117].

Limited by the range of the image given by the AOM system, the LMU can explore the formation of tripartite bonds of three distinguishable fermions creating Efimov states. An estimate of this possibility is presented in [118].

Within the framework of tripartite bonding, it is instructive to draw analogies with quantum chromodynamics (QCD), adopting the nomenclature of color charge and baryon formation to describe interactions in three-species ultracold atomic systems [119]. In such systems, the notion of color superfluidity has been proposed [120]. This frontier area of physics is emerging as a promising theoretical landscape that can be realized using a three-species system such as the one envisioned in future experiments at LMU.

Under the conception of the formation of tripartite bonds, it is practical to associate this structure with those of QCD, using the nomenclatures of color and the baryon formation,

but applied to three-species ultracold systems [119]. For this type of system, the concept of superfluidity of color is determined [120]. This field of frontier physics is emerging as a theory that can be explored from a three-species system like the one that can be prepared at LMU in the future.

Then, the access and manipulation of the third species have a whole range of applications and fields of knowledge where we can contribute and continue to advance the quantum matter domain.

Appendix A

Imaging detuning considerations

We use absorption imaging to measure the properties of ultra-cold or cold samples. This laser beam is separate from the light used in the molasses process. Its frequency is precisely controlled using acousto-optic modulators (AOMs) [121], which diffract the beam into multiple diffraction orders. The appropriate order is selected to obtain resonant light to transition between the state we wish to observe and some hyperfine state of $2^2P_{3/2}$.

The imaging transition frequency is computed by considering the sample under a constant magnetic field, using the Breit-Rabi formula and the numerical diagonalization method for the Hamiltonian that includes the Zeeman effect. In Chapter 1, we reviewed all these conditions.

The imaging frequency must match the contributions of all frequency shifts provided by the AOM mounted in the experimental setup, as follows:

$$\Delta\nu_{\text{transition}} = 2 \times \left(-\nu_{\text{zero-B}} + \nu_{\text{MOPA}} - \nu_{\text{slower}} - \nu_{\text{img}}\right), \tag{A-1}$$

where the frequency $\nu_{\text{zero-B}}$ represents the value at the zero magnetic field transition, which is circa 216.2 MHz; the ν_{MOPA} is given for the cooling or repumper configuration centred at 80 MHz and 200 MHz respective; ν_{slower} is the frequency of the Zeeman slower optical configuration, fixed at 194.8 MHz; finally, the ν_{img} corresponds to the frequency proper of the imaging optical setup. The signs represent the orders selected in each AOM, and the 2 factor is for the double-pass configurations.

Fig. (A-1) outlines the frequency shifts applied by the AOMs used in the last expression. The leftmost gray block denotes the set frequency used throughout the experimental sequence. Subsequent frequency adjustments are made for cooling and repumping configurations shown in the gray boxes, calibrated to match the shift requirements.

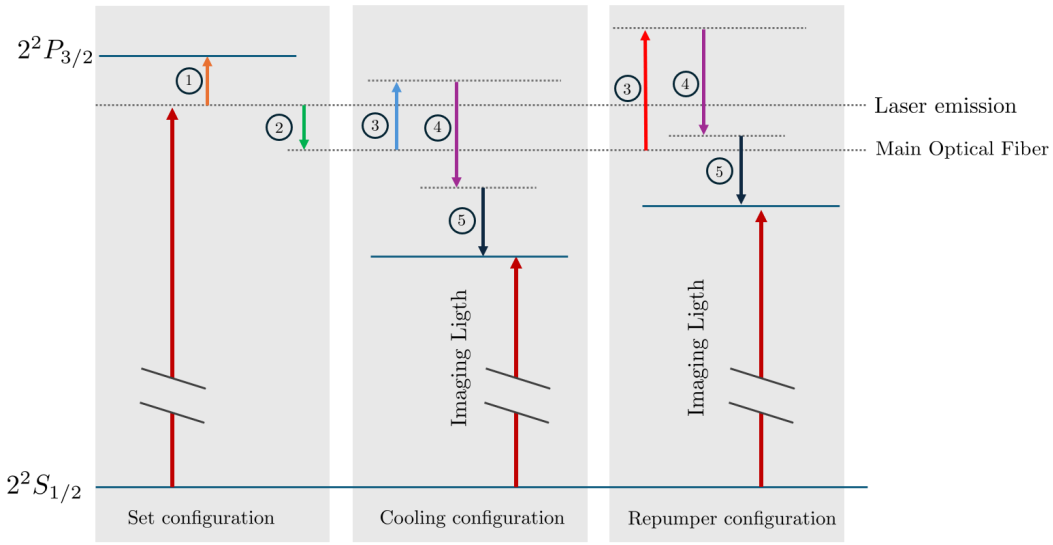

Figure A-1: Diagram of the use of the AOM shifters. The preparation is divided into two parts: Set configuration (left gray block), the red arrow represents the light emitted by the laser, and the (1) orange little arrow is the correction made by the AOM of SAS (Saturated Absorption Spectroscopy) and helps to fix the line transition in the laser; (2) green arrow is the action of the switch AOM before separated the cooling configuration (middle gray block) or the repumper configuration (right gray block). In both options, we have the (3) election of the AOM (cooling-blue trace, repumper-red arrow), and then the next change in the frequency is given by the (4) Slower AOM identified by the purple arrow. Finally, the compensation is obtained by the (5) black arrow that corresponds to the AOM centered in 350 MHz or 200 sume.

Bibliography

[1] W. Ketterle and M. W. Zwierlein, *Making, Probing and Understanding Ultracold Fermi Gases*. Rivista del nuovo cimento, Societa italiana di fisica, 2008.

[2] C. Chin, R. Grimm, P. Julienne, and E. Tiesinga, "Feshbach resonances in ultracold gases," *Rev. Mod. Phys.*, vol. 82, pp. 1225–1286, 2010.

[3] G. Zürn, T. Lompe, A. N. Wenz, S. Jochim, P. S. Julienne, and J. M. Hutson, "Precise characterization of ^{6}Li feshbach resonances using trap-sideband-resolved rf spectroscopy of weakly bound molecules," *Phys. Rev. Lett.*, vol. 110, p. 135301, Mar 2013.

[4] D. Dew-Hughes, "The critical current of superconductors: an historical review," *Low Temperature Physics*, vol. 27, pp. 713–722, 09 2001.

[5] B. Yan and S.-C. Zhang, "Topological materials," *Reports on Progress in Physics*, vol. 75, p. 096501, aug 2012.

[6] F. Oba and Y. Kumagai, "Design and exploration of semiconductors from first principles: A review of recent advances," *Applied Physics Express*, vol. 11, p. 060101, may 2018.

[7] K. O. Ho, Y. Shen, Y. Y. Pang, W. K. Leung, N. Zhao, and S. Yang, "Diamond quantum sensors: from physics to applications on condensed matter research," *Functional Diamond*, vol. 1, no. 1, pp. 160–173, 2021.

[8] M. H. Anderson, J. R. Ensher, M. R. Matthews, C. E. Wieman, and E. A. Cornell, "Observation of bose-einstein condensation in a dilute atomic vapor," *Science*, vol. 269, no. 5221, pp. 198–201, 1995.

[9] K. B. Davis, M. O. Mewes, M. R. Andrews, N. J. van Druten, D. S. Durfee, D. M. Kurn, and W. Ketterle, "Bose-einstein condensation in a gas of sodium atoms," *Phys. Rev. Lett.*, vol. 75, pp. 3969–3973, Nov 1995.

[10] C. C. Bradley, C. A. Sackett, J. J. Tollett, and R. G. Hulet, "Evidence of bose-einstein condensation in an atomic gas with attractive interactions," *Phys. Rev. Lett.*, vol. 75, pp. 1687–1690, Aug 1995.

[11] J. K. Chin, D. Miller, Y. Liu, C. Stan, W. Setiawan, C. Sanner, K. Xu, and W. Ketterle, "Evidence for superfluidity of ultracold fermions in an optical lattice," *Nature*, vol. 443, no. 7114, pp. 961–964, 2006.

[12] S. Sunami, V. P. Singh, D. Garrick, A. Beregi, A. J. Barker, K. Luksch, E. Bentine, L. Mathey, and C. J. Foot, "Observation of the berezinskii-kosterlitz-thouless transition in a two-dimensional bose gas via matter-wave interferometry," *Phys. Rev. Lett.*, vol. 128, p. 250402, Jun 2022.

[13] M. Greiner, C. A. Regal, and D. S. Jin, "Emergence of a molecular bose-einstein condensate from a fermi gas," *Nature*, vol. 426, no. 6966, pp. 537–540, 2003.

[14] C. A. Regal, C. Ticknor, J. L. Bohn, and D. S. Jin, "Creation of ultracold molecules from a fermi gas of atoms," *Nature*, vol. 424, no. 6944, pp. 47–50, 2003.

[15] B. DeMarco and D. S. Jin, "Onset of fermi degeneracy in a trapped atomic gas," *Science*, vol. 285, no. 5434, pp. 1703–1706, 1999.

[16] A. G. Truscott, K. E. Strecker, W. I. McAlexander, G. B. Partridge, and R. G. Hulet, "Observation of fermi pressure in a gas of trapped atoms," *Science*, vol. 291, no. 5513, pp. 2570–2572, 2001.

[17] T. Fukuhara, Y. Takasu, M. Kumakura, and Y. Takahashi, "Degenerate fermi gases of ytterbium," *Phys. Rev. Lett.*, vol. 98, p. 030401, Jan 2007.

[18] M. Lu, N. Q. Burdick, and B. L. Lev, "Quantum degenerate dipolar fermi gas," *Phys. Rev. Lett.*, vol. 108, p. 215301, May 2012.

[19] S. Baier, D. Petter, J. H. Becher, A. Patscheider, G. Natale, L. Chomaz, M. J. Mark, and F. Ferlaino, "Realization of a strongly interacting fermi gas of dipolar atoms," *Phys. Rev. Lett.*, vol. 121, p. 093602, Aug 2018.

[20] D. Hernandez-Rajkov, J. E. Padilla-Castillo, M. Mendoza-Lopez, R. Colin-Rodriguez, A. Gutierrez-Valdes, S. A. Morales-Ramirez, R. A. Gutierrez-Arenas, C. A. Gardea-Flores, R. Jauregui-Renaud, J. A. Seman, F. J. Poveda-Cuevas, and G. Roati, "Experimental setup for the production of ultracold strongly correlated fermionic superfluids of 6li," *Rev. Mex. Fis.*, vol. 66, p. 388–403, 2020.

[21] F. Scazza, G. D. Pace, L. Pieri, R. Concas, W. J. Kwon, and G. Roati, "An efficient high-current circuit for fast radio-frequency spectroscopy in cold atomic gases," 2021.

[22] S. Gupta, Z. Hadzibabic, M. W. Zwierlein, C. A. Stan, K. Dieckmann, C. H. Schunck, E. G. M. van Kempen, B. J. Verhaar, and W. Ketterle, "Radio-frequency spectroscopy of ultracold fermions," *Science*, vol. 300, no. 5626, pp. 1723–1726, 2003.

[23] T. B. Ottenstein, T. Lompe, M. Kohnen, A. N. Wenz, and S. Jochim, "Collisional stability of a three-component degenerate fermi gas," *Phys. Rev. Lett.*, vol. 101, p. 203202, Nov 2008.

[24] J. H. Huckans, J. R. Williams, E. L. Hazlett, R. W. Stites, and K. M. O'Hara, "Three-body recombination in a three-state fermi gas with widely tunable interactions," *Phys. Rev. Lett.*, vol. 102, p. 165302, Apr 2009.

[25] A. J. Leggett, "Macroscopic quantum systems and the quantum theory of measurement," *Progress of Theoretical Physics Supplement*, vol. 69, pp. 80–100, 1980.

[26] I. Mills, T. Cvitas, K. Homann, N. Kallay, and K. Kuchitsu, *Quantities, Units, and Symbols in Physical Chemistry*. Oxford: Blackwell Scientific Publishing, 1988.

[27] R. C. Weast, M. J. Astle, and W. H. Beyer, eds., *CRC Handbook of Chemistry and Physics*. Boca Raton: CRC Press, 64th ed., 1983.

[28] D. Lide, *CRC Handbook of Chemistry and Physics, 85th Edition*. No. v. 85 in CRC Handbook of Chemistry and Physics, 85th Ed, Taylor & Francis, 2004.

[29] E. Cohen, R. S. of Chemistry (Great Britain), I. U. of Pure, A. C. Physical, and B. C. Division, *Quantities, Units and Symbols in Physical Chemistry*. Royal Society of Chemistry, 2007.

[30] K. Pachucki, V. Patkóš, and V. A. Yerokhin, "Accurate determination of 6,7li nuclear magnetic moments," *Physics Letters B*, vol. 846, p. 138189, 2023.

[31] B. Bransden and C. Joachain, *Physics of Atoms and Molecules*. Pearson Education, Prentice Hall, 2003.

[32] N. Zettili, *Quantum Mechanics: Concepts and Applications*. Wiley, 2009.

[33] L. J. Radziemski, R. Engleman, and J. W. Brault, "Fourier-transform-spectroscopy measurements in the spectra of neutral lithium, ^{6}I and ^{7}I (li i)," *Phys. Rev. A*, vol. 52, pp. 4462–4470, Dec 1995.

[34] W. I. McAlexander, E. R. I. Abraham, and R. G. Hulet, "Radiative lifetime of the $2p$ state of lithium," *Phys. Rev. A*, vol. 54, pp. R5–R8, Jul 1996.

[35] R. Li, Y. Wu, Y. Rui, B. Li, Y. Jiang, L. Ma, and H. Wu, "Absolute frequency measurement of ^{6}Li d lines with khz-level uncertainty," *Phys. Rev. Lett.*, vol. 124, p. 063002, Feb 2020.

[36] R. C. Brown, S. Wu, J. V. Porto, C. J. Sansonetti, C. E. Simien, S. M. Brewer, J. N. Tan, and J. D. Gillaspy, "Quantum interference and light polarization effects in unresolvable atomic lines: Application to a precise measurement of the ^{6,7}li D_2 lines," *Phys. Rev. A*, vol. 87, p. 032504, Mar 2013.

[37] E. Arimondo, M. Inguscio, and P. Violino, "Experimental determinations of the hyperfine structure in the alkali atoms," *Rev. Mod. Phys.*, vol. 49, pp. 31–75, Jan 1977.

[38] J. Walls, R. Ashby, J. J. Clarke, B. Lu, and W. A. van Wijngaarden, "Measurement of isotope shifts, fine and hyperfine structure splittings of the lithium d lines," *The European Physical Journal D - Atomic, Molecular, Optical and Plasma Physics*, vol. 22, no. 2, pp. 159–162, 2003.

[39] J. Stark, "Beobachtungen über den effekt des elektrischen feldes auf spektrallinien. i. quereffekt," *Annalen der Physik*, vol. 348, no. 7, pp. 965–982, 1914.

[40] C. Pethick and H. Smith, *Bose–Einstein Condensation in Dilute Gases*. Cambridge University Press, 2002.

[41] D. Steck, *Quantum and Atom Optics*. 2007.

[42] P. Zeeman, "The effect of magnetisation on the nature of light emitted by a substance," *Nature*, vol. 55, no. 1424, pp. 347–347, 1897.

[43] P. Zeeman, "Vii. doublets and triplets in the spectrum produced by external magnetic forces," *The London, Edinburgh, and Dublin Philosophical Magazine and Journal of Science*, vol. 44, no. 266, pp. 55–60, 1897.

[44] A. Landé, "Termstruktur und zeemaneffekt der multipletts," *Zeitschrift für Physik*, vol. 19, no. 1, pp. 112–123, 1923.

[45] G. Breit and I. I. Rabi, "Measurement of nuclear spin," *Phys. Rev.*, vol. 38, pp. 2082–2083, Dec 1931.

[46] W. Pauli, "The connection between spin and statistics," *Phys. Rev.*, vol. 58, pp. 716–722, Oct 1940.

[47] R. K. Pathria, *Statistical Mechanics: International Series of Monographs in Natural Philosophy*, vol. 45. Elsevier, 2017.

[48] J. Szczepkowski, R. Gartman, M. Witkowski, L. Tracewski, M. Zawada, and W. Gawlik, "Analysis and calibration of absorptive images of bose–einstein condensate at nonzero temperatures," *Review of Scientific Instruments*, vol. 80, p. 053103, 05 2009.

[49] B. Ohayon and G. Ron, "New approaches in designing a zeeman slower," *J. Instrum.*, vol. 8, no. 02, p. P02016, 2013.

[50] Y. Castin, H. Wallis, and J. Dalibard, "Limit of doppler cooling," *J. Opt. Soc. Am. B*, vol. 6, pp. 2046–2057, Nov 1989.

[51] C. Foot, *Atomic Physics*. Oxford Master Series in Physics, OUP Oxford, 2005.

[52] R. G. Hulet, J. H. V. Nguyen, and R. Senaratne, "Methods for preparing quantum gases of lithium," *Rev. Sci. Instrum.*, vol. 91, no. 1, p. 011101, 2020.

[53] A. Aspect, E. Arimondo, R. Kaiser, N. Vansteenkiste, and C. Cohen-Tannoudji, "Laser cooling below the one-photon recoil energy by velocity-selective coherent population trapping," *Phys. Rev. Lett.*, vol. 61, pp. 826–829, 1988.

[54] J. Hack, L. Liu, M. Olshanii, and H. Metcalf, "Velocity-selective coherent population trapping of two-level atoms," *Phys. Rev. A*, vol. 62, p. 013405, 2000.

[55] A. Burchianti, G. Valtolina, J. A. Seman, E. Pace, M. De Pas, M. Inguscio, M. Zaccanti, and G. Roati, "Efficient all-optical production of large ^{6}Li quantum gases using D_1 gray-molasses cooling," *Phys. Rev. A*, vol. 90, p. 043408, 2014.

[56] C. L. Satter, S. Tan, and K. Dieckmann, "Comparison of an efficient implementation of gray molasses to narrow-line cooling for the all-optical production of a lithium quantum gas," *Phys. Rev. A*, vol. 98, p. 023422, Aug 2018.

[57] D. Hernández Rajkov, "Tesis de licenciatura: Enfriamiento doppler y sub-doppler de un gas atómico de litio-6." Facultad de Ciencias - Universidad Nacional Autónoma de México, 2018.

[58] V. S. Moralez-Guzmán, "Enfriamiento sub-doppler tipo melaza gris para dos isótopos de litio." Facultad de Ciencias - Universidad Nacional Autónoma de México, 2022.

[59] A. Ashkin, "Trapping of atoms by resonance radiation pressure," *Phys. Rev. Lett.*, vol. 40, pp. 729–732, Mar 1978.

[60] W. Ketterle and N. V. Druten, "Evaporative cooling of trapped atoms," vol. 37 of *Advances In Atomic, Molecular, and Optical Physics*, pp. 181–236, Academic Press, 1996.

[61] P. Vargas-Vélez, "Objetivo de microscopio de alta resolución para diagnóstico y manipulación de sistemas ultrafríos." Facultad de Ciencias - Universidad Nacional Autónoma de México, 2022.

[62] D. Hernández Rajkov, "Tesis de maestría: Non-destructive and high resolution imaging techniques for studying ultracold quantum gases." Instituto de Física - Universidad Nacional Autónoma de México, 2021.

[63] I. L. Kofsky and H. Levinstein, "A dynamic method for the determination of the velocity distribution of thermal atoms," *Phys. Rev.*, vol. 74, pp. 500–500, Aug 1948.

[64] E. I. García-Padilla, "Diseño de los sistemas de ultra-alto vacío y de control para experimentos con gases cuánticos de litio." Facultad de Ciencias - Universidad Nacional Autónoma de México, 2016.

[65] L. Pitaevskii and S. Stringari, *Bose-Einstein Condensation*. International Series of Monographs on Physics, Clarendon Press, 2003.

[66] L. Pitaevskii and S. Stringari, *Bose-Einstein Condensation and Superfluidity*. International Series of Monographs on Physics, OUP Oxford, 2016.

[67] L. de la Peña, *Introducción a la mecánica cuántica*. Ediciones Científicas Universitarias, Fondo de Cultura Economica, 2014.

[68] G. B. Arfken and H. J. Weber, *Mathematical methods for physicists; 4th ed.* San Diego, CA: Academic Press, 1995.

[69] L. Landau and E. Lifshitz, *Quantum Mechanics: Non-Relativistic Theory*. Course of theoretical physics, Butterworth-Heinemann, 1991.

[70] A. Leggett, *Quantum Liquids: Bose Condensation and Cooper Pairing in Condensed-matter Systems*. Oxford Graduate Texts, OUP Oxford, 2006.

[71] L. P. Pitaevskii, "Vortex lines in an imperfect bose gas," *Soviet Physics JETP*, vol. 13, pp. 451–454, 1961. Translated from Zh. Eksp. Teor. Fiz. 40, 646 (1961).

[72] E. P. Gross, "Structure of a quantized vortex in boson systems," *Il Nuovo Cimento (1955-1965)*, vol. 20, no. 3, pp. 454–477, 1961.

[73] D. S. Petrov, C. Salomon, and G. V. Shlyapnikov, "Weakly bound dimers of fermionic atoms," *Phys. Rev. Lett.*, vol. 93, p. 090404, Aug 2004.

[74] J. Bardeen, L. N. Cooper, and J. R. Schrieffer, "Microscopic theory of superconductivity," *Phys. Rev.*, vol. 106, pp. 162–164, 1957.

[75] J. Bardeen, L. N. Cooper, and J. R. Schrieffer, "Theory of superconductivity," *Phys. Rev.*, vol. 108, pp. 1175–1204, Dec 1957.

[76] L. N. Cooper, "Bound electron pairs in a degenerate fermi gas," *Phys. Rev.*, vol. 104, pp. 1189–1190, Nov 1956.

[77] L. P. Gorkov and T. K. Melik-Barkhudarov, "Contribution to the theory of superfluidity in an imperfect fermi gas," *Soviet Physics JETP*, vol. 13, pp. 1018–1022, Nov. 1961.

[78] T.-L. Ho, "Universal thermodynamics of degenerate quantum gases in the unitarity limit," *Phys. Rev. Lett.*, vol. 92, p. 090402, Mar 2004.

[79] A. Perali, P. Pieri, L. Pisani, and G. C. Strinati, "Bcs-bec crossover at finite temperature for superfluid trapped fermi atoms," *Phys. Rev. Lett.*, vol. 92, p. 220404, Jun 2004.

[80] J. Dalibard, *Bose Einstein Condensation in Atomic Gases*, vol. Course CXL of *Proceedings of the International School of Physics "Enrico Fermi*, ch. Collisional dynamics of ultra-cold atomic gases, pp. 321–349. IOS Press, 1998.

[81] H. Feshbach, "Unified theory of nuclear reactions," *Annals of Physics*, vol. 5, no. 4, pp. 357–390, 1958.

[82] H. Feshbach, "A unified theory of nuclear reactions. ii," *Annals of Physics*, vol. 19, no. 2, pp. 287–313, 1962.

[83] U. Fano, "Effects of configuration interaction on intensities and phase shifts," *Phys. Rev.*, vol. 124, pp. 1866–1878, Dec 1961.

[84] G. Andrade-Sánchez and V. Romero-Rochín, "Potential and feshbach s-wave resonances in coupled atomic collision channels," *European Journal of Physics*, vol. 44, p. 065401, sep 2023.

[85] A. J. Moerdijk, B. J. Verhaar, and A. Axelsson, "Resonances in ultracold collisions of ^{6}Li, ^{7}Li, and ^{23}Na," *Phys. Rev. A*, vol. 51, pp. 4852–4861, Jun 1995.

[86] H. Stoof, D. Dickerscheid, and K. Gubbels, *Ultracold Quantum Fields*. Theoretical and Mathematical Physics, Springer Netherlands, 2008.

[87] J. E. Carro-Martínez, "Diseño y proyección de trampas magnéticas y ópticas para experimentos de gases ultrafríos de litio." Facultad de Ciencias - Universidad Nacional Autónoma de México, 2016.

[88] M. Bartenstein, A. Altmeyer, S. Riedl, R. Geursen, S. Jochim, C. Chin, J. H. Denschlag, R. Grimm, A. Simoni, E. Tiesinga, C. J. Williams, and P. S. Julienne, "Precise determination of ^{6}Li cold collision parameters by radio-frequency spectroscopy on weakly bound molecules," *Phys. Rev. Lett.*, vol. 94, p. 103201, Mar 2005.

[89] A. G. Martin, K. Helmerson, V. S. Bagnato, G. P. Lafyatis, and D. E. Pritchard, "rf spectroscopy of trapped neutral atoms," *Phys. Rev. Lett.*, vol. 61, pp. 2431–2434, Nov 1988.

[90] C. Chin, M. Bartenstein, A. Altmeyer, S. Riedl, S. Jochim, J. H. Denschlag, and R. Grimm, "Observation of the pairing gap in a strongly interacting fermi gas," *Science*, vol. 305, no. 5687, pp. 1128–1130, 2004.

[91] J. T. Stewart, J. P. Gaebler, and D. S. Jin, "Using photoemission spectroscopy to probe a strongly interacting fermi gas," *Nature*, vol. 454, no. 7205, pp. 744–747, 2008.

[92] Y. Sagi, T. E. Drake, R. Paudel, and D. S. Jin, "Measurement of the homogeneous contact of a unitary fermi gas," *Phys. Rev. Lett.*, vol. 109, p. 220402, Nov 2012.

[93] B. Mukherjee, P. B. Patel, Z. Yan, R. J. Fletcher, J. Struck, and M. W. Zwierlein, "Spectral response and contact of the unitary fermi gas," *Phys. Rev. Lett.*, vol. 122, p. 203402, May 2019.

[94] I. Bloch, T. W. Hänsch, and T. Esslinger, "Atom laser with a cw output coupler," *Phys. Rev. Lett.*, vol. 82, pp. 3008–3011, Apr 1999.

[95] M. R. Matthews, D. S. Hall, D. S. Jin, J. R. Ensher, C. E. Wieman, E. A. Cornell, F. Dalfovo, C. Minniti, and S. Stringari, "Dynamical response of a bose-einstein condensate to a discontinuous change in internal state," *Phys. Rev. Lett.*, vol. 81, pp. 243–247, Jul 1998.

[96] J. Stenger, S. Inouye, D. M. Stamper-Kurn, H.-J. Miesner, A. P. Chikkatur, and W. Ketterle, "Spin domains in ground-state bose-einstein condensates," *Nature*, vol. 396, no. 6709, pp. 345–348, 1998.

[97] P. Törmä, *Spectroscopies — Theory*, ch. Chapter 10, pp. 199–250. Imperial College Press, London UK, 2014.

[98] H. Jasik, *Antenna Engineering Handbook*. No. v. 1 in Antenna Engineering Handbook, McGraw-Hill, 1961.

[99] A. Cosco, "Optimized production and probing ofresonantly interacting lithium-chromiumfermi mixtures." University of Florence, 2023.

[100] A. N. Wenz, "Few-body physicsin a three-component fermi gas." Max-Planck-Institute for Nuclear Physics, 2008.

[101] M. Bartenstein, *From Molecules to Cooper Pairs: Experiments in the BEC-BCSCrossover*. PhD thesis, Leopold-Franzens-Universität Innsbruck, 2005.

[102] C. Balanis, *Antenna Theory: Analysis and Design*. Wiley, 2015.

[103] H. Sizun and P. de Fornel, *Radio Wave Propagation for Telecommunication Applications*. Signals and Communication Technology, Springer Berlin Heidelberg, 2006.

[104] W. Smythe, *Static and Dynamic Electricity*. International series in physics, McGraw-Hill, 1950.

[105] J. Schwinger and K. Milton, *Classical Electrodynamics*. Frontiers in Physics, CRC Press, 2024.

[106] D. S. Barker, A. Restelli, J. A. Fedchak, J. Scherschligt, and S. Eckel, "A radiofrequency voltage-controlled current source for quantum spin manipulation," *Rev. Sci. Instrum.*, vol. 91, p. 104708, 10 2020.

[107] K. Kurokawa, "Power waves and the scattering matrix," *IEEE Transactions on Microwave Theory and Techniques*, vol. 13, no. 2, pp. 194–202, 1965.

[108] C. Zener and R. H. Fowler, "Non-adiabatic crossing of energy levels," *Proc. R. Soc. London, Ser. A.*, vol. 137, no. 833, pp. 696–702, 1932.

[109] T. Lompe, T. B. Ottenstein, F. Serwane, K. Viering, A. N. Wenz, G. Zürn, and S. Jochim, "Atom-dimer scattering in a three-component fermi gas," *Phys. Rev. Lett.*, vol. 105, p. 103201, 2010.

[110] A. Gutiérrez-Valdés, "Estudio de transiciones hiperfinas en un gas cuántico de litio." Facultad de Ciencias - Universidad Nacional Autónoma de México, 2020.

[111] D. Hernández-Rajkov, J. E. Padilla-Castillo, A. del Río-Lima, A. Gutiérrez-Valdés, F. J. Poveda-Cuevas, and J. A. Seman, "Faraday waves in strongly interacting superfluids," *New J. Phys.*, vol. 23, no. 10, p. 103038, 2021.

[112] A. del Río-Lima, J. A. Seman, R. Jáuregui, and F. J. Poveda-Cuevas, "Spatial and temporal periodic density patterns in driven bose-einstein condensates," *Phys. Rev. A*, vol. 110, p. 053318, 2024.

[113] R. Schmidt and T. Enss, "Excitation spectra and rf response near the polaron-to-molecule transition from the functional renormalization group," *Phys. Rev. A*, vol. 83, p. 063620, Jun 2011.

[114] W. E. Liu, Z.-Y. Shi, M. M. Parish, and J. Levinsen, "Theory of radio-frequency spectroscopy of impurities in quantum gases," *Phys. Rev. A*, vol. 102, p. 023304, Aug 2020.

[115] Z. Z. Yan, Y. Ni, A. Chuang, P. E. Dolgirev, K. Seetharam, E. Demler, C. Robens, and M. Zwierlein, "Collective flow of fermionic impurities immersed in a bose-einstein condensate," *Nature Physics*, vol. 20, no. 9, pp. 1395–1400, 2024.

[116] F. Scazza, G. Valtolina, A. Amico, P. E. S. Tavares, M. Inguscio, W. Ketterle, G. Roati, and M. Zaccanti, "Exploring emergent heterogeneous phases in strongly repulsive fermi gases," *Phys. Rev. A*, vol. 101, p. 013603, Jan 2020.

[117] P. F. Bedaque and J. P. D'Incao, "Superfluid phases of the three-species fermion gas," *Annals of Physics*, vol. 324, no. 8, pp. 1763–1768, 2009.

[118] T. Lompe, T. B. Ottenstein, F. Serwane, A. N. Wenz, G. Zürn, and S. Jochim, "Radio-frequency association of efimov trimers," *Science*, vol. 330, no. 6006, pp. 940–944, 2010.

[119] A. Rapp, G. Zaránd, C. Honerkamp, and W. Hofstetter, "Color superfluidity and "baryon" formation in ultracold fermions," *Phys. Rev. Lett.*, vol. 98, p. 160405, Apr 2007.

[120] D. M. Kurkcuoglu and C. A. R. Sá de Melo, "Color superfluidity of neutral ultracold fermions in the presence of color-flip and color-orbit fields," *Phys. Rev. A*, vol. 97, p. 023632, Feb 2018.

[121] C. D. Tran, "Acousto-optic devices," *Analytical chemistry*, vol. 64, no. 20, pp. 971A–981A, 1992.